

Dynamics of long-range interacting quantum spin systems

by

Mauritz van den Worm

*Dissertation approved for the degree of Doctor of
Philosophy in the Faculty of Science at Stellenbosch
University*



Department of Physics,
University of Stellenbosch,
Private Bag X1, Matieland 7602, South Africa.

Promoter: Prof. Dr. M. Kastner

December 2015

Declaration

By submitting this dissertation electronically, I declare that the entirety of the work contained therein is my own, original work, that I am the sole author thereof (save to the extent explicitly otherwise stated), that reproduction and publication thereof by Stellenbosch University will not infringe any third party rights and that I have not previously in its entirety or in part submitted it for obtaining any qualification.

December 2015

Copyright © 2015 Stellenbosch University
All rights reserved.

Abstract

In this thesis we study the time evolution of correlation functions in quantum lattice models in the presence of long-range interactions or hopping decaying asymptotically as a power law. For a large class of initial conditions, exact analytic results are obtained in arbitrary lattice dimension for the long-range Ising model. In contrast to the nearest-neighbour case, we find that correlations decay like stretched or compressed exponentials in time. Provided the long-range character of the interactions is sufficiently strong, pronounced prethermalization plateaus are observed and relaxation timescales are widely separated. Starting from uncorrelated states that are easily prepared in experiments, we show the dynamical emergence of correlations and entanglement in these far-from-equilibrium interacting quantum systems. We characterize these correlations by the entanglement entropy, concurrence, and squeezing, which are inequivalent measures of entanglement corresponding to different quantum resources.

For interaction exponents larger than the lattice dimensionality, a Lieb-Robinson-type bound effectively restricts the spreading of correlations to the interior of a causal region, but allows supersonic (faster than linear) propagation. Using tools of quantum metrology, for any exponents smaller than the lattice dimension, we construct Hamiltonians giving rise to quantum channels with capacities not restricted to any causal region. An analytic analysis of long-range Ising models illustrates the disappearance of the causal region and the creation of correlations becoming distance-independent. In all models we analyzed the spreading of correlations follows a power law, and not the exponential increase of the long-range Lieb-Robinson bound. Lieb-Robinson-type bounds are extended to strongly long-range interactions where the interaction exponent is smaller than the lattice dimension, and we report particularly sharp bounds that are capable of reproducing regimes with soundcone as well as supersonic dynamics. Our results provide guidance for optimizing experimental efforts to harness long-range interactions in a variety of quantum information and signaling tasks.

Uittreksel

In hierdie tesis studeer ons die tydevolusie van korrelasiefunksies in kwantumroostermodelle in die teenwoordigheid van lang-afstand interaksies of spronge wat asimptoties in 'n magswet verval. Vir 'n groot versameling begintoestande word presiese analitiese resultate vir die lang-afstand-Ising-model verkry. In teenstelling met die naaste-naasliggende-interaksie-Ising-model vind ons dat korrelasies soos uitgerekte of saamgepersde eksponentiële funksies in tyd verval. Indien die lang-afstand gedrag van die interaksies lank genoeg is word lanklewende kwasi-stationere toestande gevorm as gevolg van wyd verspreide tydscale wat in die ontspanningsgedrag van die korrelasiefunksies voorkom. Wanneer ongekorrleerde begintoestande, wat eenvoudig in die laboratorium voorberei kan word, gebruik word kan die dinamiese opkoms van verskillende maatstawe van verstrengeling analities bereken word. Gevolglik kan hierdie verstrengelde toestande gebruik word om kwantumberekeninge mee uit te voer.

Vir interaksie-eksponente groter as die roosterdimensie bestaan daar sogenaamde Lieb-Robinson-grense wat die verspreiding van korrelasies beperk tot die binneruim van 'n oorsaaklike-kegel, maar steeds supersoniese verspreiding (vinniger as lineêr) toelaat. Deur gebruik te maak van gereedskap uit kwantummeetkunde kan ons, vir enige interaksie-eksponent kleiner as die roosterdimensie, Hamiltoniane konstrueer wat oorsaak gee aan kwantumkanale met kapasiteite wat nie beperk word deur enige oorsaaklike-kegel nie. Die analitiese resultate van die lang-afstand-Ising-model illustreer die verdwyning van die oorsaaklike-kegel sowel as die vorming van afstand onafhanklike korrelasies. In al die modelle waar ons die verspreiding van korrelasies bestudeer het, het die verspreiding magswette gevolg, en nie die eksponentiële toename wat deur die lang-afstand Lieb-Robinson-grense voorspel word nie. Lieb-Robinson-grense word uitgebrei na kwantumsisteme met sterk-lang-afstand interaksies waar die interaksie-eksponent kleiner is as die roosterdimensie. Besondere skerp grense word voorgedra wat die oorgang van lineêre na supersoniese verspreiding vasvang. Die resultate wat in hierdie tesis vasgevang is verskaf riglyne vir die optimalisering van eksperimentele pogings om lang-afstand interaksies in te span in 'n verskeidenheid kwantuminformasie en -seintake.

Acknowledgements

I would like to express my sincere gratitude to my supervisor, Michael Kastner, for his patient and supportive guidance. Michael gave me the opportunity to work alongside influential physicists from both experimental and theoretical sides of the nonequilibrium quantum physics community. He has a keen eye for detail and has taught me to look extremely critically at my own work, for this I am extremely grateful.

I am grateful for financial support from NITheP over the past six years, not only for the yearly stipend, but also for supporting me in attending two international workshops, one in Boulder Colorado and the other in Trieste Italy. With the support from the NITheP staff I have explored the frontiers of quantum physics, however they also taught me how to communicate scientific ideas and results in the best possible way, for this I am extremely grateful.

A word of thanks is due to Dawid Storch and Kaden Hazzard for many helpful discussions.

Lastly, but most importantly, I would like to thank my friends, family and in particular my wife, Lerinza, for constant encouragement and support throughout the course of my studies.

Contents

Declaration	i
Abstract	ii
Uittreksel	iii
Acknowledgements	iv
Contents	v
List of Figures	viii
List of Tables	x
1 Introduction	1
1.1 Motivation: General background	1
1.1.1 Long-range interactions	1
1.1.2 Equilibration and thermalization of isolated quantum systems	3
1.1.3 Lieb-Robinson bounds	5
1.2 Motivation: Experimental realization	9
1.3 Challenges and outline of thesis	11
1.3.1 The death of a workhorse	11
1.3.2 Outline	13
2 Long-range interacting quantum Ising Model	16
2.1 The model	17
2.2 Orthogonal initial states	20
2.3 Product initial states	23

<i>CONTENTS</i>	vi
2.4 σ^x tensor product initial state	25
2.5 Upper bound on correlations in the thermodynamic limit . . .	27
2.6 Prethermalization	30
2.7 Application to trapped ion quantum simulators	33
2.8 Entanglement in far-from-equilibrium quantum magnetism . .	36
2.8.1 Spin squeezing	38
2.8.2 Entanglement entropy	40
2.8.3 Concurrence	42
2.9 Summary and conclusions	43
3 Supersonic spreading of correlations	44
3.1 Non-equilibrium systems as quantum channels	45
3.2 Lower bounds on information propagation	47
3.2.1 Supersonic propagation in an Ising-like toy model . . .	48
3.2.1.1 Product initial state	49
3.2.1.2 Entangled initial state	50
3.2.2 Supersonic propagation in the full long-range Ising model	51
3.3 Propagation of correlators	54
3.3.1 Exact results for the long-range interacting Ising model	54
3.3.1.1 Finite size scaling	56
3.3.2 Numerical results on the long-range XXZ spin chain .	58
3.4 Comparison with experimental results	58
3.5 Summary and conclusions	63
4 Interplay of soundcone and supersonic dynamics	64
4.1 Lieb-Robinson bounds for $\alpha < D$	66
4.2 Matrix exponential bounds for intermediate α	68
4.3 Long-range hopping for small α	70
4.3.1 Long-range hopping model	71
4.3.2 Propagation from staggered initial state	71
4.3.3 Dispersion and group velocity	73
4.3.4 Density of states and typical propagation velocities . .	75
4.4 Summary and conclusions	77
5 Outlook and preliminary results	80
5.1 Spreading of correlations in initially correlated states	80

<i>CONTENTS</i>	vii
5.2 Many body localization	81
5.2.1 Many body localization in finite-range systems	81
5.2.2 Many body localization in long-ranged systems	84
5.2.3 Fully many body localized systems	87
Appendices	89
A Systematic Calculation of Correlators	90
A.1 Expressing $\prod_i \sigma_i^\pm \prod_j \sigma_j^\mp$ in the Heisenberg Picture	90
A.2 Correlation Functions With Orthogonal Initial States	94
A.3 n -Time Correlators	96
B Lattice Independent Upper Bound	100
B.1 Proof of Equations (2.5.2) and (2.5.3)	100
C Lower Bounds on Information Propagation	105
C.1 Product Initial State	105
C.2 Entangled Initial state	107
C.3 Supersonic propagation in the full long-range Ising Model	108
D Calculation of Entanglement Measures	114
D.1 Spin Squeezing	114
Bibliography	117

List of Figures

1.1	Schematic of short- and long-range Lieb-Robinson bounds	7
2.1	Schematic showing the Bloch sphere representation.	24
2.2	Hexagonal patches of triangular lattices	25
2.3	Time evolution of normalized correlation functions	27
2.4	Time evolution of general upper bounds for different α	28
2.5	Fixed time and contour plot of general upper bounds	29
2.6	Time evolution of single- and two-spin purity	31
2.7	Theoretical prediction of interaction strength $J_{i,j}$	34
2.8	Spin squeezing schematic	37
2.9	Time dependent spin squeezing	39
2.10	Equal time two-spin correlation functions for tipping angles $\pi/2$ and $\pi/4$	39
2.11	Time dependent entanglement entropy	41
2.12	Time dependent concurrence	42
3.1	Schematic representation of the coding.	46
3.2	Graphical representation of lattice constraint in (3.2.3).	48
3.3	Connected correlation function of the Ising model	55
3.4	Connected correlations function in normal and rescaled time	56
3.5	Connected correlation finite size scaling	57
3.6	Connected correlation function for the XXZ model	59
3.7	Experimental Ising and XX connected correlation functions	60
3.8	Experimental supersonic spreading of correlations for $\alpha > D$	61
3.9	Measured magnetization after a local quench	62
4.1	Light-cones arising for three different models in three different α - regimes	65

<i>LIST OF FIGURES</i>	ix
4.2 Shape of causal region for rescaled time Lieb-Robinson bound . . .	68
4.3 Spacetime plots of the matrix exponential bound	69
4.4 Time dependent number operator in long-range hopping fermionic model	72
4.5 Spatio-temporal spreading in long-range hopping fermionic model	73
4.6 Dispersion relation and group velocity of the long-range fermionic hopping model	74
4.7 Density of states of the long-range hopping fermionic model . . .	76
5.1 Level statistics of Oganesyanyan and Huse	83
5.2 Finite-size scaling of the dynamic polarization of the random Heisen- berg model	84
5.3 Finite-size scaling of the dynamic polarization of the random XXZ - model	85
5.4 Mean of r as a function of hopping exponent α for disorder $W = 9$	86
B.1 Schematic used in proof of the lattice independent upper bound .	101
C.1 Transmission probability as a function of time for different α . . .	111
C.2 Faster than linear spreading of transmission probability for $\alpha > D$	112

List of Tables

1.1	Current state-of-the-art in experimental quantum spin systems . .	10
-----	---	----

Chapter 1

Introduction

1.1 Motivation: General background

This work investigates the non-equilibrium dynamics of long-range interacting quantum spin systems. Of fundamental importance is the timescales on which quantum systems relax toward equilibrium, and if the final equilibrium state is given by a Gibbs ensemble or not. Intuition gained from Lieb-Robinson bounds govern our current understanding of the spreading of correlations and the rate at which quantum systems equilibrate. The following subsections delve deeper into long-range interactions, equilibration and thermalization, and the notion of Lieb-Robinson bounds. These are central concepts that will be used throughout this thesis.

1.1.1 Long-range interactions

We define short-range interactions as any two-body interaction that asymptotically decays faster than r^{-D} in separation distance r , or has a finite range outside of which the interaction is zero. Here D is the dimension of the underlying system. In this framework, long-range interactions are defined as those interactions decaying slower than r^{-D} asymptotically.

For nearly a century condensed matter physicists have been fascinated by short-range or nearest neighbour interacting or hopping systems. The interest in short-ranged systems can be traced back to the pioneers of statistical physics, Boltzmann and Gibbs. They were interested in describing the different

states of matter where the fundamental interactions are typically electromagnetic. The presence of both positive and negative charges cause screening effects which give rise to interactions that are effectively short-range or exponentially decaying. This explains the nearly exclusive interest in short- or finite-range interactions in the community of condensed matter physics. From a theoretical point of view short- or finite-range interactions are valuable since they allow to partition a large volume into smaller sub-volumes while neglecting the surface effects of the sub-volumes in the thermodynamic (large system) limit. This mathematical trick has been used extensively to prove theorems in statistical physics for short-range interacting systems. Specifically, this trick is the corner stone of the existence of thermodynamic potentials and their convexity properties in the thermodynamic limit as well as the celebrated equivalence of statistical ensembles.

On the other side of the coin, astrophysicists have been aware of the strange consequences of long-range interactions for decades. The attractive gravitational potential decays like r^{-1} in separation distance and can be considered long-range in any spatial dimension. Moreover, the absence of negative masses renders screening impossible which in turn preserves the long-range nature of the interactions. The first peculiar result in statistical physics, due to the presence of long-range interactions, was published in 1968 by Lynden-Bell and Wood [77]. They showed that self-gravitating gas spheres have negative heat capacities, i.e., adding heat to the system actually decreases the temperature. This phenomenon was later explained by Thirring [112] who showed that the specific heat is always positive when calculated withing the canonical ensemble. This observation showed the nonequivalence of the microcanonical and canonical ensembles in the presence of long-range interactions. These results came as a great surprise since the equivalence of ensembles was assumed by many physicists to be a general property irrespective of the range of interaction.

Physicists studying classical statistical mechanics have delved into long-range interacting systems in a effort to extend traditional short-range statistical physics, see [17] for a review. However, the quantum condensed matter community has taken somewhat longer to become intrigued about the intricacies of long-range interactions. However, owing to the groundbreaking progress in the control of ultra-cold atoms and ions, as well as the creation of ultra-

cold polar molecules, a number of proposals and experimental realizations of quantum simulators for strongly correlated, and in particular spin, systems have been reported [110, 52, 53, 120, 114, 13]. In several of the theoretical proposals, the constituents interact via long-range forces. These include dipolar interactions [21, 81, 71, 7, 39, 46, 88] or phonon mediated interactions in ion crystals [92, 69]. These engineered quantum systems are different from traditional condensed matter systems where the long-range character of the underlying Coulombic interactions is suppressed by screening so that only on-site or nearest neighbour interactions need to be taken into account. Due to their relevance in the context of quantum simulation of many-body systems by ultra-cold gases and trapped ions, long-range interactions have recently moved into the focus of research [57, 58, 59, 60, 39, 78, 67, 91, 37, 55].

1.1.2 Equilibration and thermalization of isolated quantum systems

Thinking classically, if we pierce an inflated balloon inside an empty vacuum chamber, very soon the air molecules will become uniformly distributed within the enclosure, with their velocities reaching the Maxwell distribution, whose width only depends on the total energy and number of particles. The shape of the balloon, where we place it inside the chamber, or where on the surface of the balloon we decide to pierce it plays no role in the final spacial and velocity distributions. This thermodynamic universality can be understood by arguing that the particle trajectories very quickly begin to look alike, even if they have different initial conditions. This is because nonlinear equations drive them to uniformly cover their constant energy manifold with the microcanonical measure. However, in the presence of conserved quantities functionally independent of the Hamiltonian and each other, time evolution is confined to a restricted hypersurface of the constant energy manifold. In this case, even though the system equilibrates, the microcanonical predictions of the equilibrium behaviour fails and the system does not thermalize.

In the quantum world the situation is not so clear. For an isolated quantum system time-evolution is linear, there is an absence of dynamical chaos and the spectrum is discrete. Up until recently it was not clear under what conditions conserved quantities provide constraints on relaxation dynamics in

quantum systems. However, the groundbreaking work of [108, 100, 14, 18] have shaped our current understanding of the influence of conserved quantities in the long-time behaviour of isolated quantum systems. In a nutshell, non-integrable systems are believed to eventually reach a thermal stationary state characterized by a Gibbs distribution with a single temperature. Integrable systems, on the other hand, are not expected to thermalize, but their asymptotic stationary state should nonetheless be described by a generalized Gibbs ensemble with one effective temperature for each conserved quantity.

Equilibration and thermalization are two complementary, but unequal notions of the long-time behaviour of isolated quantum systems. A system is said to equilibrate if its density operator evolves toward some particular state and remains in, or close to, that state for almost all times [75]. To quantify this in mathematical terms suppose we have some system consisting of a subsystem S and bath B . The state of the subsystem $\rho_S(t)$ is found by tracing the global state $\rho(t)$ over the bath, $\rho_S(t) = \text{Tr}_B \rho(t)$. Similarly, the state of the bath at time t is described by $\rho_B = \text{Tr}_S \rho(t)$. The time averaged state of the global system ω is given by

$$\omega = \lim_{\tau \rightarrow \infty} \frac{1}{\tau} \int_0^\tau \rho(t) dt. \quad (1.1.1)$$

Similarly ω_S and ω_B are the time averaged states of the subsystem and bath respectively. The central quantity in determining whether the subsystem equilibrates to its time averaged state is the difference in operator norm,

$$\|\rho_S(t) - \omega_S\|. \quad (1.1.2)$$

However, the state of the subsystem $\rho_S(t)$ will fluctuate around its time average ω_S . Correspondingly their separation, in operator norm, changes in time. To take these fluctuations into account it is necessary to study the time averaged separation,

$$\lim_{\tau \rightarrow \infty} \frac{1}{\tau} \int_0^\tau \|\rho_S(t) - \omega_S\| dt. \quad (1.1.3)$$

This amounts to studying the probability in time that the time-evolved state differs, in operator norm, from some equilibrium state by more than some small $\epsilon > 0$. If this probability is less than some small $\delta(\epsilon) > 0$, the system is considered as equilibrated. This probabilistic notion of equilibration is known

as *typicality* [96, 97, 98, 75, 35, 106, 36, 54].

The equilibrium state does not have to be a Gibbs or any other special state, and it may even depend on the initial state of the global system (unlike our classical picture of the balloon inside the vacuum chamber). Thermalization on the other hand is a much stronger notion and additionally requires that the final equilibrium state be independent of the details of the initial state (similar to the balloon inside the vacuum chamber). When a system thermalizes the equilibrium state must at most depend on a few relevant parameters (like the total energy or bath temperature), and has to be a Gibbs state (microcanonical, canonical or a generalization thereof).

In any quantum system on a finite-dimensional Hilbert space, time evolution is periodic or quasi-periodic. Consequently, large fluctuations that bring the system arbitrarily close to its initial state will inevitably occur in the form of recurrences. Another way, other than typicality, of dealing with the fluctuations of $\rho_S(t)$ as well as the recurrences, consists of taking a suitable infinite system limit. This advances the recurrence times to infinity and simultaneously makes the amplitude of fluctuations around the equilibrium state vanishingly small. We will follow the second approach in this thesis.

We consider in the following a closed (isolated) quantum spin system, in the sense that no thermal bath or other reservoir is coupled to the system. However, for such a closed system, we do not study the relaxation to equilibrium in the above described sense of density operators being close to the equilibrium state. Instead, we restrict our attention to the long-time behaviour of two-spin correlation functions between lattice sites i and j . This can be viewed as studying relaxation to equilibrium in a closed system, but only for a restricted class of observables. Alternatively, since such correlation functions are fully determined by the reduced density operator for sites i and j , we can consider these two sites as an open system, coupled to a bath consisting of all the spins on the remaining lattice sites.

1.1.3 Lieb-Robinson bounds

In relativistic quantum theory, information propagation is limited by the speed of light. This forms the familiar notion of a light-cone, outside of which, no

signals can propagate. On the other hand, in non-relativistic quantum many-body systems the speed of light plays no such role. Naively you might guess that, in the absence of a finite maximum speed, a local change in some part of a spatially extended system can take immediate effect in distant parts. However, at any given time t after the initial perturbation, this effect turns out to be extremely small in the exterior of an effective sound cone, at least for lattice systems with finite-range interactions and finite-dimensional constituents. This effect goes under the name of *quasi-locality* and is the content of the Lieb-Robinson theorem. In the Heisenberg picture the time evolution of an operator O_A , with support $A \subset \Lambda$, is given by (\hbar has been set to 1)

$$O_A(t) = e^{iHt} O_A e^{-iHt}, \quad (1.1.4)$$

which is well-defined for finite lattices Λ . Originally Lieb-Robinson bounds were used to prove that unitary time evolution remains well-defined (in the rigorous context of C^* -algebras) in the thermodynamic limit ($|\Lambda| \rightarrow \infty$) for finite range interacting quantum spin systems (for details see [11]). Later on the connection with the maximum group velocity in finite range interacting quantum many-body systems took on a life of its own. The Lieb-Robinson theorem states that observables, O_A and O_B , respectively supported on non-overlapping subsets A and B of Λ , evolving in the Heisenberg picture satisfy

$$\|[O_A(t), O_B(0)]\| \leq C \|O_A\| \|O_B\| \min(|A|, |B|) e^{(v|t| - \text{dist}(A,B))/\xi} \quad (1.1.5)$$

for spin systems on arbitrary lattices (regular graphs) interacting through finite-range or exponentially decaying potentials [74, 85, 66], for $C, v, \xi > 0$. Here, $O_A(0)$ and $O_B(0)$ are supported only on the subspaces of the Hilbert space corresponding to A and B , respectively. $\text{dist}(A, B)$ denotes the graph-theoretic distance between A and B i.e. the number of edges along the shortest path connecting the two non-overlapping regions. The physical relevance of (1.1.5) lies in the fact that a number of physically interesting quantities like the speed at which information, equal-time correlation functions, or entanglement propagate can be related to the operator norm on the left-hand side of (1.1.5), so that similar bounds also hold for these physical quantities [12, 85, 24]. Moreover, all these physical quantities are negligibly small outside the effective causal cone that is determined by those values of t and $\text{dist}(A, B)$

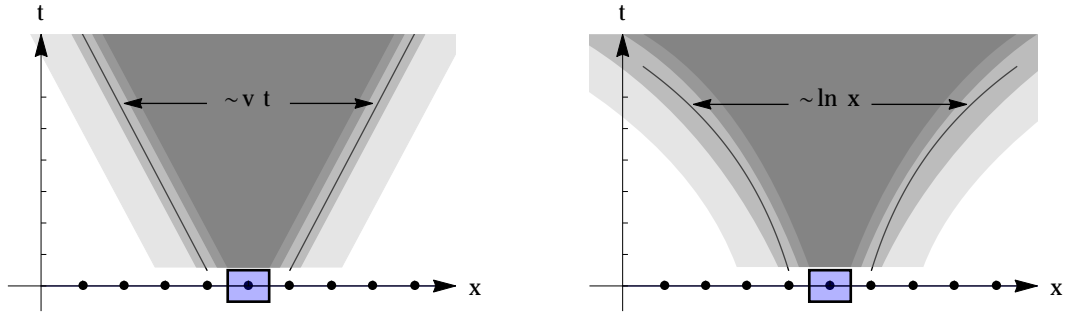


Figure 1.1: Schematic representation of short- and long-range Lieb-Robinson bounds.

for which the exponential in (1.1.5) is larger than some $\epsilon > 0$, which happens for

$$v|t| > \text{dist}(A, B) + \xi \ln \epsilon. \quad (1.1.6)$$

This gives a causal region that grows linearly in the separation distance between regions A and B .

Long-range interactions have a drastic effect on the spreading of correlations. Long-range interacting Hamiltonians take on the general form

$$H_\Lambda = \sum_{X \subset \Lambda} h_X, \quad (1.1.7)$$

where h_X are local Hamiltonian terms of compact support X . Two restrictions are placed on the form of the Hamiltonian. Firstly, a boundedness condition,

$$\sum_{X \ni x, y} \|h_X\| \leq \frac{\lambda}{[1 + \text{dist}(x, y)]^\alpha} \quad (1.1.8)$$

where $\alpha > 0$ is the exponent bounding the decay of the interaction strength at large distances and λ is some finite positive constant. The boundedness condition is a generalization of power-law type interactions, which are going to play a dominant role throughout this thesis. The second condition is reproducibility,

$$\sum_{k \in \Lambda} \frac{1}{[1 + \text{dist}(i, k)]^\alpha [1 + \text{dist}(k, j)]^\alpha} \leq \frac{p}{[1 + \text{dist}(i, j)]^\alpha} \quad (1.1.9)$$

which, in the large system limit, only holds for $\alpha > D$. For exponents α larger than the graph theoretical dimension D of the lattice (coinciding with the standard dimension in case of a cubic lattice), Lieb-Robinson-type bounds have been proved [43, 85] to be of the form

$$\|[O_A(t), O_B(0)]\| \leq C \|O_A\| \|O_B\| \frac{\min(|A|, |B|)(e^{v|t|} - 1)}{[\text{dist}(A, B) + 1]^{\alpha - D}}. \quad (1.1.10)$$

Analogous to the short-range case, this expression limits the way information can propagate in a quantum lattice system. We obtain an effective *causal region* by determining those values of time t and distance $\text{dist}(A, B)$ for which the fraction on the right-hand side of (1.1.10) is larger than $\epsilon > 0$. This condition gives rise to the inequality

$$v|t| > \ln \left[1 + \frac{\epsilon(1 + \text{dist}(A, B))^{\alpha - D}}{\min(|A|, |B|)} \right], \quad (1.1.11)$$

resulting in an effective causal region that is growing logarithmically for large distances. A striking consequence of this behaviour is that the maximum group velocity, given by the slope of the light-cone, grows exponentially with time. This suggests that processes such as equilibration, thermalization and entanglement growth may in principle be sped up exponentially by the presence of long-range power-law interactions. In contrast to the short-range case, spreading of correlations (or entanglement, or information) is not confined to the interior of a linear sound cone, an effect we refer to as “*supersonic*” propagation. The bound (1.1.10) is only valid for $\alpha > D$.

Recently there has been renewed interest in the study of Lieb-Robinson bounds applied to long-range power-law interacting quantum spin systems. The tightness of these long-range Lieb-Robinson bounds have come under the crossfire with many physicists questioning the physicality of the exponential speed-up of timescales for physical processes. Foss-Feig et al. [29] came up with the ingenious insight to calculate the Lieb-Robinson bound in the interaction picture of quantum mechanics. This insight enabled them to prove that the shape of the causal front cannot be logarithmic in the separation distance when $\alpha > 2D$. They also show that the shape of the causal front becomes increasingly linear as α grows larger. This agrees with the fact that when

$\alpha \rightarrow \infty$ the underlying spin model has nearest neighbour interactions and a linear causal region as given by (1.1.5).

For intermediate values of the interaction exponent, $D < \alpha \lesssim 4D$, consensus has not been reached on the exact shapes of the causal regions. Long-range field theoretical models have shown causal regions that initially grow linearly before undergoing a sharp transition to a power-law shaped causal front [95]. In Chapter 4 we introduce a Lieb-Robinson-type bound that captures this transition for intermediate values of α . In Chapter 3 we find long-range interacting spin models that show well-defined causal regions for strong long-range interactions, where $\alpha < D$. Inspired by these results we derive, in Chapter 4, a Lieb-Robinson bound valid for any positive α . These results show a system size dependence on the shape of the causal front but still manage to capture the supersonic spreading of correlations.

It is important to understand that Lieb-Robinson bounds are upper bounds, and generally (especially for long-range interacting systems) they are weak upper bounds. Well chosen long-range interacting models prepared in special initial states might show much slower spreading of correlations, such a model is discussed in Chapter 4.

1.2 Motivation: Experimental realization

As theorists we tend to forget that *real* physics happens in the laboratory. For this reason this section serves as an experimental motivation for studying long-range interacting quantum spin systems. In the following we introduce various physical systems in atomic and condensed matter physics that are pooled together by their portrayal of the familiar XXZ model,

$$H = \frac{1}{2} \sum_{(i,j) \in \Lambda \times \Lambda} [J_{ij}^z \sigma_i^z \sigma_j^z + 2J_{ij}^\perp (\sigma_i^+ \sigma_j^- + \sigma_i^- \sigma_j^+)]. \quad (1.2.1)$$

Here the sum extends over all pairs of lattice sites i and j of an arbitrary lattice Λ . By σ_j^a with $a \in \{x, y, z\}$ we denote the usual Pauli operators, and we define $\sigma_j^\pm = \frac{1}{2} (\sigma_j^x \pm i\sigma_j^y)$. We refer to the first term in (1.2.1) as the *Ising* term, and the second as the *exchange, flip-flop*, or *XX* term. The *XX* terminology comes

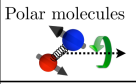
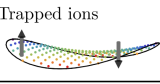
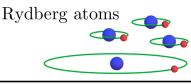
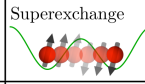
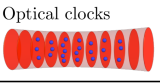
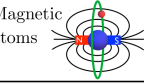
						
(a)	$J_{\perp}, J_{\perp}, J_z$	$J_{\perp}, J_{\perp}, 0$ or $0, 0, J_z$	$J_{\perp}, J_{\perp}, J_z$ or $0, 0, J_z$	$J_{\perp}, J_{\perp}, J_z$	$J_{\perp}, J_{\perp}, J_z$	$J_{\perp}, J_{\perp}, -2J_{\perp}$
(b)	$(1-3\cos^2\theta)/r^3$	$1/r^\alpha; 0 < \alpha < 3$	$(1-3\cos^2\theta)/r^3$ or $1/r^6$	Nearest neighbor	Variable long-range	$(1-3\cos^2\theta)/r^3$
(c)	$10^3 \lesssim J \lesssim 10^5$	$10^2 \lesssim J \lesssim 10^4$	$10^4 \lesssim J \lesssim 10^9$	$1 \lesssim J \lesssim 10^2$	$1 \lesssim J \lesssim 10^2$	$10 \lesssim J \lesssim 10^3$
(d)	$\tau \gtrsim 10^{-2}$ s	$\tau \gtrsim 10^{-3}$ s	$\tau \gtrsim 10^{-6}$ s	$\tau \gtrsim 1$ s	$\tau \gtrsim 10^{-1}$ s	$\tau \gtrsim 10^{-1}$ s
(e)	$N \lesssim 10^5$	$N \lesssim 10^2$	$N \lesssim 10^6$	$N \lesssim 10^6$	$N \lesssim 10^4$	$N \lesssim 10^5$

Table 1.1: (Reproduced from [47]) Properties of six examples of physical systems that can be used to realize the quantum spin models and non-equilibrium dynamics considered in this thesis. (a) *Spin-coupling*. Practicable spin couplings, reported as J_x, J_y, J_z , are to be understood as coefficients of the Hamiltonian $\mathcal{H} = (1/2) \sum_{i \neq j} (J_x S_i^x S_j^x + J_y S_i^y S_j^y + J_z S_i^z S_j^z)$ with $S_i^a = \frac{1}{2} \sigma_i^a$. (b) *Spatial structure*. The distance and angular dependence of the interactions is presented. (c) *Coupling strengths*. Typical coupling strengths are given in Hertz. Coupling strengths are given as a range, which is intended to reflect reasonable coupling strengths realizable in current implementations of these systems. (d) *Coherence times*. Coherence times given are rough lower bounds, but in some special cases (for example by using field-insensitive clock transitions in ions) these times can greatly exceed the stated values. (e) *Number of spins*. System sizes quoted reflect rough upper limits achieved in current experiments. Rydberg atoms exist in a wide variety of regimes, and the numbers given encompass many different experimental situations.

from rewriting the second term as

$$2(\sigma_i^+ \sigma_j^- + \sigma_i^- \sigma_j^+) = \sigma_i^x \sigma_j^x + \sigma_i^y \sigma_j^y \quad (1.2.2)$$

and noting that there are two couplings with the same strength along the x - and y -spin directions. We refer to the case where the XX term vanishes ($J_{ij}^{\perp} = 0$ for all i and j) as the Ising Hamiltonian and the case where the Ising term vanishes ($J_{ij}^z = 0$ for all i and j) as the XX Hamiltonian. In the isotropic case where $J_{ij}^z = J_{ij}^{\perp} := J_{ij}$ for all i and j , it is possible to rewrite the Hamiltonian (1.2.1) as

$$H = \frac{1}{2} \sum_{i \neq j} J_{ij} \boldsymbol{\sigma}_i \cdot \boldsymbol{\sigma}_j \quad (1.2.3)$$

where $\boldsymbol{\sigma}_i = (\sigma_i^x, \sigma_i^y, \sigma_i^z)$ is the vector or Pauli operators on lattice site i . We refer to (1.2.3) as the Heisenberg Hamiltonian.

Specific realizations of the XXZ Hamiltonian discussed in this thesis can be

implemented in a variety of atomic, molecular, optical, and solid-state systems, including but not limited to:

- polar molecules [120, 45],
- trapped ions [64, 72, 13, 53, 99],
- Rydberg atom ensembles [117, 105, 76],
- neutral atoms in optical lattices [113, 40],
- alkaline-earth-atom optical lattice clocks [111, 79],
- tilted Bose-Hubbard models in optical lattices [107],
- magnetic defects in solids (e.g. nitrogen-vacancy centers in diamond) [93], and
- quantum magnetic materials in solid state physics [5, 103, 70, 102, 62].

Experiments in many of these systems have measured the same or closely related non-equilibrium dynamics as those discussed in the body of this thesis. The assortment of applications and scope of these experimental realizations are enormous. Table 1.1 (reproduced from [47]) summarizes the relevant properties (spin-coupling structure, energy scales, coherence times and number of spin degrees of freedom) of several of the experimental systems capable of simulating the XXZ Hamiltonian, and serves as a quick reference to the current state-of-the-art in generating quantum spin models in the laboratory.

1.3 Challenges and outline of thesis

1.3.1 The death of a workhorse

A plethora of tools and techniques have been developed over the years to handle nearest-neighbour interacting or hopping quantum models analytically. The prototypical example is the nearest neighbour transverse field Ising model,

$$H = -J \sum_i (\sigma_i^x \sigma_{i+1}^x + h \sigma_i^z). \quad (1.3.1)$$

This Hamiltonian can be diagonalized by first performing a Jordan-Wigner transformation

$$\sigma_i^z = c_i c_i^\dagger - c_i^\dagger c_i = 1 - 2n_i \quad (1.3.2)$$

$$\sigma_i^x = -(\sigma_1^z \dots \sigma_{i-1}^z) (c_i + c_i^\dagger) \quad (1.3.3)$$

which maps the Pauli operators to Fermionic creation (c_i^\dagger) and annihilation (c_i) operators. The interaction terms in the Hamiltonian can be written as

$$\sigma_i^x \sigma_{i+1}^x = (\sigma_1^z \dots \sigma_{i-1}^z) (c_i + c_i^\dagger) (\sigma_1^z \dots \sigma_i^z) (c_{i+1} + c_{i+1}^\dagger) \quad (1.3.4)$$

$$= (c_i + c_i^\dagger) \sigma_i^z (c_{i+1} + c_{i+1}^\dagger) \quad (1.3.5)$$

$$= (c_i^\dagger - c_i) (c_{i+1} + c_{i+1}^\dagger) \quad (1.3.6)$$

which enables us to rewrite the Hamiltonian in quadratic form

$$H = J \sum_i (c_i^\dagger c_{i+1} + c_i^\dagger c_{i+1} + c_i^\dagger c_{i+1}^\dagger + c_{i+1} c_i - 2hc_i^\dagger c_i + h). \quad (1.3.7)$$

From here the Hamiltonian can be diagonalized by performing a Fourier transformation followed by a Bogoliubov rotation. The transverse field Ising model, together with these techniques, form the standard testing bed for theorists wishing to verify/falsify the validity of some theory in the quantum regime. Vast amounts of literature can be found on this model, however the self-contained works of Calabrese, Essler and Fagotti [15, 16] have become the standard references when dealing with quench or non-equilibrium dynamics within the nearest neighbour transverse field Ising model.

If we extend the interaction of the transverse field Ising model beyond that of nearest neighbour the interaction terms can be written as

$$\sigma_i^x \sigma_{i+\delta}^x = (\sigma_1^z \dots \sigma_{i-1}^z) (c_i + c_i^\dagger) (\sigma_1^z \dots \sigma_{i+\delta-1}^z) (c_{i+\delta} + c_{i+\delta}^\dagger) \quad (1.3.8)$$

$$= (c_i + c_i^\dagger) (\sigma_i^z \dots \sigma_{i+\delta-1}^z) (c_{i+\delta} + c_{i+\delta}^\dagger) \quad (1.3.9)$$

$$= \left[\prod_{j=i+1}^{i+\delta-1} (c_j c_j^\dagger - c_j^\dagger c_j) \right] (c_i^\dagger - c_i) (c_{i+\delta} + c_{i+\delta}^\dagger), \quad (1.3.10)$$

valid for $\delta \geq 2$. This implies that in the presence of interactions beyond nearest

neighbour the Hamiltonian is no longer quadratic in Fermionic creation and annihilation operators and is in general not analytically solvable any longer. This signifies the death of the *ever faithful* work horse in the presence of long-range interactions.

The biggest challenge of this thesis is the absence of the machinery that has been built up to tackle nearest neighbour interacting quantum spin systems. Nevertheless, by carefully choosing initial states we have made significant progress regarding analytic results in the presence of long-range interactions. In the following we present an outline of this thesis.

1.3.2 Outline

In Chapter 2 we introduce the long-range interacting quantum Ising model and define a class of initial states which enables exact calculation of any order correlation function. We apply these exact results to lattices consisting of hexagonal patches of triangular lattices, as can be found in recent ion trap experimental setups [13]. Depending on the range of interaction two distinct relaxation dynamics occur. For shorter-ranged interactions local correlation functions decay on a single timescale, while sufficiently long-ranged interactions introduce a second, much slower, timescale on which the final relaxation takes place. The fast and slow timescales are separated by a long-lived quasi stationary state or prethermalization plateau. Upper bounds on two-spin correlation functions that capture the qualitative features of the actual relaxation dynamics are derived. These upper bounds hint at the possibility of an additional relaxation timescale that emerges in between the long- and short-ranged regimes for dimensions $D \geq 3$. We present the formation of different types of entanglement when starting from carefully chosen product initial states. The results of Chapter 2 were published in

- M. van den Worm, B. C. Sawyer, J. J. Bollinger, and M. Kastner, *Relaxation timescales and decay of correlations in a long-range interacting quantum simulator*, New J. Phys. **15** (2013), 083007
- M. Kastner and M. van den Worm, *Relaxation timescales and prethermalization in d -dimensional long-range quantum spin models*, Phys. Scr

(2015), no. T165, 14039

- K. R. A. Hazzard, M. van den Worm, M. Foss-Feig, S. R. Manmana, E. Dalla Torre, T. Pfau, M. Kastner, and A. M. Rey, *Quantum correlations and entanglement in far-from-equilibrium spin systems*, Phys. Rev. A **90** (2014), 063622.

Chapter 3 deals with the spreading of correlations in long-range quantum spin models. The analytic results of Chapter 2 are used to determine exact expression for equal time connected correlations functions which show *supersonic*, faster than linear, spreading of correlations for sufficiently long-range interactions. To complement the intuition obtained from long-range Lieb-Robinson bounds we determine lower bounds to the spreading of classical information in the long-range Ising model. Depending on whether we choose a product or entangled initial state qualitatively different behaviour can be seen. At the end of Chapter 3 we compare our exact calculations to recent experimental results. This chapter is mainly based on

- J. Eisert, M. van den Worm, S. R. Manmana, and M. Kastner, *Breakdown of quasi-locality in long-range quantum lattice models*, Phys. Rev. Lett. **111** (2013), 260401.

but also contains results from

- D.M. Storch, M. van den Worm, and M. Kastner, *Interplay of soundcone and supersonic propagation in lattice models with power law interactions*, New J. Phys. **17** (2015), 063021.

In Chapter 4 we investigate the interplay of linear and supersonic propagation of correlations in long-range interacting and hopping quantum lattice models. We extend the validity of Lieb-Robinson bounds to ultra long-ranged interacting systems, with interaction exponent less than the dimensionality, and report particularly sharp bounds that are capable of reproducing regimes with linear as well as supersonic spreading dynamics. We show, using the long-range hopping fermionic model together with special initial states, that

linear spreading of correlations may persist even in the presence of strongly long-ranged hopping. Counter intuitively, this model shows an emergent localization for strongly long-ranged hopping. Using exact expressions for the dispersion relation and density of states this emergent localization is explained. This chapter is based on

- D.M. Storch, M. van den Worm, and M. Kastner, *Interplay of soundcone and supersonic propagation in lattice models with power law interactions*, New J. Phys. **17** (2015), 063021.

Lastly, in Chapter 5 we present possible future avenues along which ideas and results presented in the previous chapters may be exploited. Of particular interest is the study of the many-body localization-delocalization transition in the presence of long-range hopping or interactions, and the use of the exact results of Chapter 2 to study the fully many-body localized regime.

Chapter 2

Long-Range Interacting quantum Ising Model

In this chapter we study the time evolution of correlation functions in isolated long-range interacting quantum Ising systems on arbitrary lattices. We show exact analytic results that enhance our understanding of different relaxation timescales and general non-equilibrium properties of long-range interacting quantum systems. In particular we find that for sufficiently long-range interactions, a second relaxation timescale emerges, that is substantially slower than the timescale on which single-spin observables relax to equilibrium. As a consequence, pronounced *prethermalization plateaus* (or long-lived quasi-stationary states) are observed.

This chapter introduces the long-range interacting Ising model in a rigorous fashion. In Section 2.1 we define the long-range Ising Hamiltonian and argue that even though the model appears to be simple and *classical* it does contain true quantum peculiarities that make it interesting from both a theoretical and experimental point of view. Section 2.2 introduces the class of orthogonal initial states that allows exact analytic calculation of any order correlation function in the long-range interacting Ising model. This class of initial states is very large and contains all product initial states constrained to the xy -plane in the Bloch sphere representation. However, product initial states are special in the sense that they are easily related to actual experimental setups. For this reason Section 2.3 shows how the correlation functions can be expressed when restricting to pure product initial states. In Section 2.4 we give analytic

expressions and graphical representations of single- and two-spin correlation functions with initial states taken from a subset of the class of orthogonal initial states. This choice greatly simplifies the expressions for the single- and two-spin correlation functions (2.2.11). Upper bounds of the two-spin correlation functions on arbitrary regular lattice structures, valid in any spatial dimension are derived in Section 2.5. The formation of the prethermalization plateaus and the mechanism responsible for relaxation are discussed in Section 2.6. In Section 2.7 we examine the application of these exact analytic results in the benchmarking of recent trapped ion quantum simulators [13]. Exact results for time evolved entanglement measures can be found in Section 2.8. Finally Section 2.9 summarises the results of this chapter.

Note: This chapter is based on the results of [116], [61] and [46].

2.1 The model

In this Section we introduce the long-range interacting Ising model in a general form. Let Λ be a D -dimensional lattice. At each site i of Λ associate a two dimensional Hilbert space \mathbb{C}_i^2 . The quantum dynamics takes place on the tensor product Hilbert space

$$\mathcal{H} = \bigotimes_{i \in \Lambda} \mathbb{C}_i^2. \quad (2.1.1)$$

Define the *long-range Ising Hamiltonian* as

$$H = -\frac{1}{2} \sum_{(i,j) \in \Lambda \times \Lambda} J_{i,j} \sigma_i^z \sigma_j^z - h \sum_{i \in \Lambda} \sigma_i^z \quad (2.1.2)$$

where σ_i^z is the z -Pauli matrix defined at lattice site i . Define the coupling matrix as

$$J_{i,j} = \frac{1}{|i-j|^\alpha}, \quad (2.1.3)$$

where $|\cdot|$ denotes the Euclidean distance between lattice sites i and j with $\alpha \geq 0$. For the above Hamiltonian to be self-adjoint (or Hermitian), we require that the coupling terms $J_{i,j}$ be real. We define $J_{i,j}$ be a function only of the Euclidean distance $|i-j|$ between lattice sites i and j . To avoid self interaction

CHAPTER 2. LONG-RANGE INTERACTING QUANTUM ISING MODEL 18

we require $J_{i,i} = 0$ and for stability we require that the total energy at any site due to interaction with the entire lattice be finite,

$$\sum_{i \in \Lambda} J_{i,j} < \infty. \quad (2.1.4)$$

When dealing with a finite lattice Λ the above inequality always holds, irrespective of the value of the interaction exponent α . However in the thermodynamic limit $|\Lambda| \rightarrow \infty$ with $\alpha \leq D$ the inequality does not hold. In this case, where the sum over all the interactions diverge, we renormalize the interaction by

$$J_{i,j} \mapsto \mathcal{N}_\alpha J_{i,j} \quad (2.1.5)$$

with

$$\mathcal{N}_\alpha := \left(\sum_{i \in \Lambda} J_{i,j} \right)^{-1}. \quad (2.1.6)$$

This normalization renders the energy per spin $\langle \mathcal{H} \rangle / |\Lambda|$ finite in the thermodynamic limit $|\Lambda| \rightarrow \infty$ when $\alpha \leq D$ and makes the model well-defined.

Naively the long-range interacting Ising model (2.1.2) may seem to be *classical* since all the elements in the Hamiltonian commute amongst themselves. This is however not the case. Formally, we may argue that since the observables of the model live on the space of bounded linear operators $B(\mathcal{H})$ of the tensor product Hilbert space \mathcal{H} , which is a *noncommutative* C^* -algebra, the model has to be quantum in nature. As an example notice that any observable in the long-range interacting Ising model can be written as a linear combination of products of Pauli operators $\{\sigma_j^a\}$ with $a \in \{x, y, z\}$. In general these do not commute amongst themselves which implies that the algebra of observables is noncommutative. On the other hand, the observables of the classical Ising model form a maximal commutative C^* -subalgebra of $B(\mathcal{H})$, which can be shown to consist of continuous functions that commute amongst themselves [101].

Following a more intuitive or physical approach we can prepare initial states for the long-range interacting Ising model that are not eigenstates of the Hamiltonian (2.1.2). This can, for example, be achieved using a quantum quench

CHAPTER 2. LONG-RANGE INTERACTING QUANTUM ISING MODEL 19

where we prepare the initial state to be the ground state of the Hamiltonian,

$$H = -\frac{1}{2} \sum_{(i,j) \in \Lambda \times \Lambda} J_{i,j} \sigma_i^z \sigma_j^z - h \sum_{i \in \Lambda} \sigma_i^z + h_x \sum_{i \in \Lambda} \sigma_i^x \quad (2.1.7)$$

with $h_x \gg h, J_{i,j}$. This polarizes all the spins along the x -axis. Then at time $t = 0$ we set $h_x = 0$ and study the ensuing unitary quantum dynamics of some suitably chosen observable. In Section 2.8 we show that unitary time evolution governed by the long-range interacting Ising Hamiltonian (2.1.2) generates bipartite and even true multipartite entangled states. Clearly the same cannot be done using the *classical* Ising model.

In equilibrium, the long-range interacting Ising model (2.1.2) is known to undergo a transition from a ferromagnetic phase at low temperature to a paramagnetic phase at high temperature. In spatial dimensions $D \geq 2$ such a transition occurs for all non-negative values of the exponent α , whereas for $D = 1$ the transition is present only for $\alpha \leq 2$ [22].

We are interested in studying the time evolution of expectation values of observables — correlation functions — within the long-range interacting Ising model. To pursue this endeavor we write time dependent observables in the Heisenberg picture as

$$A(t) = e^{iHt} A e^{-iHt} \quad (2.1.8)$$

where we have chosen units of $\hbar = 1$. Expectation values are found by evaluating

$$\langle A(t) \rangle = \text{Tr} [A(t) \rho(0)] \quad (2.1.9)$$

where $\rho(0)$ is some initial state. Depending on the structure of the chosen observable, the form of the initial state and the value of the interaction exponent α we show new dynamical behaviour that occurs in this simple, yet *quantum*, spin model. Remarkably and surprisingly, we will see that the long-time dynamics studied in this chapter turns out to be independent of whether the corresponding energies are situated in the low- or high-energy regime.

2.2 Orthogonal initial states

The aim of this Section is to define a general class of initial states that gives rise to analytic expressions for the time dependent correlation functions of the long-range interacting Ising model. This class of initial states is inspired by Radin [94]. Define the triple

$$A := (A_1, A_2, A_3) \quad (2.2.1)$$

together with the operator

$$\sigma^A := \left(\prod_{i \in A_1} \sigma_i^x \right) \left(\prod_{j \in A_2} \sigma_j^y \right) \left(\prod_{k \in A_3} \sigma_k^z \right) \quad (2.2.2)$$

where the A_i 's are mutually disjoint finite subsets of the lattice Λ . Define the following class of initial density matrices:

Definition 2.2.1. (*Orthogonal Initial States*)

We say that the initial density matrix $\rho(0)$ is in the class of orthogonal initial states if for any triple $A = (A_1, A_2, A_3)$ with $A_3 \neq \emptyset$ we have

$$\text{Tr} [\sigma^A \rho(0)] = 0. \quad (2.2.3)$$

Phrased differently, if the operator σ^A contains at least one σ^z Pauli matrix then its expectation value with respect to an initial state in the class of orthogonal initial states will be zero. Examples of orthogonal initial states include initial states prepared diagonal in the Pauli σ^x and σ^y tensor product eigenbasis. The most general orthogonal initial state can be written as

$$\rho(0) = \frac{1}{2^{|\Lambda|}} \left(\mathbb{1} + \sum_{i \in \Lambda} \sigma_i^a \left(s_i^a + \sum_{j \in \Lambda \setminus \{i\}} \sigma_j^b \left(s_{ij}^{ab} + \sum_{k \in \Lambda \setminus \{i,j\}} \sigma_k^c \left(s_{ijk}^{abc} + \sum_{l \in \Lambda \setminus \{i,j,k\}} \dots \right) \right) \right) \right) \quad (2.2.4)$$

where $\mathbb{1}$ denotes the identity operator on the tensor product Hilbert space $\mathcal{H} = \otimes_{i \in \Lambda} \mathbb{C}_i^2$, and the sums run over $a, b, c, d \in \{x, y\}$. From (2.2.4) it follows that

$$s_i^a = \langle \sigma_i^a \rangle, \quad s_{ij}^{ab} = \langle \sigma_i^a \sigma_j^b \rangle, \quad s_{ijk}^{abc} = \langle \sigma_i^a \sigma_j^b \sigma_k^c \rangle, \quad \dots \quad (2.2.5)$$

CHAPTER 2. LONG-RANGE INTERACTING QUANTUM ISING MODEL 21

The set of all $\rho(0)$ as defined in (2.2.4) is a very large class of initial states parameterized by more than 2^N real continuous parameters (2.2.5). This can be compared with the size of the class of initial states of the much studied quantum quenches, a rather restrictive class of initial states parameterized by only two parameters, namely the quench parameter before and after the quench. The idea of considering the class of orthogonal initial states was used by Emch [26], Radin [94], and later by Kastner [59] for both the nearest neighbour ($\alpha = \infty$) and long-range cases to calculate time dependent single spin expectation values. The most efficient method to calculate $\langle \sigma_m^x(t) \rangle$ and $\langle \sigma_m^y(t) \rangle$ involves determining the time evolution of

$$\sigma_m^\pm = \frac{1}{2} (\sigma_m^x \pm i\sigma_m^y). \quad (2.2.6)$$

From (2.2.6) it is clear that

$$\langle \sigma_m^x \rangle = 2\text{Re} (\langle \sigma_m^\pm \rangle), \quad \langle \sigma_m^y \rangle = \mp 2\text{Im} (\langle \sigma_m^\pm \rangle). \quad (2.2.7)$$

Moreover, since σ_m^z commutes with the Hamiltonian (2.1.2) it does not evolve in time. For a system of arbitrary finite size the single spin expectation values (calculated in Appendix A) are given by

$$\begin{aligned} \langle \sigma_m^x(t) \rangle &= 2\text{Re} [\langle \sigma_m^+(0) \rangle e^{-2iht}] \prod_{k \in \Lambda \setminus \{m\}} \cos(2J_{m,k}t) \\ \langle \sigma_m^y(t) \rangle &= 2\text{Im} [\langle \sigma_m^+(0) \rangle e^{-2iht}] \prod_{k \in \Lambda \setminus \{m\}} \cos(2J_{m,k}t) \\ \langle \sigma_m^z(t) \rangle &= \langle \sigma_m^z(0) \rangle. \end{aligned} \quad (2.2.8)$$

Using the identities

$$\begin{aligned} 4\sigma_i^\pm \sigma_j^\pm &= \sigma_i^x \sigma_j^x - \sigma_i^y \sigma_j^y \pm i\sigma_i^x \sigma_j^y \pm i\sigma_i^y \sigma_j^x, \\ 4\sigma_i^\pm \sigma_j^\mp &= \sigma_i^x \sigma_j^x + \sigma_i^y \sigma_j^y \mp i\sigma_i^x \sigma_j^y \pm i\sigma_i^y \sigma_j^x \end{aligned} \quad (2.2.9)$$

CHAPTER 2. LONG-RANGE INTERACTING QUANTUM ISING MODEL 22

we can write

$$\begin{aligned}
\sigma_i^x \sigma_j^x &= 2\text{Re} [\sigma_i^\pm \sigma_j^\mp + \sigma_i^\pm \sigma_j^\pm], \\
\sigma_i^y \sigma_j^y &= 2\text{Re} [\sigma_i^\pm \sigma_j^\mp - \sigma_i^\pm \sigma_j^\pm], \\
\sigma_i^x \sigma_j^y &= \mp 2\text{Im} [\sigma_i^\pm \sigma_j^\mp - \sigma_i^\pm \sigma_j^\pm], \\
\sigma_i^y \sigma_j^x &= \pm 2\text{Im} [\sigma_i^\pm \sigma_j^\mp + \sigma_i^\pm \sigma_j^\pm].
\end{aligned} \tag{2.2.10}$$

In the end only expectation values of $\sigma_i^\pm \sigma_j^\pm$ and $\sigma_i^\pm \sigma_j^\mp$ are required to determine the relevant two-spin correlation functions. In their most general form the two-spin correlation functions within the class of orthogonal initial states are given by

$$\begin{aligned}
\langle \sigma_i^x(t) \sigma_j^x(t) \rangle &= 2\text{Re} [\langle \sigma_i^+(0) \sigma_j^-(0) \rangle P_{i,j}^- + \langle \sigma_i^+(0) \sigma_j^+(0) \rangle e^{-4iht} P_{i,j}^+], \\
\langle \sigma_i^y(t) \sigma_j^y(t) \rangle &= 2\text{Im} [\langle \sigma_i^+(0) \sigma_j^-(0) \rangle P_{i,j}^- - \langle \sigma_i^+(0) \sigma_j^+(0) \rangle e^{-4iht} P_{i,j}^+], \\
\langle \sigma_i^y(t) \sigma_j^x(t) \rangle &= 2\text{Im} [\langle \sigma_i^+(0) \sigma_j^-(0) \rangle P_{i,j}^- + \langle \sigma_i^+(0) \sigma_j^+(0) \rangle e^{-4iht} P_{i,j}^+], \\
\langle \sigma_i^x(t) \sigma_j^z(t) \rangle &= 2\text{Re} \left[i \sin(J_{i,j}t) \langle \sigma_i^+(0) \rangle e^{-2iht} \prod_{k \in \Lambda \setminus \{i,j\}} \cos(2J_{k,i}t) \right], \\
\langle \sigma_i^y(t) \sigma_j^z(t) \rangle &= 2\text{Im} \left[i \sin(J_{i,j}t) \langle \sigma_i^+(0) \rangle e^{-2iht} \prod_{k \in \Lambda \setminus \{i,j\}} \cos(2J_{k,i}t) \right], \\
\langle \sigma_i^z(t) \sigma_j^z(t) \rangle &= \langle \sigma_i^z(0) \sigma_j^z(0) \rangle
\end{aligned} \tag{2.2.11}$$

where we define

$$P_{i,j}^\pm = \prod_{k \in \Lambda \setminus \{i,j\}} \cos[2t(J_{i,k} \pm J_{j,k})]. \tag{2.2.12}$$

Details of these calculations can be found in Appendix A. These expressions are valid for arbitrary coupling constants $J_{i,j}$, and therefore apply in arbitrary spatial dimension and on arbitrary lattices. Moreover, these expressions can easily be evaluated on a personal computer for millions of spins. The presence of a longitudinal field $h \neq 0$ in (2.2.11) imposes a spin precession at an angular frequency proportional to h . For the relaxation to equilibrium we are interested in, such an oscillatory spin precession is irrelevant and merely amounts to a Larmor precession. Further discussion will be restricted to the $h = 0$ case.

Using the class of orthogonal initial states any order correlation function of the long-range interacting Ising model can be calculated. Since any operator on \mathbb{C}^{2^N} can be expanded in products of Pauli operators, such results for correlation

functions of arbitrary order enable the computation of the time evolution of expectation values of arbitrary operators. For details of the calculations see appendix A.

Within the class of orthogonal initial states these results can be extended to n -time correlation functions

$$\left\langle \prod_{i=1}^n A_i(t_i) \right\rangle = \text{Tr} \left[\prod_{i=1}^n A_i(t_i) \rho(0) \right] \quad (2.2.13)$$

with A_i operators on the tensor product Hilbert space \mathcal{H} , each evolving at a different time t_i . In particular, two-time correlation functions can be used to calculate dynamical response functions involving arbitrary Pauli matrices [31].

2.3 Product initial states

Another useful class of initial states, which we will use in Section 2.8, are the familiar product initial states. Pure product initial states can be parametrized by angles, allowing the study of the angular dependence of time dependent correlation functions. However, it is less general than the *class of orthogonal initial states* in the sense that time evolution of entangled initial states cannot be studied.

The most general product initial state takes the form

$$|\Psi(0)\rangle = \bigotimes_{j \in \Lambda} \left(e^{i\phi_j/2} \cos \frac{\theta_j}{2} |\uparrow\rangle_j + e^{-i\phi_j/2} \sin \frac{\theta_j}{2} |\downarrow\rangle_j \right) \quad (2.3.1)$$

where θ_j and ϕ_j are the polar and azimuthal angles in the Bloch sphere representation. $|\uparrow\rangle_j$ and $|\downarrow\rangle_j$ are eigenstates of σ_j^z with eigenvalues $+1$ and -1 respectively. Since σ_j^z commutes with the long-range interacting Ising Hamiltonian (2.1.2), its expectation value remains constant during the time evolution,

$$\langle \sigma_j^z(t) \rangle = \cos \theta_j, \quad (2.3.2)$$

$$\langle \sigma_j^z(t) \sigma_k^z(t) \rangle = \cos \theta_j \cos \theta_k. \quad (2.3.3)$$

The following results are from [31, 30], where derivations can be found.

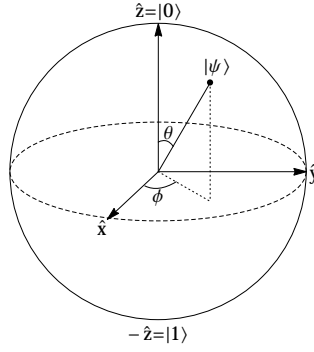


Figure 2.1: Schematic showing the Bloch sphere representation.

The time dependent expectation value of σ_j^\pm is

$$\langle \sigma_j^\pm(t) \rangle = \frac{1}{2} e^{i\phi_j} \sin \theta_j \prod_{k \in \Lambda \setminus \{j\}} g_k^\pm(2J_{k,i}t) \quad (2.3.4)$$

where we define

$$g_j^\pm(x) = \cos^2 \left(\frac{\theta_j}{2} \right) e^{-ix} \pm \sin^2 \left(\frac{\theta_j}{2} \right) e^{ix}. \quad (2.3.5)$$

The x and y spin components are given by

$$\langle \sigma_j^x(t) \rangle = 2\text{Re} [\sigma_j^+(t)], \quad \langle \sigma_j^y(t) \rangle = 2\text{Im} [\sigma_j^+(t)]. \quad (2.3.6)$$

The remaining two-point correlation functions are given by

$$\langle \sigma_j^+(t) \sigma_k^z(t) \rangle = \frac{1}{2} e^{i\phi_j} \sin(\theta_j) g_k^-(2J_{j,k}t) \prod_{l \in \Lambda \setminus \{j,k\}} g_l^+(2J_{j,l}t), \quad (2.3.7)$$

$$\langle \sigma_j^+(t) \sigma_k^+(t) \rangle = \frac{1}{4} e^{i(\phi_j + \phi_k)} \sin \theta_j \sin \theta_k \prod_{l \in \Lambda \setminus \{j,k\}} g^+[2(J_{j,l} + J_{k,l})t], \quad (2.3.8)$$

$$\langle \sigma_j^+(t) \sigma_k^-(t) \rangle = \frac{1}{4} e^{i(\phi_j - \phi_k)} \sin \theta_j \sin \theta_k \prod_{l \in \Lambda \setminus \{j,k\}} g^+[2(J_{j,l} - J_{k,l})t]. \quad (2.3.9)$$

For $j \neq k$ it follows from the definitions that

$$\begin{aligned} \langle \sigma_j^+(t) \sigma_k^-(t) \rangle &= \langle \sigma_j^-(t) \sigma_k^+(t) \rangle^*, \\ \langle \sigma_j^+(t) \sigma_k^+(t) \rangle &= \langle \sigma_j^-(t) \sigma_k^-(t) \rangle^*, \\ \langle \sigma_j^+(t) \sigma_k^z(t) \rangle &= \langle \sigma_j^-(t) \sigma_k^z(t) \rangle^*. \end{aligned} \quad (2.3.10)$$

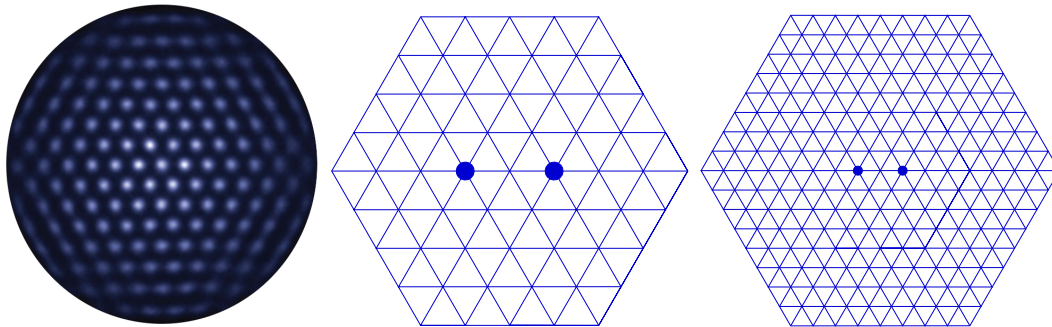


Figure 2.2: Left: a top-view resonance fluorescence image showing the center region of an ion crystal captured in the ions' rest frame taken from [13]. Fluorescence is an indication of a valence electron being in the spin-up state. Here, all ions are in the spin-up state. The lattice constant is approximately $20\mu\text{m}$. Center and right: Triangular lattices on hexagonal patches of side lengths $L = 4$ and 8 .

Using (2.2.10) the x and y components of the two-spin correlation functions can be determined.

As in the case of the class of orthogonal initial states these results can be extended to equal time correlation functions of any order. Similar calculations can also be used to determine n -time correlators. In Section 2.8 we study the angular dependence of the formation of different measures of entanglement starting from pure product initial states. These exact results are directly applicable to current experimental configurations and confirm the “*quantumness*” of the long-range interacting Ising model (2.1.2).

2.4 σ^x tensor product initial state

As mentioned in the introduction, we aim to study the relaxation to equilibrium of the long-range interacting Ising model (2.1.2). Specifically, we study the time evolution of two-spin correlation functions (2.2.11). In order to simplify the general form of the two-spin correlation functions (2.2.11) we restrict ourselves to initial density operators $\rho(0)$ that are diagonal in the σ^x tensor product eigenbasis,

$$\rho(0) = \frac{1}{2^{|\Lambda|}} \left(\mathbb{1} + \sum_{i \in \Lambda} \sigma_i^x \left(s_i^x + \sum_{j \in \Lambda \setminus \{i\}} \sigma_j^x \left(s_{ij}^{xx} + \sum_{k \in \Lambda \setminus \{i,j\}} \sigma_k^x \left(s_{ijk}^{xxx} + \sum_{l \in \Lambda \setminus \{i,j,k\}} \dots \right) \right) \right) \right). \quad (2.4.1)$$

This class of initial states falls within the class of orthogonal initial states (see Definition 2.2.1) but simplifies the expressions of the correlation functions. For

vanishing longitudinal magnetic field $h = 0$, the results are

$$\langle \sigma_i^x(t) \sigma_j^y(t) \rangle = \langle \sigma_i^x(t) \sigma_j^z(t) \rangle = \langle \sigma_i^z(t) \sigma_j^z(t) \rangle = 0, \quad (2.4.2)$$

$$\langle \sigma_i^y(t) \sigma_j^z(t) \rangle = \langle \sigma_i^x(0) \rangle \sin(2J_{i,j}t) \prod_{k \in \Lambda \setminus \{i,j\}} \cos(2J_{k,i}t), \quad (2.4.3)$$

$$\langle \sigma_i^x(t) \sigma_j^x(t) \rangle = \frac{1}{2} \langle \sigma_i^x(0) \sigma_j^x(0) \rangle (P_{i,j}^- + P_{i,j}^+), \quad (2.4.4)$$

$$\langle \sigma_i^y(t) \sigma_j^y(t) \rangle = \frac{1}{2} \langle \sigma_i^x(0) \sigma_j^x(0) \rangle (P_{i,j}^- - P_{i,j}^+) \quad (2.4.5)$$

with

$$P_{i,j}^\pm = \prod_{k \in \Lambda \setminus \{i,j\}} \cos[2(J_{k,i} \pm J_{k,j})t]. \quad (2.4.6)$$

Besides an overall factor of $\langle \sigma_i^x(0) \rangle$ or $\langle \sigma_i^x(0) \sigma_j^x(0) \rangle$, Equations (2.4.2)-(2.4.5) do not depend on the particular choice of initial state, but apply to all $\rho(0)$ in the σ^x tensor product eigenbasis.

As an example, we determine the time evolution (2.4.2)-(2.4.5) of two-spin correlation functions as illustrated in Figure 2.3 for system parameters similar to those of the ion trap experiment of Britton et al. [13]. We consider hexagonal patches of triangular lattices (see Figure 2.2), and couplings $J_{i,j} = J|i - j|^{-\alpha}$ proportional to the α th power of the inverse Euclidean distance between lattice sites i and j , and $J \in \mathbb{R}$ being a coupling constant. Numerical calculations for other two-dimensional lattice structures and geometries, show similar qualitative and quantitative behaviour.

The plots in Figure 2.3 show the normalized expectation values $\langle \sigma_i^x(t) \sigma_j^x(t) \rangle / \langle \sigma_i^x(0) \sigma_j^x(0) \rangle$, $\langle \sigma_i^y(t) \sigma_j^y(t) \rangle / \langle \sigma_i^x(0) \sigma_j^x(0) \rangle$, $\langle \sigma_i^y(t) \sigma_j^z(t) \rangle / \langle \sigma_i^x(0) \rangle$ and $\langle \sigma_i^x(t) \rangle / \langle \sigma_i^x(0) \rangle$, as given by (2.4.2)-(2.4.5). The plotted curves suggest that correlations decay to their microcanonical equilibrium values $\langle \sigma_i^a \sigma_j^b \rangle_{\text{mc}} = 0$ where $a, b \in \{x, y, z\}$, however this is only an apparent decay. Since the expression in (2.4.2)-(2.4.5) consist of products on N trigonometric functions, the time evolution of two-spin correlation functions is quasi-periodic for any finite number N of spins. This is exactly the situation described in the introduction (see Section 1.1.2) for general finite quantum systems on a finite dimensional Hilbert space. Accordingly, recurrences will occur that repeatedly bring the system arbitrarily close to its initial state. These recurrences occur

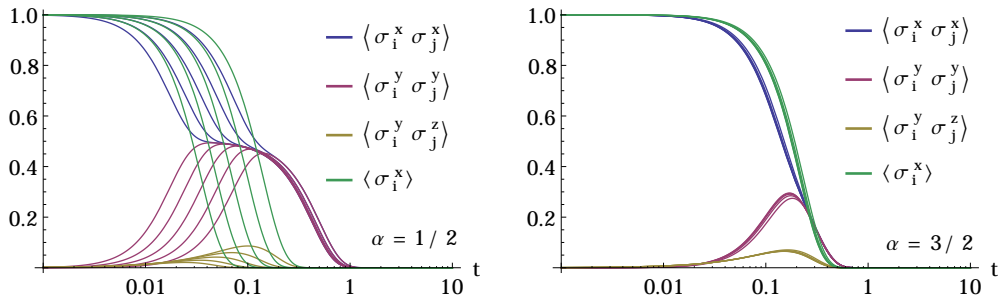


Figure 2.3: (Reproduced from [116]) The time evolution of the normalized expectation values $\langle \sigma_i^x(t) \sigma_j^x(t) \rangle / \langle \sigma_i^x(0) \sigma_j^x(0) \rangle$, $\langle \sigma_i^y(t) \sigma_j^y(t) \rangle / \langle \sigma_i^y(0) \sigma_j^y(0) \rangle$, $\langle \sigma_i^y(t) \sigma_j^z(t) \rangle / \langle \sigma_i^y(0) \sigma_j^z(0) \rangle$ and $\langle \sigma_i^x(t) \rangle / \langle \sigma_i^x(0) \rangle$, as given by (2.4.2)-(2.4.5). The lattice sites i and j are chosen one lattice site to the right, respectively left, of the center of the hexagonal patch as indicated by the blue dots in Figure 2.2 (center and right). The various curves of the same color in each plot correspond to side lengths $L = 4, 8, 16, 32$ and 64 (from right to left) of the hexagonal patches. The left panel is for power-law interactions with exponent $\alpha = 1/2$, but results are qualitatively similar for α between 0 and $D/2$. The right panel is for $\alpha = 3/2$, with qualitatively similar behaviour for all $\alpha > D/2$. The unit of time is $1/J$.

on a timescale that is exponentially large in N and, already for moderate system sizes, they do not show up on the timescales plotted in Figure 2.3. In the large N limit, this recurrence time is expected to be pushed to infinity.

2.5 Upper bound on correlations in the thermodynamic limit

Note: Originally, we published upper bounds on the correlation functions for the specific case of a two-dimensional triangular lattice in [116]. Subsequently these ideas have been generalized to arbitrary regular lattice structures in any spatial dimension [61]. This Section is based on the latter and shows an additional relaxation regime that emerges in dimensions $D \geq 3$.

Since the expressions (2.4.2)-(2.4.5) are quasi-periodic in t it is clear that $\langle \sigma_i^x \sigma_j^x \rangle(t)$ does not converge in the long-time limit for any finite lattice. Only in the thermodynamic limit of an infinite number of lattice sites do we have a chance of observing convergence towards an equilibrium value. To derive such a result, we consider regular D -dimensional lattices. Without loss of generality we consider the lattice constants normalised such that there is on average one

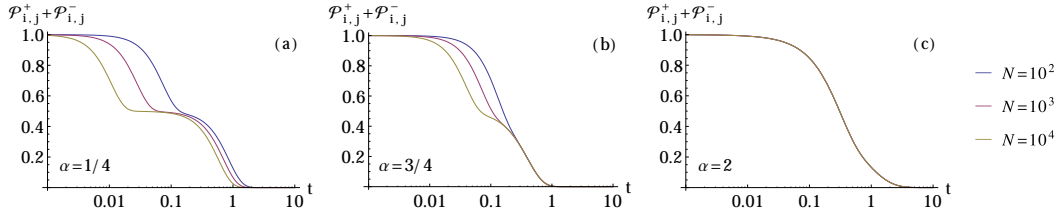


Figure 2.4: Plots of the bound $\mathcal{P}_{i,j}^- + \mathcal{P}_{i,j}^+$ on the normalised correlator $\langle \sigma_i^x \sigma_j^x \rangle(t) / \langle \sigma_i^x \sigma_j^x \rangle(0)$ as a function of time. The examples are for lattice dimension $D = 3$, and the α -values are chosen such that they furnish examples for the three different regimes of relaxation behaviour, as discussed in the text.

lattice site per unit (hyper)volume in the limit of large lattice size. All these bounds are of the form

$$\langle \sigma_i^x(t) \sigma_j^x(t) \rangle, \langle \sigma_i^y(t) \sigma_j^y(t) \rangle \leq \frac{1}{2} (\mathcal{P}_{i,j}^+ + \mathcal{P}_{i,j}^-) \quad (2.5.1)$$

where we define

$$|P_{i,j}^-| \leq \mathcal{P}_{i,j}^- := \begin{cases} \exp \left[-C_{\alpha,D}^- \left(\frac{4\alpha|i-j|t}{\pi} \right)^2 N^{1-2(\alpha+1)/D} \right] & \text{for } 0 \leq \alpha < D/2 - 1, \\ \exp \left[-C_{\alpha,D}^- \left(\frac{4\alpha|i-j|t}{\pi} \right)^{D/(\alpha+1)} \right] & \text{for } \alpha > D/2 - 1, \end{cases} \quad (2.5.2)$$

$$|P_{i,j}^+| \leq \mathcal{P}_{i,j}^+ := \begin{cases} \exp \left[-C_{\alpha,D}^+ \left(\frac{8t}{\pi} \right)^2 N^{1-2\alpha/D} \right] & \text{for } 0 \leq \alpha < D/2, \\ \exp \left[-C_{\alpha,D}^+ \left(\frac{8t}{\pi} \right)^{D/\alpha} \right] & \text{for } \alpha > D/2, \end{cases} \quad (2.5.3)$$

with positive constants $C_{\alpha,D}^+$ and $C_{\alpha,D}^-$ as defined in (B.1.20) and (B.1.21). The proof of the inequalities (2.5.2) and (2.5.3) can be found in appendix B.1.

Depending on the value of α , the bounds (2.5.2) and (2.5.3) decay like stretched or compressed exponentials. By numerically evaluating the exact expressions (2.4.2)-(2.4.5), we find that the functional form of the bound agrees well, although the numerical constants in the bound overestimate, as expected, the exact values. From (2.5.2) and (2.5.3) one can read off that there are three different regimes of α -values, each with a different relaxation or scaling behaviour:

$$0 \leq \alpha < D/2 - 1: \quad |P_{i,j}^-| \text{ and } |P_{i,j}^+| \text{ both decay like a Gaussian in time,}$$

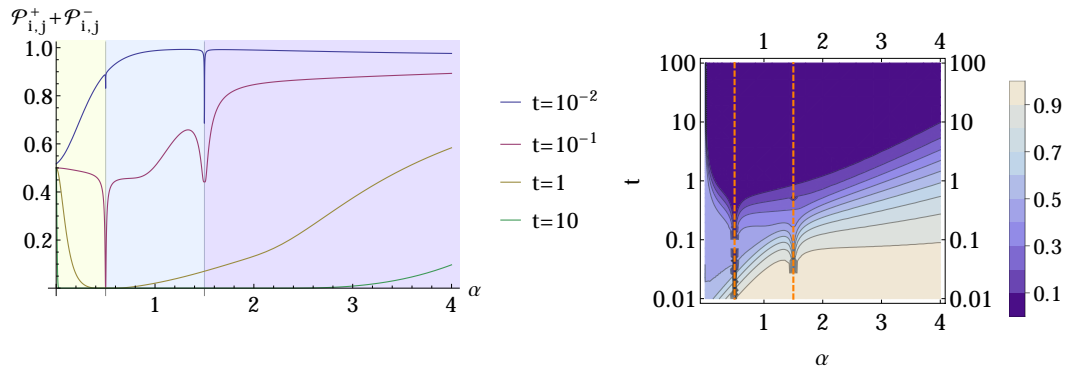


Figure 2.5: Left: For fixed instances of time, the bound $\mathcal{P}_{i,j}^- + \mathcal{P}_{i,j}^+$ is shown as a function of the exponent α . The different shaded regions correspond to the three ranges of α -values discussed in the text. Right: Contour plot of the bound $\mathcal{P}_{i,j}^- + \mathcal{P}_{i,j}^+$ as a function of t and α . The dashed orange lines separate the three regions of α -values discussed in the text. In both figures we chose dimension $D = 3$ and a lattice of $N = 10 \times 10 \times 10$ sites.

and both do so on timescales that are N -dependent. The two timescales of relaxation are widely separated, with $|P_{i,j}^-|$ decaying much slower than $|P_{i,j}^+|$. The form of the resulting upper bound on $\langle \sigma_i^x \sigma_j^x \rangle$ is shown in Figure 2.4(a). This regime occurs for positive α only in lattice dimensions $D \geq 3$.

$D/2 - 1 < \alpha < D/2$: Again, relaxation takes place in a two-step process with widely separated timescales. The fast process described by $|P_{i,j}^+|$ still decays like a Gaussian in time, on a timescale that is N -dependent. The slow timescale corresponding to $|P_{i,j}^-|$ is independent of the system size, with a decay in the form of a compressed exponential. The form of the resulting upper bound on $\langle \sigma_i^x \sigma_j^x \rangle$ is shown in Figure 2.4(b).

$\alpha > D/2$: Both terms $|P_{i,j}^-|$ and $|P_{i,j}^+|$ decay to zero like stretched or compressed exponentials. Relaxation takes place in a single step, as both relevant timescales are very similar and independent of N . The form of the resulting upper bound on $\langle \sigma_i^x \sigma_j^x \rangle$ is shown in Figure 2.4(c).

Figures 2.5 (left and right) show further graphical representations of the bound, highlighting in particular the qualitative changes that occur upon variation of the exponent α .

The stretched or compressed exponential relaxation of the long-range in-

teracting Ising model (2.1.2) discussed above is different from the exponential decay of correlations known to occur in the nearest neighbour Ising model [14]. In the limit $\alpha \rightarrow \infty$ of the power-law interactions, one would usually expect to approach the nearest neighbour interacting model and recover exponentially decaying correlations, however this does not seem to be the case. This puzzle is resolved by observing that, in the limit $\alpha \rightarrow \infty$, the argument of the exponential in (2.5.2) diverges, implying that the bound is not meaningful in this limit.

2.6 Prethermalization

Apart from the overall relaxation times, there are other striking α -dependent aspects of the relaxation dynamics. The plot in the right panel of Figure 2.3, representative for exponents $\alpha \geq D/2$, shows a simple relaxation to equilibrium with a single relevant timescale. The plot in the left panel of Figure 2.3, representative for $0 \leq \alpha \leq D/2$, differs considerably. In a first step, the correlation functions $\langle \sigma_i^x \sigma_j^x \rangle$ and $\langle \sigma_i^y \sigma_j^y \rangle$ display a Gaussian decay on a fast timescale τ_1 to one half of the $\langle \sigma_i^x \sigma_j^x \rangle$ initial value, before finally relaxing to their vanishing equilibrium value on a much longer timescale τ_2 . The fast timescale τ_1 is roughly the same as the timescale on which single-spin observables (green lines in Figure 2.3) relax, while correlations are not yet equilibrated. The system then remains *prethermalized* [82] for a relatively long period of time (notice the logarithmic scale of the time axes), a behaviour observed in the left panel of Figure 2.3 as a noticeable plateau (long-lived quasi-stationary state).

Different from previous observations of prethermalization in quantum dynamics, the ratio τ_1/τ_2 goes to zero in the large $|\Lambda| = N$ limit. This implies that the separation of timescales becomes more pronounced (i.e. a longer plateau) with increasing system size. Such a behaviour of N -dependent relaxation timescales have previously been observed in classical long-range interacting systems, either for mean-field-type spin models [119], or for self-gravitating systems in the astrophysical context [33]. Besides the large N limit, also the $\alpha \rightarrow 0$ limit leads to a more pronounced separation of timescales in the long-range interacting Ising model. In the $\alpha \rightarrow 0$ limit the slow relaxation timescale τ_2 diverges, whereas the fast timescale τ_1 remains finite for finite N . This fact

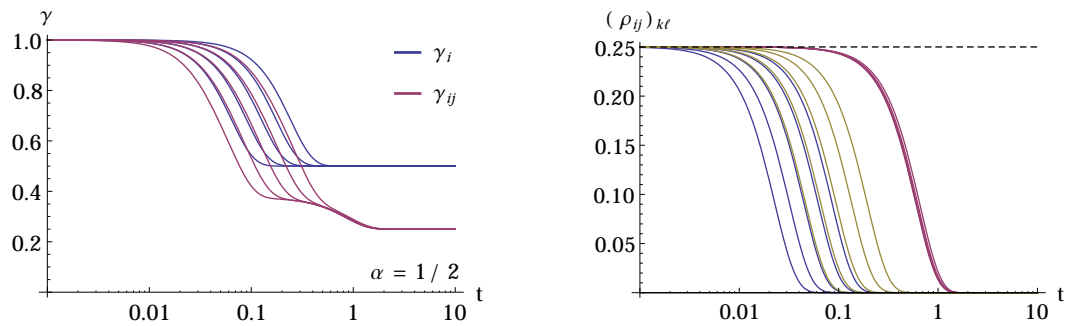


Figure 2.6: Curves of the same colour correspond to side lengths $L = 4, 8, 16, 32, 64$ (from right to left) of the hexagonal patches of triangular lattices. Left: Time evolution of the single- and two-spin purities γ_i and γ_{ij} as defined in (2.6.1). Each relaxation step in the two-spin correlation functions in Figure 2.3 corresponds to a drop in purity. Right: Time evolution of the modulus of the matrix elements of the two-spin reduced density matrix (2.6.4). The black dashed line shows the diagonal elements (2.6.7), blue shows (2.6.8), purple represents (2.6.9) and yellow shows (2.6.11).

can be explained by the presence of $N(N - 1)$ additional symmetries in the $\alpha = 0$ case, where all operators $\sigma_i^x \sigma_j^x + \sigma_i^y \sigma_j^y$ commute with the Hamiltonian (2.1.2). Although these symmetries are absent for $\alpha > 0$, the slow timescale τ_2 can be seen as a remnant of the weakly destroyed $\alpha = 0$ symmetry. While two-spin correlations exhibit relaxation in a two-step process for $\alpha < D/2$, no third timescale emerges for three-spin correlators. In general only even-spin correlations show a two-step relaxation process, while odd-spin correlations relax in a single timescale.

Multiple timescales of relaxation may emerge for various reasons. One possible scenario that has been observed previously, both in theory and experiment [41], is that dephasing is responsible for prethermalization, while a collisional mechanism causes relaxation on a slower timescale through the redistribution of occupation numbers. In order to test which of these mechanisms is at work in the long-range interacting Ising model we compute the time evolution of the n -spin purity

$$\gamma_{i_1, \dots, i_n}(t) = \text{Tr} [\rho_{i_1, \dots, i_n}^2(t)] \quad (2.6.1)$$

where

$$\rho_{i_1, \dots, i_n} = \text{Tr}_{\Lambda \setminus \{i_1, \dots, i_n\}} \rho \quad (2.6.2)$$

is the n -spin reduced density operator, as obtained by tracing the density

CHAPTER 2. LONG-RANGE INTERACTING QUANTUM ISING MODEL 32

operator ρ over all sites of the lattice Λ except i_1, \dots, i_n . The purity can take any value from $1/D$ and 1 which respectively indicate maximally entangled and pure product states. Knowledge of the single-spin expectation values $s_i^a = \langle \sigma_i^a \rangle$ with $a \in \{x, y, z\}$ allows for the reconstruction of the single spin reduced density matrix,

$$\rho_i = \frac{1}{2} \begin{pmatrix} 1 + s_i^z & s_i^x + i s_i^y \\ s_i^x - i s_i^y & 1 - s_i^z \end{pmatrix}. \quad (2.6.3)$$

Additional knowledge of the two-spin correlation functions $s_{i,j}^{ab}$ with $a, b \in \{x, y, z\}$ facilitates the reconstruction of the two-spin reduced density matrix,

$$\rho_{i,j} = \frac{1}{4} \begin{pmatrix} 1 + s_i^z + s_j^z + s_{ij}^{zz} & s_j^x - i s_j^y + s_{ij}^{zx} - i s_{ij}^{zy} & s_i^x - i s_i^y + s_{ij}^{xz} - i s_{ij}^{yz} & s_{ij}^{xx} - s_{ij}^{yy} - i s_{ij}^{xy} - i s_{ij}^{yx} \\ & 1 + s_i^z - s_j^z - s_{ij}^{zz} & s_{ij}^{xx} + s_{ij}^{yy} + i s_{ij}^{xy} - i s_{ij}^{yx} & s_i^x - i s_i^y - s_{ij}^{xz} + i s_{ij}^{yz} \\ & \text{h.c.} & 1 - s_i^z + s_j^z - s_{ij}^{zz} & s_j^x - i s_j^y - s_{ij}^{zx} + i s_{ij}^{zy} \\ & & & 1 - s_i^z - s_j^z + s_{ij}^{zz} \end{pmatrix} \quad (2.6.4)$$

Inserting the exact results for the time dependent spin-spin correlation function of the long-range interacting Ising model [see (2.4.2)-(2.4.5)] into (2.6.3) and (2.6.4), we readily obtain the time evolved single- and two-spin reduced density operators, these in turn can then be used to determine the time dependent purity. As can be seen in Figure 2.6 (left), both relaxation steps of the two-spin correlations that we observe in Figure 2.3, turn out to be associated with a drop in purity γ_{ij} . This indicates that both relaxation steps are caused by dephasing.

In order to demonstrate dephasing more clearly, we study the modulus of the off-diagonal terms of the two-spin reduced density matrix (2.6.4) in the σ^z tensor product eigenbasis. In the case of vanishing magnetic field $h = 0$ and the σ^x tensor product initial state (2.4.1), we have

$$s_i^y = s_i^z = s_{ij}^{xy} = s_{ij}^{xz} = s_{ij}^{yx} = s_{ij}^{zx} = s_{ij}^{zz} = 0 \quad (2.6.5)$$

for all times t . With this simplification and the additional symmetries

$$s_i^a = s_j^a, \quad s_{ij}^{ab} = s_{ij}^{ba} \quad (2.6.6)$$

only four of the original 16 matrix elements of $\rho_{i,j}$ have defined moduli,

$$|(\rho_{i,j})_{kk}| = 1/4 \quad \forall k \in \{1, 2, 3, 4\}, \quad (2.6.7)$$

$$|(\rho_{i,j})_{14}| = |(\rho_{i,j})_{41}| = |s_{ij}^{xx} - s_{ij}^{yy}|/4 = P_{ij}^+/2, \quad (2.6.8)$$

$$|(\rho_{i,j})_{23}| = |(\rho_{i,j})_{32}| = |s_{ij}^{xx} + s_{ij}^{yy}|/4 = P_{ij}^-/2, \quad (2.6.9)$$

$$|(\rho_{i,j})_{12}| = |(\rho_{i,j})_{13}| = |(\rho_{i,j})_{21}| = |(\rho_{i,j})_{24}| = |(\rho_{i,j})_{31}| = |(\rho_{i,j})_{34}| \quad (2.6.10)$$

$$= |(\rho_{i,j})_{24}| = |(\rho_{i,j})_{43}| = |s_i^x + i s_{ij}^{yz}|/4. \quad (2.6.11)$$

The moduli of these matrix elements have been plotted in Figure 2.6 (right) for several sizes of hexagonal patches with internal triangular lattices. All non-diagonal matrix elements decay to zero, but they do so on two different timescales. The matrix elements $(\rho_{ij})_{23}$ and $(\rho_{ij})_{32}$ are given by $P_{ij}^-/2$ and therefore decay on the longer of the two timescales we had previously observed. All other non-diagonal matrix elements decay on faster, N -dependent timescales. This demonstrates that both steps of the two-step relaxation process we observe for two-spin correlation functions in Figure 2.3 are caused by dephasing. Since all the diagonal terms $(\rho_{i,j})_{kk}$ involve expectation values of σ_i^z or the identity, they remain constant throughout the time evolution. This implies that no redistribution of occupation numbers takes place. Such a redistribution would signal collisional relaxation due to inelastic scattering processes between these modes. However, since the long-range interacting Ising Hamiltonian (2.1.2) has only commuting terms, no inelastic collisional mechanism is available.

2.7 Application to trapped ion quantum simulators

Long-range Ising interactions between effective two-level or spin systems can be implemented in crystalline arrays of trapped ions [13]. Spin dependent optical potentials are used to modify the Coulomb interaction energy of the trapped ions and generate an effective Ising interaction. With small numbers of ions in linear radio-frequency traps, long-range Ising interactions such as those in (2.1.2) are the basis of quantum gates, and have been implemented with high fidelity (>98%). These techniques have recently been extended to

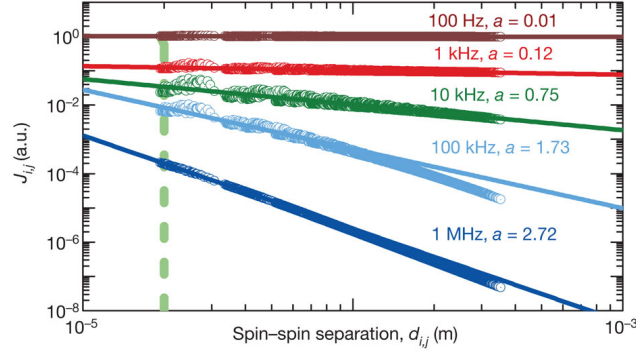


Figure 2.7: (Taken from [13]) Theoretical predictions of interaction strength $J_{i,j}$ plotted as a function of the separation distance between ions at lattice sites i and j for a hexagonal lattice consisting of 217 sites. Straight lines show power-law fits to the data.

single-plane triangular lattices of several hundred ions stored in a Penning trap. To date, the Ising interactions implemented in the Penning ion trap simulator have been benchmarked for short timescales through comparison with mean-field theory [13], a classical limit of the long-range interacting Ising Hamiltonian (2.1.2) where quantum fluctuations and correlations are ignored. The exact results on correlation functions, (2.4.5)-(2.4.5), will enable a much higher level of benchmarking, and a determination of the timescales over which the expected emulation of quantum effects of an Ising model is indeed realized.

Application of the results shown in the previous sections for the ion trap simulators required initial states that are diagonal in the σ^x tensor product eigenbasis, and assurance that the trapped ion simulator is an isolated quantum system for the quantum many-body equilibration timescales associated with the upper bounds on two-spin correlation functions $\mathcal{P}_{i,j}^\pm$ discussed in Section 2.5. Preparation of the diagonal states in the σ^x tensor product eigenbasis is straightforward in ion traps. Specifically, optical pumping and coherent control techniques can initialize each spin to point along the x -axis with high fidelity. In the Penning ion trap simulator this initialization can be done with a fidelity greater than 99% [10]. Equilibration timescales \mathcal{P}_{ij}^\pm [see equations (2.5.2) and (2.5.3)] that are short compared with other relaxation timescales have been demonstrated with 10-20 ions in linear radio-frequency traps [63, 32, 52, 72]. In the current Penning ion trap simulator [13], spontaneous emission from the off-resonant laser beams used to engineer the long-range Ising interaction sets

an experimental relaxation timescale that is comparable to the quantum many-body equilibration timescales. However, with straightforward improvement to the setup described in [13], the quantum many-body relaxation timescales can be short compared to the spontaneous emission timescale. Specifically, with $N = 217$ ions and an optical dipole force generated from two 10 mW beams crossing with an angular separation of 35° (see Figure 1 in [13]) and frequency difference tuned to generate $\alpha = 1/2$ power-law interactions, we calculate the two relaxation timescales $\mathcal{P}_{i,j}^\pm$ to be $\approx 30 \mu\text{s}$ and $\approx 430 \mu\text{s}$. Here i and j are chosen to be one site to the left and right of the center site as shown in Figure 2.2 (center and right). The spontaneous emission time for this configuration is $(1/\Gamma) \sim 4 \text{ ms}$. All of these timescales are short compared to the $T_2 \gtrsim 50 \text{ ms}$ coherence time of Be^+ valence electron spin qubits.

To compare with exact results reported here requires an experimental measurement of two-spin correlation functions after the Ising interaction has been applied for a variable period. This is readily accomplished with trapped ions by using spin-dependent resonance fluorescence. Britton et al. [13] use spin-dependent resonance fluorescence to measure spin orientation in the σ^z basis. With resolved imaging of the array of ions [see Figure 2.2 (left)], the spin orientation of each ion can be detected and arbitrary pair correlation functions calculated. However, more simply, the global fluorescence detected from all the ions in the array can be used to measure the global spin state of the system (the total number of spins in the $|\uparrow\rangle$ state and the total number of ions in the $|\downarrow\rangle$ state). Shot-to-shot fluctuations in these measurements are sensitive to the second-order moment $\langle S_z^2 \rangle$ of the total z -component of the spin $S_z = \sum_{i \in \Lambda} \sigma_i^z$. Of particular interest are measurements of the second-order moments in directions perpendicular to the mean composite spin vector,

$$\langle \boldsymbol{\sigma} \rangle = \sum_{i \in \Lambda} (\langle \sigma_i^x \rangle, \langle \sigma_i^y \rangle, \langle \sigma_i^z \rangle). \quad (2.7.1)$$

For example, with all spins initially pointing along the x -axis, fluctuations of measurements of J_z after rotation about the x -axis by an angle θ are sensitive to

$$\langle S_z^2 \rangle_\theta = \sum_{i,j \in \Lambda} [\sin^2 \theta \langle \sigma_i^y \sigma_j^y \rangle - \sin \theta \cos \theta \langle \sigma_i^y \sigma_j^z + \sigma_i^z \sigma_j^y \rangle + \cos \theta \langle \sigma_i^z \sigma_j^z \rangle]. \quad (2.7.2)$$

These so-called spin squeezing measurements [115] are sensitive to pairwise correlations summed over all the spins in the ensemble. In the following section we study spin squeezing and other measures of entanglement that emerge in the long-range interacting Ising model which confirm, without an inkling of doubt, the quantum nature of the model.

2.8 Entanglement in far-from-equilibrium quantum magnetism

In this section we calculate several time dependent entanglement measures within the long-range interacting Ising model. This allows us to compare the dynamics of several different types of entanglement, each of which can evolve qualitatively differently. Although each entanglement measure quantifies some kind of quantum correlations, there are many types of inequivalent entanglement [49]. Each type can be harnessed for capabilities beyond those provided by classical states, but different types of entanglement require different protocols to harness. In addition to their ability to quantify quantum resources, these entanglement measures generate great interest in their connection to many-body physics, where they help to classify and understand the structure of many-body phases of matter and dynamics [19].

The long-range interacting Ising model furnishes concrete examples of different types of entanglement possessing qualitatively different dynamics. To illustrate this, it suffices to consider the all-to-all coupling limit,

$$\alpha = 0, \quad J_{i,j} = J \tag{2.8.1}$$

for all i and j , also known as the one-axis twisting Hamiltonian. In this model for initial states fully aligned along the x -axis, spin squeezing (a measure of multipartite entanglement) emerges at short times, while Greenberger-Horne-Zeilinger (GHZ) entanglement occurs at later times (more discussion and definitions are given below). Spin squeezed states may be used to perform quantum-enhanced metrology of spin energy splittings using Ramsey spectroscopy, while utilizing GHZ-entangled states requires a Ramsey pulse sequence with a final readout using another observable, for example the spin

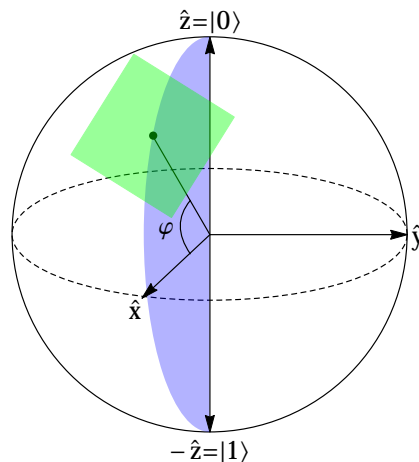


Figure 2.8: Schematic showing the tipping angle φ restricted to the xz -plane together with a surface perpendicular to the spin direction. Spin squeezing can be thought of as the minimum uncertainty perpendicular to the mean spin direction.

parity. With the analytic results of the previous sections we are able to quantify these and other types of entanglements' time evolution, and their dependence on other experimental parameters. This allows us to determine which factors are favorable or detrimental for creating different types of entanglement, and hence for application to different quantum-enhanced applications.

We study the dependence of different entanglement measures on the initial state $|\Psi(0)\rangle$ and range of interaction α . For simplicity we consider one-dimensional lattices (i.e., chains), but our qualitative conclusions do not depend on the latter assumption and should hold for any dimension. Homogeneous *product initial states* (see Section 2.3) are chosen, given by

$$|\Psi(0)\rangle = \bigotimes_{j \in \Lambda} \left(e^{i\phi_j/2} \cos \frac{\theta_j}{2} |\uparrow\rangle_j + e^{-i\phi_j/2} \sin \frac{\theta_j}{2} |\downarrow\rangle_j \right) \quad (2.8.2)$$

with $\phi_j = 0$ and $\theta_j = \varphi$ for all j . In this way we restrict the initial state to consist of products of states on the xz -plane of the Bloch sphere (see Figure 2.8). We study the formation of entanglement as a function of two parameters, the global tipping angle φ and the interaction exponent α .

Note: This Section is based on the author's contribution to [46].

2.8.1 Spin squeezing

Spin squeezing was introduced by Kitagawa and Ueda [65] to quantify the usefulness of a quantum state for quantum metrology using a Ramsey protocol. A squeezed state is necessarily entangled, and in addition to its use as an entanglement witness [68] and for quantifying quantum metrological resources, it is appealing for its clear physical meaning and relatively straightforward potential to measure. It also is simple in the sense that, in order to calculate it, only the single- and two-spin correlation functions are required, which allows us to use the results of Sections 2.2 and 2.3. We define the squeezing in decibels as

$$\text{dB squeezing} = -10 \log_{10} \xi \quad (2.8.3)$$

with

$$\xi = \min_{\hat{n}_\psi} \frac{\sqrt{N} \sqrt{\langle (\boldsymbol{\sigma} \cdot \hat{n}_\psi)^2 \rangle - \langle \boldsymbol{\sigma} \cdot \hat{n}_\psi \rangle^2}}{|\langle \boldsymbol{\sigma} \rangle|}, \quad (2.8.4)$$

where $\boldsymbol{\sigma} = \sum_{i \in \Lambda} (\sigma_i^x, \sigma_i^y, \sigma_i^z)$ the vector of Pauli operators. The minimization is over unit vectors \hat{n}_ψ perpendicular to the mean spin direction. For details of the calculation see appendix D. The dB squeezing is an entanglement witness: when dB squeezing is positive, the state is squeezed and entangled.

In [65] Kitagawa and Ueda discussed spin squeezing for the one-axis twisting (OAT) Hamiltonian $H_{\text{OAT}} = \frac{1}{2} J (\sigma^z)^2$, corresponding to the $\alpha = 0$ case of the long-range interacting Ising model (2.1.2). The OAT Hamiltonian generates spin squeezed states at short times, a fact that has been confirmed in a number of experiments [42, 27]. Theoretically, entangled GHZ-states have been shown to occur at longer times [84].

Figure 2.9 (left) shows a contour plot of dB squeezing in the (α, t) -plane, starting from a fully x -polarized, $\varphi = \pi/2$ initial state. Increasing the interaction exponent α leads to a slower and weaker creation of entanglement, but also to a longer lifetime of the squeezed state. While this α dependence is substantial for $\alpha < D$ it becomes weaker for $\alpha > D$.

Figure 2.9 (right) shows dB spin squeezing in the (φ, t) -plane for $\alpha = 3/4$.

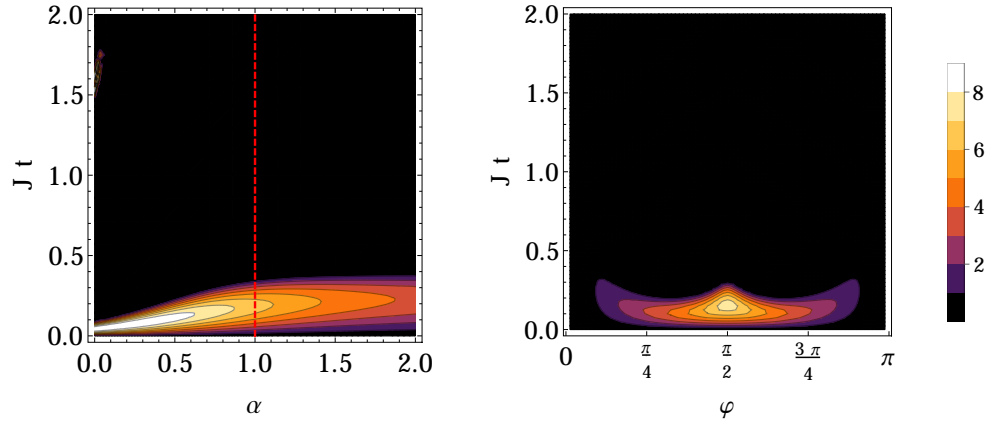


Figure 2.9: Contour plots of decibel spin squeezing in a long-range Ising chains with $L=41$ lattice sites. Left: dB spin squeezing as a function of the interaction exponent α with initial tipping angle $\varphi = \pi/2$. Right: dB spin squeezing as a function of tipping angle φ for $\alpha = 3/4$.

Maximal spin squeezing occurs for a tipping angle $\varphi = \pi/2$. This implies that a fully x -polarized initial state (or any fully polarized state in the x - y plane) is the ideal choice for creating squeezed states under time evolution. As the tipping angle is decreased to around $\varphi = \pi/4$, spin squeezing emerges, but grows to a smaller maximum than at $\varphi = \pi/2$ and then disappears rather quickly. This can be understood by noting that correlations $\langle \sigma_i^a \sigma_j^z \rangle$ containing a z -component build up quickly which in turn reduce spin squeezing, as illustrated in Figure 2.10 and Equation (D.1.11) of appendix D. Finally, further decreasing φ , the squeezing decreases, approaching zero when the mean spin

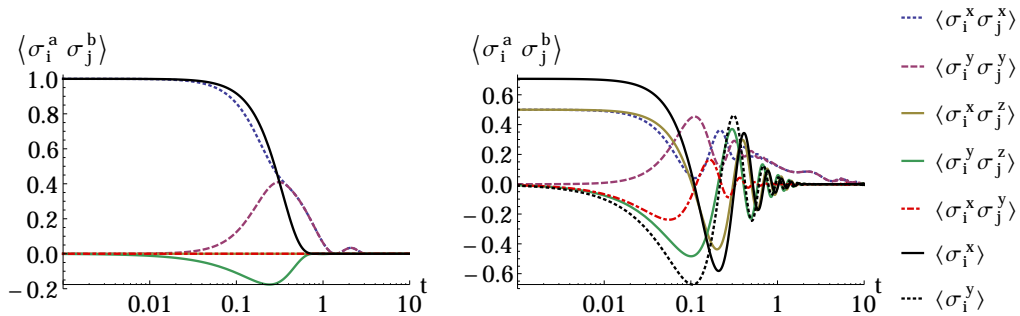


Figure 2.10: Time evolution of the normalized two-spin correlation functions $\langle \sigma_i^x \sigma_j^x \rangle$, $\langle \sigma_i^y \sigma_j^y \rangle$, $\langle \sigma_i^x \sigma_j^y \rangle$, $\langle \sigma_i^x \sigma_j^z \rangle$ and $\langle \sigma_i^y \sigma_j^z \rangle$ for a long-range interacting Ising chain consisting of 41 lattice sites. The interaction exponent is $\alpha = 1/4$, with initial tipping angles $\varphi = \pi/4$ (left) and $\varphi = \pi/2$ (right). Lattice sites i and j are chosen one lattice spacing to either side of the center of the chain.

direction points along the z -axis ($\varphi \rightarrow 0$). Furthermore, the time at which the small amount of squeezing is created for small φ increases as φ decreases, giving the appearance of “horns” in the contour plot in Figure 2.9 (right).

2.8.2 Entanglement entropy

We define the entanglement entropy between a subregion \mathcal{R} and the rest of the system by

$$S_{\mathcal{R}} = -\text{Tr}(\rho_{\mathcal{R}} \log_2 \rho_{\mathcal{R}}), \quad (2.8.5)$$

where $\rho_{\mathcal{R}}$ is the reduced density matrix of the subregion \mathcal{R} , obtained by tracing out all those parts of the Hilbert space not associated with \mathcal{R} . The \log_2 convention is convenient since it quantifies the amount of entanglement in bits. With this convention, the maximum bipartite entanglement between the system and subsystem is equal to the number of spins in the subsystem. The entanglement entropy is a measure of the total entanglement of bipartite pure states (although even un-entangled mixed states have finite entanglement entropy) and is widely used in quantum information theory. Its physical meaning has been nicely summarized by Latorre and Riera [73], stating that

“The entanglement entropy quantifies the amount of surprise that a sub-part of a system finds when discovering that it is correlated with the rest of the system”.

We will consider subregions $\mathcal{R}_{ij} \equiv \{i, j\}$, consisting of pairs of (not necessarily neighboring) spins i and j . The reduced density matrix is given by

$$\rho_{\mathcal{R}_{ij}} = \frac{1}{4} \sum_{a,b \in \{0,x,y,z\}} \langle \sigma_i^a \sigma_j^b \rangle \sigma_i^a \sigma_j^b, \quad (2.8.6)$$

with the convention that σ_i^0 is the 2×2 identity matrix at lattice site i . From this expression it becomes obvious that the exact results for the single- and two-spin correlation functions [see equations (2.4.2)-(2.4.5)] allow us to also obtain exact results for the entanglement entropy of subregions \mathcal{R}_{ij} .

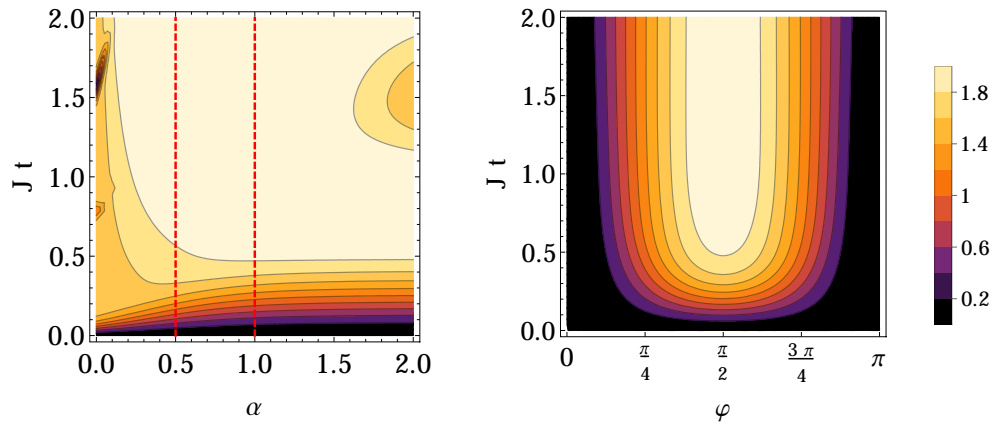


Figure 2.11: Contour plots of entanglement entropy for a long-range Ising chain with $L=41$ lattice sites. Left: entanglement entropy as a function of the interaction exponent α with initial tipping angle $\varphi = \pi/2$. Right: entanglement entropy as a function of tipping angle φ for $\alpha = 3/4$.

Heuristically, if we increase the tipping angle φ away from the fully x -polarized state, we increase the z -component of the mean spin direction. Since components pointing along the z -axis are conserved under the Ising time evolution, they will not contribute to the formation of entanglement. Hence, as we move the tipping angle away from the fully x -polarized state at $\varphi = \pi/2$, we expect the entanglement entropy to saturate at a lower level. This intuition is confirmed by Figure 2.11 (right), where we have chosen \mathcal{R}_{ij} as consisting of the sites adjacent (one to the left and one to the right) of the center spin of a chain with 41 sites.

Figure 2.11 (left) shows a contour plot of the entanglement entropy in the (α, t) -plane. The entanglement entropy evolution is qualitatively different depending on whether α is less or greater than $D/2$. For $\alpha < D/2$ two widely separated timescales are observed. On a short timescale a long lived quasi-stationary state (or “prethermalization plateau”) [116] of intermediate entanglement strength is formed, while larger entanglement is built up only on a much longer timescale. This effect is enhanced when increasing the number of lattice sites, or when further reducing α . For $\alpha > D/2$ no such separation of timescales is visible. When $\alpha > D$ the single- and two-spin correlation functions begin to show oscillatory behaviour. These oscillations become more pronounced for greater values of α and can also be observed in the (α, t) -plane for $\alpha \gtrsim 1.5$.

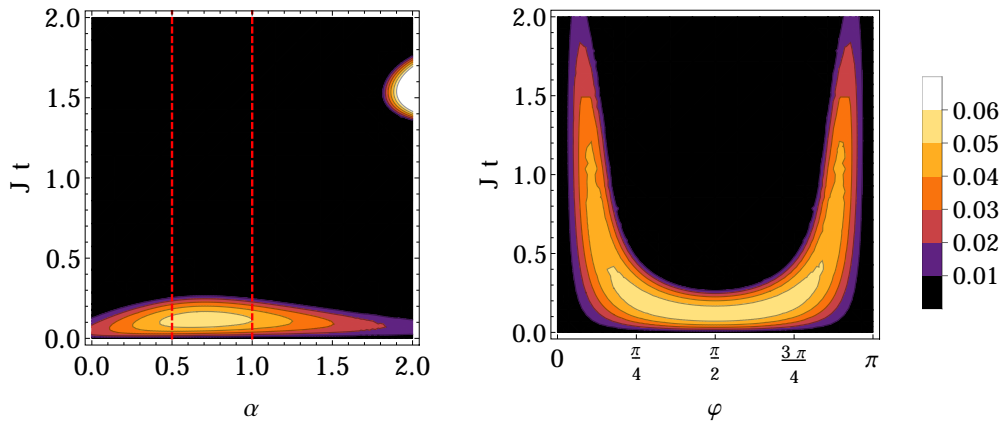


Figure 2.12: Contour plots of concurrence for a long-range Ising chain with $L=41$ lattice sites. Left: concurrence as a function of the interaction exponent α with initial tipping angle $\varphi = \pi/2$. Right: concurrence as a function of tipping angle φ for $\alpha = 3/4$.

2.8.3 Concurrence

Concurrence was introduced in [118] as an entanglement measure for two-qubit systems. It is defined as

$$\mathcal{C}(\rho) \equiv \max \{0, \lambda_1 - \lambda_2 - \lambda_3 - \lambda_4\} \quad (2.8.7)$$

where $\lambda_1, \dots, \lambda_4$ are the square roots of eigenvalues (in decreasing order) of the non-Hermitian matrix $\rho_{\mathcal{R}_{ij}} \sigma_i^y \sigma_j^y \rho_{\mathcal{R}_{ij}}^* \sigma_i^y \sigma_j^y$. Generalizations beyond the two-qubit case have been reported in [48].

Figure 2.12 (left) shows a contour plot of the concurrence in the (α, t) -plane for a fully x -polarized, $\varphi = \pi/2$ initial state. At $\alpha = D/2$ the concurrence reaches its maximum value and also persists for the longest time. Figure 2.12 (right) shows the concurrence in the (φ, t) -plane for $\alpha = 3/4$. As for other entanglement measures, the maximum value is achieved at $\varphi = \pi/2$. Away from this value, growth of concurrence is weaker and slower, leading to “horns” which are more pronounced but similar to those for squeezing [see Figure 2.9 (right)].

2.9 Summary and conclusions

Under convenient restrictions to the initial conditions, we have obtained exact analytic results for any order correlation function of the long-range interacting Ising model in arbitrary spacial dimension and for any lattice structure. This simple, yet quantum, model shows prethermalization, widely separated timescales, and formation of different types of entanglement that further our understanding of the timescales governing the relaxation to equilibrium.

For all of the entanglement measures studied, we find a pronounced change of behavior upon variation of the exponent α . Depending on the chosen entanglement measure this change may occur at $\alpha = D/2$ as in the case of concurrence, or at $\alpha = D$ as for the decibel spin squeezing. Independent of the measure of entanglement, a fully polarized initial state in the x - y plane ($\varphi = \pi/2$) is always optimal for the creation of maximum entanglement under unitary time evolution governed by the long-range interacting Ising model.

The analytic results of this chapter can be directly compared to experimental measurements of two-spin correlation functions. This will enable a much higher degree of benchmarking of trapped ion quantum simulators [13] in a regime where quantum effects are paramount. Subsequently, once the trapped ion quantum simulator is benchmarked, it may in turn be used for testing approximate calculations of the quantum dynamics of the long-range interacting Ising model in the presence of transverse fields that result in non-commuting terms in the Hamiltonian (2.1.2) [44]. Moreover, there are certain phenomena which are believed to be peculiar to long-range interacting systems and which might receive their first experimental verification in the ion trap setup. One example is the threshold at $\alpha = D/2$ below which a second timescale of relaxation emerges. There is evidence that not only the existence of this dynamical long-range threshold, but also its numerical value $D/2$, is universal for classical as well as quantum mechanical long-range interacting systems [6]. Other long-range peculiarities include non-equivalent equilibrium statistical ensembles [58, 57], a phenomenon that has been known in the astrophysical context for decades [112] but has not seen experimental verification.

Chapter 3

Supersonic spreading of correlations in long-range quantum lattice models

In this chapter we study the non-equilibrium dynamics of two-spin correlations in quantum lattice models in the presence of long-range interactions decaying as a power law in separation distance $|i - j|^{-\alpha}$. For exponents α larger than the lattice dimension D , a Lieb-Robinson bound [74, 43] effectively restricts the spreading of correlations to the interior of a causal region (or sound cone), but allows supersonic (*faster than linear*) propagation (see Section 1.1.3 for details). In this chapter we show that this decay is not only sufficient but also necessary.

In Section 3.1 we introduce a dictionary between non-equilibrium systems and quantum channels. Borrowing methods from quantum metrology, for any exponents α smaller than the lattice dimension, we construct in Section 3.2 a toy Hamiltonian giving rise to quantum channels with capacities not restricted to any causal region. The analytic results of the long-range interacting Ising model (see Chapter 2) are used, in Section 3.3.1 to illustrate the breakdown of the causal region, i.e. distance independent spreading of correlations and information, for sufficiently small α . Section 3.3.2 shows numerical results obtained using matrix product state methods for the XXZ spin chain revealing the presence of a sound cone for large exponents, and supersonic propagation

for small ones. In all models we analyzed the fast spreading of correlations follows a power law, and not the exponential increase of the long-range Lieb-Robinson bound. Section 3.4 highlights comparisons with current experimental results.

Note: This chapter is mostly based on [25] but contains elements of [109].

3.1 Non-equilibrium systems as quantum channels

A natural way to capture information propagation is to use concepts from channel capacities of quantum channels. A quantum channel is a communication channel capable of transmitting quantum (eg. the state of a qubit) as well as classical information (eg. email sent over the internet). Formally, quantum channels are completely positive trace-preserving maps between operator spaces. In the following description we do not intend to give an all encompassing review of quantum channels, our aim is merely to give some intuition regarding the concepts.

As an example, consider the mapping

$$\phi : A \mapsto e^{-iHt} A e^{iHt} \quad (3.1.1)$$

reflecting time evolution. If we take a positive operator $A = B^\dagger B$ we can write

$$\phi(A) = \phi(B^\dagger B) = e^{-iHt} B^\dagger B e^{iHt} = (B e^{iHt})^\dagger (B e^{iHt}) \quad (3.1.2)$$

which is once again a positive operator, and positivity is preserved. Using the cyclic property of the trace,

$$\text{Tr}[\phi(A)] = \text{Tr}[e^{-iHt} A e^{iHt}] = \text{Tr}(A) \quad (3.1.3)$$

it is also clear that the trace is preserved under ϕ . This confirms that unitary evolution is indeed a quantum channel. Similarly any map $A \mapsto U^\dagger A U$ with U a unitary will also be a quantum channel.

Consider a system $\Lambda = X \cup Y$ whose state space is the tensor product

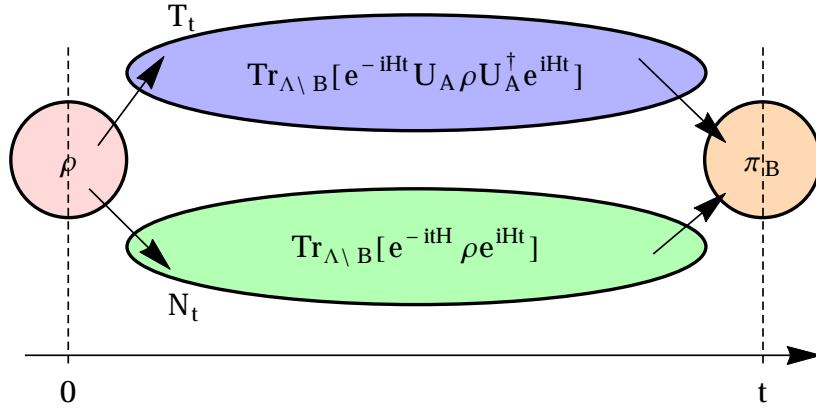


Figure 3.1: Schematic representation of the coding.

$\mathcal{H}_X \otimes \mathcal{H}_Y$ of Hilbert spaces defined on X and Y respectively. The partial trace between spaces of bounded linear operator $B(\mathcal{H}_X \otimes \mathcal{H}_Y)$ and $B(\mathcal{H}_X)$ is given by

$$\text{Tr}_Y : B(\mathcal{H}_X \otimes \mathcal{H}_Y) \rightarrow B(\mathcal{H}_X) : U \otimes V \mapsto U \text{Tr}(V). \quad (3.1.4)$$

Using the same arguments as before you can show that the partial trace is a completely positive trace preserving map.

It trivially follows that the composition of two completely positive trace preserving maps is again a completely positive trace preserving map. This implies that for any unitary U , the map

$$T(\mathcal{H}_X \otimes \mathcal{H}_Y) \rightarrow T(\mathcal{H}_X) : A \mapsto \text{Tr}_Y(U^\dagger A U) \quad (3.1.5)$$

represents a quantum channel. Classical and quantum channel capacities quantify the rate (bits per letter, or channel) at which respectively classical and quantum information can be transmitted reliably through a channel. Quantum capacities are usually less, and can never be greater, than the same channel's classical capacity [9].

For our purpose, a natural choice of capacity is the classical information capacity of the quantum channel. At time $t = 0$ we prepare the system in the state ρ . To implement the quantum channel, we encode a signal on $A \subset \Lambda$, and measure the effect of that encoding after a time t at $B \subset \Lambda$. The coding

amounts to either realizing a quantum channel

$$T_t : \rho \mapsto \text{Tr}_{\Lambda \setminus B} \left(e^{-itH} U_A \rho U_A^\dagger e^{itH} \right) \quad (3.1.6)$$

for $t \geq 0$, where U_A is a local unitary operator non-trivially supported on A only, or

$$N_t : \rho \rightarrow \text{Tr}_{\Lambda \setminus B} \left(e^{-itH} \rho e^{itH} \right) \quad (3.1.7)$$

reflecting time evolution. $\text{Tr}_{\Lambda \setminus B}$ denotes the partial trace over the entire underlying space Λ except for a subset B . Afterwards one performs a measurement associated with a positive-operator valued measure π_B supported on B only, with $0 \leq \pi_B \leq \mathbb{1}$. The classical information capacity C_t can, in the setting considered here, be bounded from below by the probability of detecting a signal at time $t > 0$, so

$$C_t \geq p_t := \left| \text{Tr}[T_t(\rho)\pi_B] - \text{Tr}[N_t(\rho)\pi_B] \right|. \quad (3.1.8)$$

This channel capacity C_t captures the rate (bits per letter, or channel) at which classical bits of information can be reliably transmitted from A to B , by either performing a local unitary U_A at $t = 0$ or not, and detecting the signal in B at a later time.

3.2 Lower bounds on information propagation

Let Λ be an arbitrary lattice of spatial dimension D with open boundary conditions. In order to compare our results with previous literature on Lieb-Robinson bounds of power-law interacting quantum spin systems, we are free to consider any Hamiltonian $H = \sum_{X \subset \Lambda} h_X$, consisting of local Hamiltonian terms h_X with compact support on $X \subset \Lambda$, that satisfies the *boundedness* condition

$$\sum_{X \ni x, y} \|h_X\| \leq \frac{\lambda}{(1 + \text{dist}(x, y))^\alpha} \quad (3.2.1)$$

for some finite positive λ .

In the following subsections we introduce a toy model resembling the long-

range interacting Ising model. Using this model together with product and entangled initial states we determine different threshold values of α below which the spreading of classical information becomes distance independent. The same ideas are also be applied to the full long-range interacting Ising model with single site measurements. These results reveal a threshold value of α below which the spreading of classical information is always faster than linear.

Note: Section 3.2.1 is based on a calculation performed by Jens Eisert in [25]. The details of these calculations were not published but can be found in Appendices C.1 and C.2. Section 3.2.2 extends the ideas of Eisert to the full long-range Ising model.

3.2.1 Supersonic propagation in an Ising-like toy model

For ease of calculation we choose the toy Hamiltonian

$$H_\Lambda = \frac{1}{2}(\mathbb{1} - \sigma_o^z) \sum_{j \in B} \frac{1}{(1 + \text{dist}(o, j))^\alpha} (\mathbb{1} - \sigma_j^z), \quad (3.2.2)$$

resembling the long-range interacting Ising model (2.1.2), where $o \in \Lambda$. As before, σ_j^z denotes the z component of the Pauli spin operator supported on lattice site j . We assume the set $A \subset \Lambda$ consists of the single lattice site $o \in \Lambda$, $A = \{o\}$, so that $|A| = 1$ and take

$$B := \{j \in \Lambda : \text{dist}(o, j) \geq \delta\} \quad (3.2.3)$$

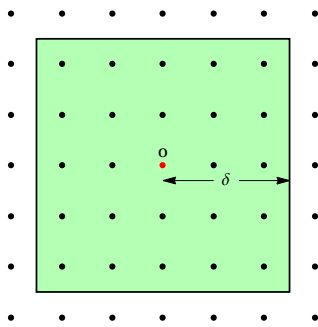


Figure 3.2: Graphical representation of lattice constraint in (3.2.3).

for some $\delta \in \mathbb{N}$, to be the set of all lattice sites in Λ separated from o by a graph distance greater or equal to some positive δ . What makes calculations easier in this toy model is the fact that interactions are limited to spins on A and B only. There is no self-interaction of spins on A , B or the remainder of the lattice sites in $\Lambda \setminus (A \cup B)$. Depending on whether we choose a product or entangled initial state we find different threshold values of α below which the spreading of information becomes distance independent.

3.2.1.1 Product initial state

We choose a *product initial state*

$$\rho = |0\rangle\langle 0|^{\otimes |\Lambda|-|B|} \otimes |+\rangle\langle +|^{\otimes |B|} \quad (3.2.4)$$

with $|+\rangle = (|0\rangle + |1\rangle)/\sqrt{2}$. The first tensor factor corresponds to the complement $\Lambda \setminus B$ of B on the lattice. We choose positive operator valued measure $\pi_B = |+\rangle\langle +|^{\otimes |B|}$ and local unitary $U_A = |1\rangle\langle 0| + |0\rangle\langle 1|$, i.e. the spin flip operator. In these terms, we can write the probability of detecting a signal in B at some time $t > 0$ given the unitary perturbation U_A as (see Appendix C.1 for details)

$$p_t = 1 - \frac{1}{2^{|B|}} \prod_{j \in B} \left[1 + \cos \left(\frac{2t}{(1 + \text{dist}(o, j))^\alpha} \right) \right]. \quad (3.2.5)$$

For short times t such that $2t \leq (1 + \delta)^\alpha$, we obtain (for details, see Appendix C.1)

$$p_t \geq 1 - \exp \left[-\frac{4t^2}{5} \sum_{j \in B} (1 + \text{dist}(o, j))^{-2\alpha} \right]. \quad (3.2.6)$$

For $\alpha < D/2$ and for the product initial states considered the sum that appears in the argument of the exponential in (3.2.6) diverges in the limit of large $|B|$. This implies that for any constant $c \in [0, 1]$ and any sufficiently small time $t > 0$, for a sufficiently large $|B|$ (and lattice), one can always detect a signal $C_t > c$. Signal propagation is therefore not restricted to any causal region, as reliable information can be transmitted arbitrarily fast, beyond any finite speed of information propagation. Even though this seems to contradict the laws of general relativity, in the end information itself cannot propagate faster than the speed of light. Moreover, (3.2.6) implies that starting from a

product initial state of the form (3.2.4) a well defined causal region can be identified for values of α down to $D/2$, i.e. *less than* the dimension of the underlying system. Examples where propagation is faster than linear are also known for lattice systems with nearest-neighbour interactions and infinite-dimensional constituents [23].

3.2.1.2 Entangled initial state

The bound of $\alpha < D/2$ for the breakdown of causality, when starting from product initial states, can be beaten by resorting to ideas of metrology and methods of multi-particle entanglement. Here we show that, precisely for $\alpha \leq D$, the causal region disappears for an entangled initial state. This specific example shows that, in general, the causal region disappears for $\alpha \leq D$. The steps used here are borrowed from quantum phase estimation. We choose an initial state of the form

$$\rho = |0\rangle\langle 0|^{|\Lambda|-|B|} \otimes |\psi\rangle\langle\psi|, \quad (3.2.7)$$

with

$$|\psi\rangle = (|0, \dots, 0\rangle + |1, \dots, 1\rangle)/\sqrt{2}. \quad (3.2.8)$$

That is, the subset $B \subset \Lambda$ of the lattice is prepared in a multi-partite entangled Greenberger-Horne-Zeilinger (GHZ) state, the kind as it is used in error-free phase estimation and metrology [50]. When the system is prepared in this initial state with positive operator measure $\pi_B = |\psi\rangle\langle\psi|$, but otherwise in the same situation as considered before, one finds that the probability of detecting a signal p_t in B at some time $t > 0$ given the unitary perturbation at A is given by (see Appendix C.2 for details)

$$p_t = 1 - \frac{1}{2} \left[1 + \cos \left(t \sum_{j \in B} (1 + \text{dist}(o, j))^{-\alpha} \right) \right]. \quad (3.2.9)$$

Exploiting the asymptotic behavior of the Hurwitz zeta function [89, see Section 25.11] the asymptotic shape of the causal region for this model is found to be of the form

$$p_t \propto t^2 \delta^{2(D-\alpha)}. \quad (3.2.10)$$

Hence, for any $\epsilon > 0$ we have

$$\sqrt{\epsilon} \propto t\delta^{D-\alpha} \quad (3.2.11)$$

which implies

$$\delta \propto t^{1/(\alpha-D)}. \quad (3.2.12)$$

When using a GHZ entangled initial state two distinct α -regimes emerge:

1. When $\alpha < D$ the leading order in the Taylor expansion of p_t diverges and the causal region breaks down, and
2. for $D < \alpha < D+1$, equation (3.2.12) gives rise to a bent causal region and allows for faster than linear propagation of information, but slower than in principle permitted by the power-law Lieb-Robinson bound (1.1.11).

Remarkably, the use of entangled initial states alters the threshold of the exponent α , where causality breaks down, from $D/2$ to the optimal value of D . On arbitrary lattices, and precisely for $\alpha > D$, the Lieb-Robinson bound of Hastings and Koma (1.1.10) sets in and defines a causal region. For $\alpha \leq D$, in contrast, models can be identified that exhibit no causal region at all. This observation does not mean that the Hamiltonian is unphysical, it only implies that, for algebraically decaying interactions, the familiar picture of the existence of causal regions can be drastically altered. These results also generalize and complete the findings of [44] (where, for $D = 1$ and $\alpha < 1$, also instances of instantaneous transmission of information have been observed) and complement recent insights into the growth of the mutual information and bi-partite entanglement following quenches [104]. In Chapter 4 we extend Lieb-Robinson bounds to the $\alpha < D$ case.

3.2.2 Supersonic propagation in the full long-range Ising model

In the previous section it was proved that information can be transferred supersonically through a quantum channel for any $\alpha < D + 1$, while no such

proof exists for $\alpha > D + 1$. However, this result required the measurement of observables supported on semi-infinite sub-lattices, which is not a very physical scenario. In this section we show that supersonic transmission through a quantum channel can occur in any dimension for $\alpha < 2$ for measurements performed on single lattice sites. What is more, we extend the time evolution with respect to the full long-range interacting Ising model, not just the simplified toy model of the previous section.

Let $\Lambda = \{1, \dots, N\}$ be a finite, one dimensional lattice consisting of N sites. On this lattice define an Ising Hamiltonian with arbitrary couplings

$$H = \frac{1}{2} \sum_{i < j} J_{ij} \sigma_i^z \sigma_j^z \quad (3.2.13)$$

with σ_j^z the z Pauli matrix on lattice site j . Define the sub-lattices $A = \{1\}$, $B = \{N\}$ and $S = \Lambda \setminus (A \cup B)$. Using this notation the Hamiltonian (3.2.13) can be rewritten as

$$H = H_{AS} + H_{AB} + H_{SB} + H_{SS} \quad (3.2.14)$$

with

$$H_{XY} = \frac{1}{2} \sum_{i \in X} \sum_{j \in Y} J_{ij} \sigma_i^z \sigma_j^z \quad (3.2.15)$$

where $X, Y \in \{A, B, S\}$. As in the previous section we prepare a product initial state of the form

$$\rho = |0\rangle\langle 0|^{|A|-|B|} \otimes |+\rangle\langle +| \quad (3.2.16)$$

with all the spins prepared in the $|0\rangle$ state except those in B . Similar to the previous section we implement the same binary quantum channel by starting the time evolution either with ρ , which transmits a “0”, or starting with $U_A^\dagger \rho U_A$, sending a “1”, where U_A is a unitary supported on A only. The classical information capacity C_t is again bound from below by the probability of detecting a signal p_t , by measuring according to a positive operator valued measure π_B , a signal in B at some time $t > 0$ given the unitary perturbation at A [see (3.1.8)]. Our aim is to study this lower bound p_t as a function of the

channel length, i.e. the distance between A and B .

Just like the previous section we choose $U_A = |1\rangle\langle 0|$ and $\pi_B = |+\rangle\langle +|$. These choices lead us to the exact expression (see Appendix C.3 for details),

$$p_t = \left| \sin \left(2t \sum_{r \in S} J_{rN} \right) \sin (2t J_{1N}) \right|. \quad (3.2.17)$$

for the detection probability. To derive a nonzero lower bound on p_t , we focus our attention on the short time regime, before oscillatory behaviour sets in. In the large system limit, assuming power-law interactions $J_{ij} = |i - j|^{-\alpha}$, the bound takes the form (see appendix C.3 for details)

$$p_t \geq \frac{16t^2}{\pi^2(\alpha - 1)} \frac{1}{(N - 1)^\alpha} \left[1 - \frac{1}{(N - 1)^{\alpha-1}} \right] =: \underline{p}_t \quad (3.2.18)$$

For $\alpha > 1$ the second term in the square bracket is much smaller than 1, and we find

$$\underline{p}_t \sim \frac{16t^2}{\pi^2(\alpha - 1)} \frac{1}{(N - 1)^\alpha} \quad (3.2.19)$$

for the large N asymptotic behaviour of the bound \underline{p}_t . In this context $\delta = N - 1$ is the distance between regions A and B . To determine the shape of the contour line at which \underline{p}_t is equal to some constant ϵ , we set

$$\epsilon = \underline{p}_t \propto \frac{t^2}{\delta^\alpha}. \quad (3.2.20)$$

From the above we can then read off that

$$\delta \propto t^{2/\alpha} \quad (3.2.21)$$

along any of the chosen contour lines. Equation (3.2.21) describes supersonic signal propagation for all $\alpha < 2$, irrespective of the dimension of the underlying lattice. These results can easily be extended to more general initial conditions and to lattices with arbitrary dimension.

3.3 Propagation of correlators

In the following subsections we investigate the spatio-temporal spreading of correlations under the influence of unitary dynamics, starting from a product initial state. The spreading of correlations is most naturally captured using the time dependent connected correlation function,

$$\langle \sigma_j^a \sigma_{j+\delta}^b \rangle_c(t) := \langle \sigma_j^a(t) \sigma_{j+\delta}^b(t) \rangle - \langle \sigma_j^a(t) \rangle \langle \sigma_{j+\delta}^b(t) \rangle \quad (3.3.1)$$

with σ_j^a the $a \in \{x, y, z\}$ Pauli matrix at lattice site j . The norm of these time dependent connected correlation functions can be bounded from above using the now familiar Lieb-Robinson bounds introduced in Section 1.1.3. In the following we compare the shapes of the causal fronts that arise using the time dependent connected correlation functions to the results of the previous sections, as well as to our current understanding of the causal fronts using established Lieb-Robinson bounds.

3.3.1 Exact results for the long-range interacting Ising model

In the previous sections we have established that suitably constructed Hamiltonians can indeed give rise to supersonic propagation and a power law-shaped causal region. In the following we show that such behavior manifests in the long-range interacting Ising and XXZ models. Moreover, we investigate in this context how correlations spread for exponents $\alpha \leq D$ where the Lieb-Robinson bound (1.1.10) of Hastings and Koma [43] is not valid.

Firstly we consider the long-range interacting Ising model (see Chapter 2) defined on a D dimensional lattice Λ ,

$$H_\Lambda = -\frac{1}{2} \sum_{i \neq j} J_{i,j} \sigma_i^z \sigma_j^z, \quad (3.3.2)$$

where, as before, $J_{i,j} \in \mathbb{R}$ denotes the coupling strength in terms of the distance between the lattice sites i and j . Starting from a fully x -polarized initial state with all spins initially pointing along the σ^x direction and using the exact

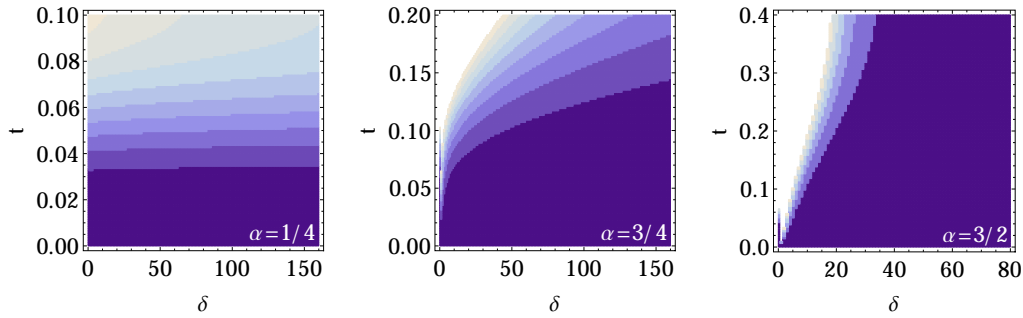


Figure 3.3: Density contour plots of the connected correlator $\langle \sigma_o^x \sigma_\delta^x \rangle_c$ in the (δ, t) -plane for long-range Ising chains with $|\Lambda| = 1001$ sites and three different values of α . Dark colors indicate small values, and initial correlations at $t = 0$ are vanishing.

results from Chapter 2 for the two-spin correlation functions, we can write

$$\langle \sigma_i^x \sigma_j^x \rangle(t) = \frac{1}{2} \langle \sigma_i^x \sigma_j^x \rangle(0) \left[\prod_{k \neq i, j} \cos(2(J_{k,i} - J_{k,j})t) + \prod_{k \neq i, j} \cos(2(J_{k,i} + J_{k,j})t) \right]. \quad (3.3.3)$$

Similar expressions hold for other spin components [see Equations (2.4.2)-(2.4.5)]. We evaluated these expressions for a linear chain of spins ($D = 1$) with interactions $J_{i,j} = J \text{dist}(i, j)^{-\alpha}$. The spreading of correlations is investigated by plotting, in Figure 3.3, the density contours of the connected correlator

$$\langle \sigma_o^x \sigma_\delta^x \rangle_c(t) = \langle \sigma_o^x(t) \sigma_\delta^x(t) \rangle - \langle \sigma_o^x(t) \rangle \langle \sigma_\delta^x(t) \rangle \quad (3.3.4)$$

in the (δ, t) -plane, with $o \in \Lambda$ denoting the centre lattice site.

For $\alpha = 3/2$ (right panel of Figure 3.3) correlations initially seem to spread linearly, but not further than a few tens of lattice sites; plots for other $\alpha > D$ are similar. The breakdown of the initial linear spread in Figure 3.3 (right) is presumably a peculiarity of the long-range Ising model and may be explained by the fact that quasi-particles in a spin-wave approximation are dispersionless for the Hamiltonian (3.3.2) [44].

For $\alpha = 3/4$ (central panel of Figure 3.3) the spreading of correlations shows a distance-dependence that is consistent with a power law-shaped causal region; plots for other $D/2 < \alpha < D$ are similar. These findings nicely match our results on the channel capacity of (3.2.2), namely that, for product initial

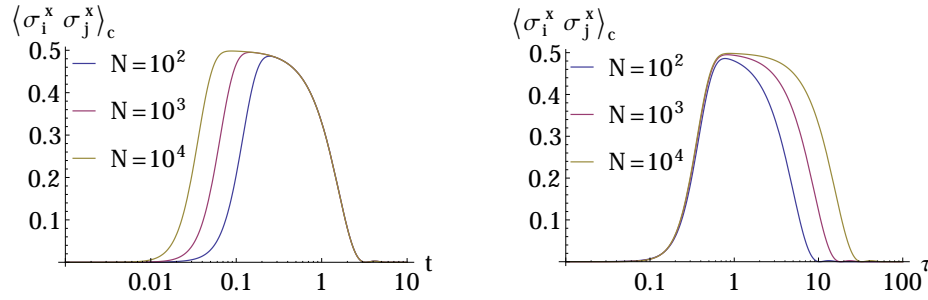


Figure 3.4: Time dependent connected correlation functions $\langle \sigma_i^x \sigma_j^x \rangle_c$ of the long-range Ising model with $\alpha = 1/4$ for lattice sites i and j chosen one site to the left and right of the center of a one dimensional chain consisting of $N = 10^2$ (blue), N^3 (purple) and N^4 (yellow). Left: As a function of time t , the timescale on which correlations build up is strongly N -dependent and even vanished with increasing N . The decay of correlations takes place on a timescale that is independent of N . Right: When plotted as a function of rescaled time $\tau = tN^{1/2-\alpha}$, the timescale on which correlations build up becomes independent of the system size.

states, an effective causal region is present already for $\alpha > D/2$, and not only for $\alpha > D$ as in the more general case of entangled initial states.

For $\alpha = 1/4$ (left panel of Figure 3.3) correlations spread in a broad, more or less distance independent front, and qualitatively similar results are found for all $0 \leq \alpha \leq D/2$. Closer inspection reveals a tiny decrease of correlations with increasing distance δ . In the following we show that this δ -dependence is a finite size effect that disappears in the large system limit.

3.3.1.1 Finite size scaling

Figure 3.4 (left) shows the connected correlation function $\langle \sigma_i^x \sigma_j^x \rangle_c$ as a function of time, we observe that, for exponents $0 \leq \alpha \leq D/2$, the timescale on which correlations build up is strongly system size $N := |\Lambda|$ dependent and vanishes for increasing N . On the other hand the timescale on which correlations decay is independent of the system size. From the upper bound of the two-spin correlation functions [see Equations (2.5.2) and (2.5.3)], the timescale for the build up of correlations scales like $N^{\alpha/D-1/2}$ asymptotically for large N . Hence, plotting $\langle \sigma_i^x \sigma_j^x \rangle_c$ as a function of rescaled time

$$\tau = tN^{1/2-\alpha/D} \quad (3.3.5)$$

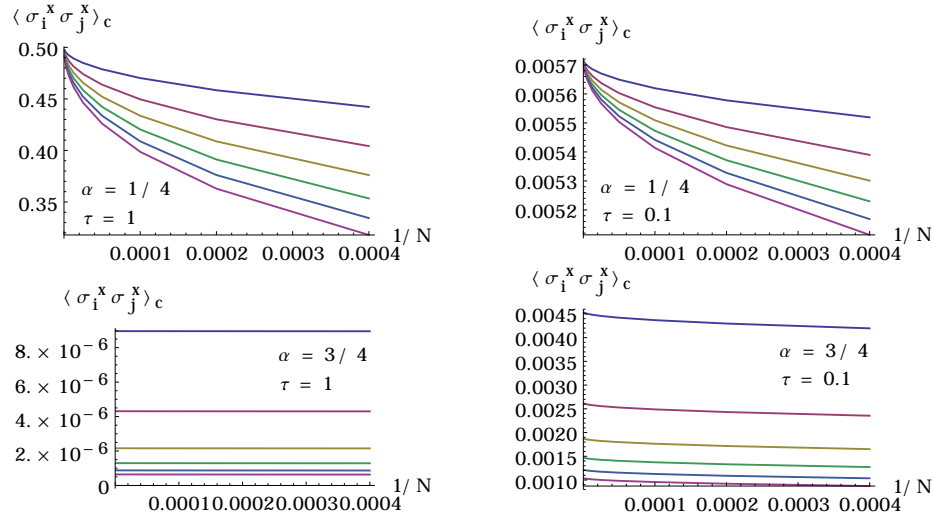


Figure 3.5: Connected correlation functions of the long-range Ising model for fixed values of the rescaled time $\tau = 0.1$ (left panels) and $\tau = 1$ (right panels). In each plot $\langle \sigma_0^x \sigma_\delta^x \rangle_c$ is shown for $\delta = 20, 40, 60, 80, 100$, and 120 (from top to bottom line in graphs) and plotted versus the inverse system size $1/N$. Top panels: For $\alpha = 1/4$ and in the limit $1/N \rightarrow 0$ the connected correlation functions become distance independent implying a flat propagation front. Bottom panels: For $\alpha = 3/4$, the distance dependence does not vanish in the large-system limit.

absorbs the N -dependence of the timescale, where now the timescale on which correlations build up is independent of the system size [see Figure 3.4 (right)].

Only in the rescaled time τ does it make sense to study the large system asymptotic behaviour of the shape of the propagation front. In Figure 3.5 we plot for some fixed instances of τ and various values of δ , the connected correlation function $\langle \sigma_0^x \sigma_\delta^x \rangle_c$ as a function of the inverse system size $1/N$. In the limit $1/N \rightarrow 0$, the connected correlation function converges to a value that is independent of the distance δ , implying a flat, distance independent, propagation front. In Chapter 4 we use a similar rescaling of time to derive a Lieb-Robinson type bound which is valid for any $\alpha > 0$.

This flat propagation front in Figure 3.3 (left) is consistent with the fact that, for small values of α , the Hamiltonian (3.3.2) does not meet the conditions required for the long-range Lieb-Robinson bound (1.1.10) to apply.

3.3.2 Numerical results on the long-range XXZ spin chain

To investigate how the observations of the preceding sections are affected by the presence of dispersion (spin flips), we augment the Ising Hamiltonian (3.3.2) with a non-commuting term. We do this by adding interactions in the transverse direction, leading to the long-range XXZ chain

$$H^{\text{XXZ}} = \sum_{i>j} \frac{1}{|i-j|^\alpha} [2J_\perp (\sigma_i^+ \sigma_j^- + \sigma_i^- \sigma_j^+) + J_z \sigma_i^z \sigma_j^z]. \quad (3.3.6)$$

For short-ranged interactions, this is a standard model used to investigate quantum magnetism. With nearest-neighbour interactions the XXZ -model is, by virtue of the Jordan-Wigner transform (see Section 1.3.1), equivalent to a spinless fermionic model in one dimension. Here, we choose $J_\perp = 1/2$ and $J_z = 1$, so that we are dealing with strong quantum fluctuations. In Figure 3.6 we show numerical results for the time evolution under the XXZ Hamiltonian (3.3.6) with $\alpha = 3/4$, $3/2$, and 3 , starting from the staggered initial state $|\psi_0\rangle = |1, 0, 1, 0, \dots, 1, 0\rangle$ (reminding of the situation of [114]). The plots show results for the equal-time connected correlation functions

$$\langle \sigma_o^z \sigma_\delta^z \rangle_c = \langle \sigma_o^z \sigma_\delta^z \rangle - \langle \sigma_o^z \rangle \langle \sigma_\delta^z \rangle. \quad (3.3.7)$$

For $\alpha = 3/4$ and $3/2$ (left and middle column in Figure 3.6) we observe a coexistence of supersonic and sound-cone-like propagation. For $\alpha = 3$ (right column in Figure 3.6) the spreading of correlations is predominantly linear in the (δ, t) -plane. Figure 3.6 (bottom) recasts the connected correlation functions on a log-log scale, here the linear trends confirm that the causal regions have power-law shapes.

3.4 Comparison with experimental results

The recent theoretical progress made with regard to the spreading of correlations, entanglement and information in long-range interacting quantum lattice models have stimulated efforts by experimentalists to test the exact analytic as well as numeric predictions made in the previous sections and [25, 44].

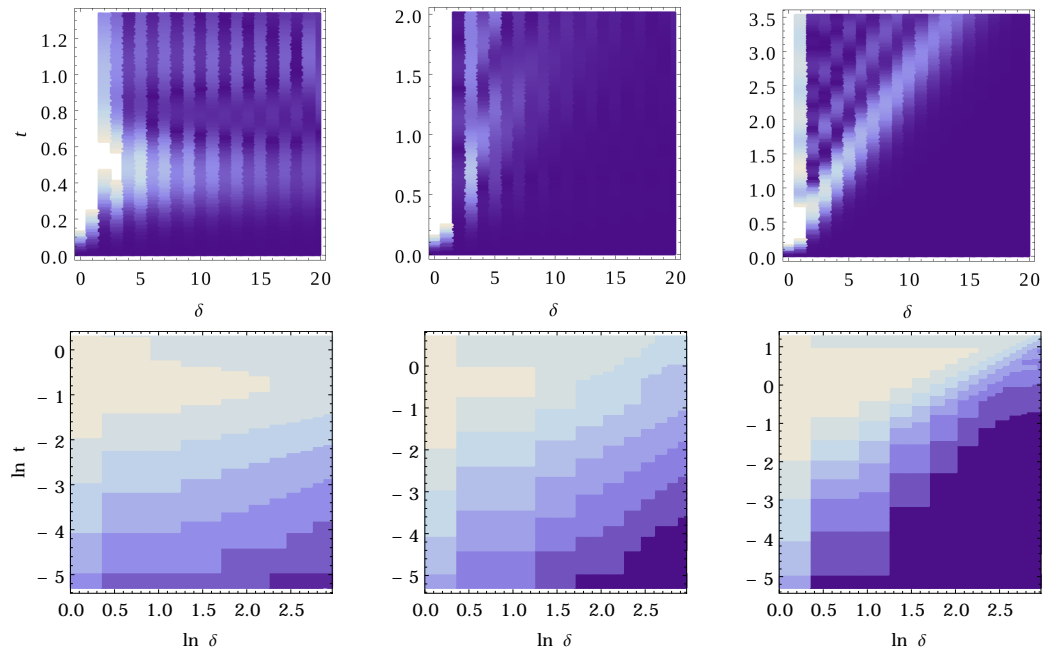


Figure 3.6: (Reproduced from [25]) Top row: Density plots of the connected correlator $\langle \sigma_o^z \sigma_\delta^z \rangle_c$ in the (δ, t) -plane. The results are for long-range XXZ chains with $|\Lambda| = 40$ sites and exponents $\alpha = 3/4, 3/2$, and 3 (from left to right). The left and center plots reveal supersonic spreading of correlations, not bounded by any linear cone, whereas such a cone appears in the right plot for $\alpha = 3$. Bottom row: As above, but showing contour plots of $\ln \langle \sigma_o^z \sigma_\delta^z \rangle_c$ in the $(\ln \delta, \ln t)$ -plane. All plots in the bottom row are consistent with a power law-shaped causal region for larger distances δ .

Of direct relation to the results of this chapter is an experiment performed in the group of Chris Monroe [99]. In [99] the authors report on an experiment that directly measures the shape of the causal region as well as the speed at which correlations propagate within the one-dimensional Ising and XX spin chains. A linear spin-1/2 system, consisting of eleven ions, is encoded into the hyperfine “clock” states of $^{171}\text{Yb}^+$ confined in a Paul trap. The spread of correlations is induced by performing a global quench by initially aligning all eleven spins in the same direction, then suddenly switching the spin-spin couplings on across the entire chain which allows the system to coherently evolve under the Ising or XX -Hamiltonian. The spin-spin interaction matrix they are able to make contains tunable, long-range couplings that fall off as a power-law $J_{i,j} \propto |i - j|^{-\alpha}$ with i and j lattice sites and $|\cdot|$ the Euclidean distance. After quenching to the long-range Ising or XX -model with a specific α , they evolve the system coherently for different lengths of time before resolving the spin

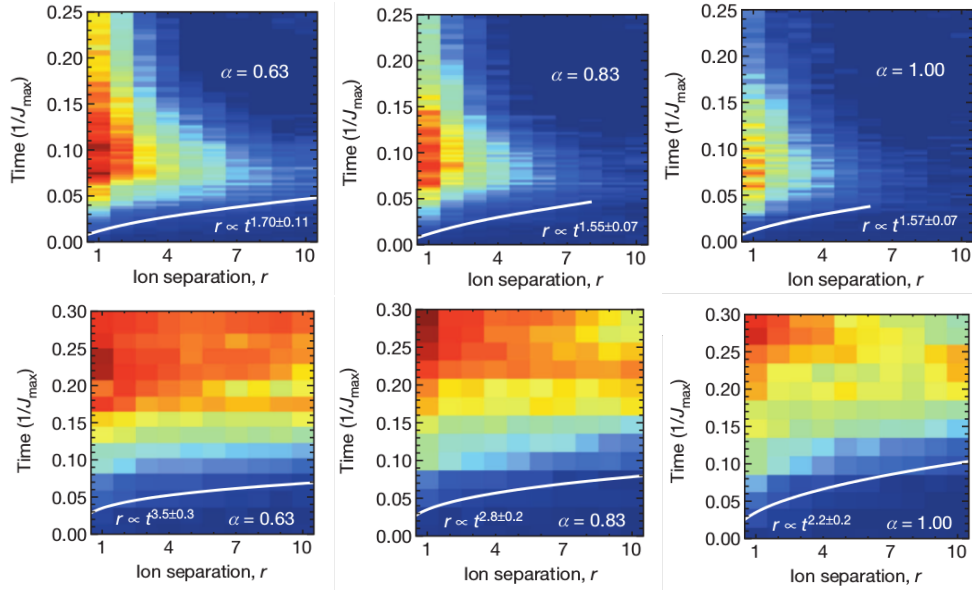


Figure 3.7: Experimental results from Richerme et al. [99] showing the connected correlation function $\langle \sigma_j^x \sigma_{j+r}^x \rangle_c(t)$ after a global quench of a linear chain consisting of 11 ions for three different values of α as indicated. The top panel shows the results for a long-range power-law interacting Ising model. The bottom panel shows the same results for the long-range interacting XX -model. Throughout the solid white curves represent the power-law shaped causal fronts as found in the experiments.

state of each ion using a CCD camera. To see the buildup of correlations they measure single- and two-spin correlation functions to construct the connected correlation function $\langle \sigma_i^x \sigma_j^x \rangle_c(t)$ between any pair of ions at any time t . This is exactly the situation described in Section 3.3, and gives us the unique opportunity to directly compare the forms of the theoretical causal fronts of the long-range Ising model with those of experiments.

The top panel of Figure 3.7 shows the experimental results of the connected correlation function of the long-range interacting Ising model for $\alpha = 0.63$ (left), 0.83 (centre) and 1.00 (right). For all three values of α they presented we see a power-law causal front as indicated by the white curves superimposed onto the images. Some argue that claiming the form of the causal front is a power-law is premature since the existence of a power-law cannot be claimed for a system consisting of only eleven ions. Nonetheless, these curves agree well with Figure 3.3 (centre) showing the connected correlation function for $\alpha = 3/4$, but qualitatively similar behaviour is expected for all $1/2 < \alpha < 1$.

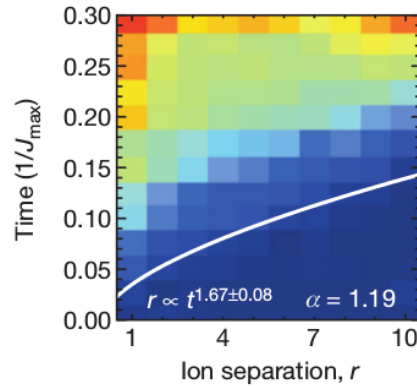


Figure 3.8: Experimental results of [99] showing supersonic spreading of correlations for $\alpha = 1.19 > 1$ as captured by the connected correlation function $\langle \sigma_j^x \sigma_{j+r}^x \rangle_c(t)$ after a global quench in the long-range Ising model on a one dimensional chain consisting of 11 ions.

The bottom panel of Figure 3.7 shows the experimental connected correlations function of the long-range XX -model for the same three α -values. For all values of α shown the propagation front has a power-law form. Time dependent density matrix renormalization results for the spreading of correlations, in the more general XXZ model, can be seen in Figure 3.6 (top). This, more general case also shows a power-law shaped causal front that can be read off from the log-log plot in Figure 3.6 (bottom left).

Figure 3.8 shows the first experimental results showing supersonic, faster than linear, spreading of correlations as captured by the connected correlation function for α greater than the dimension of the underlying lattice. This agrees well with the results of Sections 3.2.1 and 3.2.2, where we expect to see faster than linear spreading of correlations for all $\alpha < 2$.

Another experiment, closely related to the theoretical predictions made in this thesis, was performed in the group of Christiaan Roos [56]. In [56] the authors investigate the spreading of correlations in the long-range transverse field Ising model

$$H = \frac{1}{2} \sum_{(i,j) \in \Lambda \times \Lambda} J_{ij} \sigma_i^x \sigma_j^x + B \sum_{i \in \Lambda} \sigma_i^z, \quad J_{ij} \propto |i - j|^{-\alpha} \quad (3.4.1)$$

emanating from local quenches. These quenches are performed by flipping one or more spins which populate a range of quasiparticle modes. Each of these

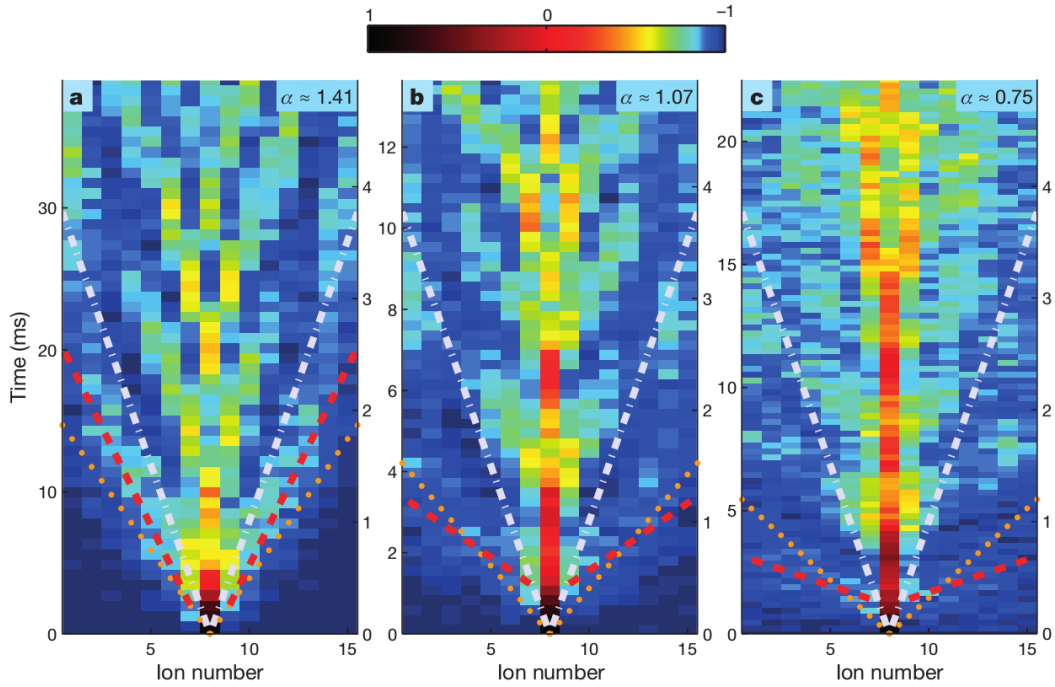


Figure 3.9: (Reproduced from [56]) Measured magnetization following a local quench. From left to right the interaction ranges are $\alpha \approx 1.41$, 1.07 , 0.75 . In the left image an effective light cone is evident and the dynamics are approximately described by nearest neighbour interactions only. Red lines are fits to the measured magnon arrival times, white lines represent the average nearest neighbour interactions and the orange dotted line shows the light cone after renormalization by the algebraic tail. As the interaction range increases the light-cone disappears and the nearest neighbour model fails to predict the dynamics.

modes can be seen as an equal superposition of spin waves (magnons) with positive and negative momentum. Figure 3.9 shows the magnetization $\langle \sigma_j^z \rangle$ following a local quench at the central spin for $\alpha = 1.41$ (left), 1.07 (centre) and 0.75 (right). As α decreases, i.e. the range of interaction becomes longer, (left to right in Figure 3.9) the magnon arrival times become shorter. For $\alpha = 1.41$ [Figure 3.9 (left)] the magnon arrival times are closely related to the nearest neighbour ($\alpha = \infty$) light-cone, but as expected, still propagate faster than it. This discrepancy between the nearest neighbour light-cone and the measured magnon arrival times become more pronounced for decreasing α . Unfortunately the authors have not made any estimates about the form of the observed causal fronts. However, given that they consider a local quench in a one-dimensional lattice, we expect from Section 3.2.2 that the spreading of information should be faster than linear for all $\alpha < 2$.

3.5 Summary and conclusions

In this chapter we have studied the spreading of correlations, information and entanglement in quantum lattice systems with long-range interactions decaying as a power-law in separation distance $J_{i,j} \propto |i - j|^{-\alpha}$. When α is greater than the dimension D of the underlying lattice Λ a causal region can be identified. This causal region is not necessarily cone-shaped and can be supersonic, faster than linear. Specifically, the long-range interacting toy model (3.2.2) showed faster than linear spreading of information for all $D < \alpha < D+1$. On the other hand, the long-range interacting Ising model with a measurement on a finite subset of the lattice, showed supersonic spreading for $\alpha < 2$ in any dimension. All the models we considered showed a power-law shaped causal region. This means that effects exceed some $\epsilon > 0$ for $v|t| > \epsilon\delta^q$ with $c, q > 0$.

We constructed models, together with entangled initial states, such that the spreading of information is not restricted to any causal region, giving rise to a breakdown of causality. Studying the same models, but with product initial states, we find a well-defined causal region for all $\alpha > D/2$. These results are validated by comparing with analytical results for the long-range Ising model as well as numerical results for the long-range XXZ -model. Based on the evidence of this chapter we conjecture that a causal region already exists for product initial states with $\alpha > D/2$.

Lastly we compared the exact and numerical results of this chapter with current ion trap experiments. At the moment experimentalists are only able to study the spatio-temporal spreading of correlations, unitarily evolving under the long-range Ising and XX -Hamiltonians, for relatively small system sizes consisting of a couple of tens of ions. Improvements in the number of ions that can be trapped and manipulated will greatly improve our current understanding of the many body dynamics of quantum systems with long-range interactions. In order to *believe* the results of these large quantum simulators we have to benchmark these experimental results with exact analytics or numerics. For this reason the results of this chapter are extremely significant for future developments of quantum simulators and eventually full-blown quantum computers.

Chapter 4

Interplay of soundcone and supersonic dynamics

In this chapter we study the spatio-temporal propagation of various physical quantities. As noted in Chapter 3, this is a topic where long-range interactions lead to peculiar behavior. A number of papers devoted to this topic have appeared in the past two years, reporting results on the spreading of correlations, information, or entanglement in long-range interacting quantum systems [25, 44, 46, 104, 47, 34, 95].

The majority of our understanding of the spreading of correlations in long-range systems comes from analytical or numerical studies of model systems, where for example correlations or entanglement between lattice sites i and j are calculated as functions of time t and spatial separation $\text{dist}(i, j)$. Typical examples of such results, similar to some of those in [25, 44, 46, 104, 47, 34, 95], are shown in Figure 4.1 for a number of different models, physical quantities, and exponents α . For larger α (Figure 4.1 right), the behavior is similar to the short-range case, with only small effects outside a cone-shaped region. For small α (Figure 4.1 left), correlations propagate supersonically, i.e. faster than any finite group velocity would permit, and are mostly confined to a region with power law-shaped boundaries. For intermediate α (Figure 4.1 center), a crossover from cone-like to faster-than-cone behavior is observed. While these three regimes seem to be typical and occur in many of the models studied, notable exceptions (some of which will be discussed further below) do occur and lead to a more complicated overall picture.

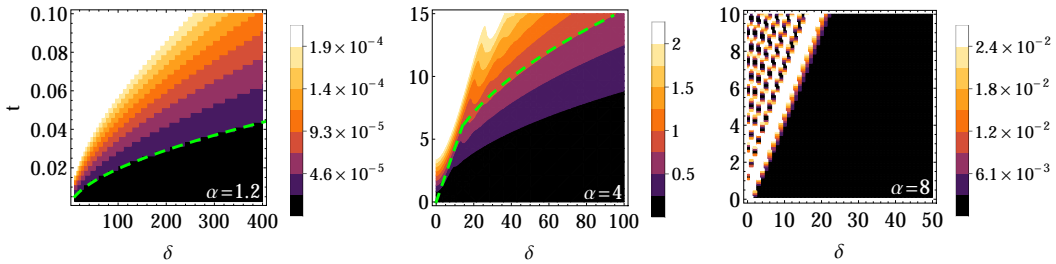


Figure 4.1: Propagation patterns as a function of distance $\delta = \text{dist}(i, j)$ and time t for different long-range exponents α . To highlight the generality of the phenomena we discuss in this chapter, we use different models and physical quantities as examples. In all plots, lighter colors represent larger values (the absolute scale is not relevant here). Left: For a long-range Ising chain with $\alpha = 1.2$, we show the probability to detect a signal sent through a quantum channel from site 0 to δ [25]. The green line is a guide to the eye and shows a power law $\delta \propto t^{1.7}$. This same power law is found in Figure 3.8. Center: Connected equal-time correlations between lattice sites 0 and δ in a long-range field theory in one spatial dimension with $\alpha = 4$ [95]. After an initial cone-like spreading, a cross-over to power law-shaped contours is observed. The green dashed curve is a guide to the eye. Right: The spreading of entanglement as captured by the mutual information between two lattice sites separated by a distance δ in the long-range hopping model (4.3.1) with $\alpha = 8$, starting from a staggered initial state. Entanglement is sharply confined to the interior of a cone.

In this chapter we prove general bounds, supplemented with model calculations, that help to establish a comprehensive and consistent picture of the various kinds of propagation behavior that occur in long-range interacting lattice models. In Section 4.1 Lieb-Robinson-type bounds are extended to strong long-range interactions where $\alpha < D$. For intermediate exponents α , we advocate, in Section 4.2, the use of a Lieb-Robinson-type bound in the form of a matrix exponential, which is tight enough to capture the transition from a cone-like to a faster-than-cone propagation as in Figure 4.1 (center), and is also computationally efficient. In Section 4.3 these results are complemented by model calculations showing that, even in the regime $\alpha < D$ of strong long-range interactions, cone-like propagation may be a dominant feature.

Note: Sections 4.1 and 4.2 formed part of a project done by David Storch under the supervision of Michael Kastner. These works together with the remaining sections were published in [109]. Section 4.3 reflects the author's main contribution to this publication.

4.1 Lieb-Robinson bounds for $\alpha < D$

An understanding of the timescales of the dynamics turns out to be crucial in deriving analytical results in the $\alpha < D$ regime. The presence of strong long-range interactions is known in many cases to cause a scaling of the relevant timescales with system size [3, 59, 60, 6, 116, 37]. For long-range quantum lattice models the fastest timescale $\tau_1 \propto N^{-q}$ [see Sections 2.6 and 3.3.1.1] was found to shrink like a power law with increasing system size N , where q is a positive exponent [6, 116]. As an example, the system size scaling of the timescale on which correlations build up in the long-range interacting Ising model can be seen in Figure 3.4. The specific form of the power-law scaling can be read off from Equations (2.5.2)-(2.5.3) for the long-range interacting Ising model. This speed-up of the relevant timescales makes clear why previous attempts to derive a Lieb-Robinson-type bound for $\alpha < D$ failed: in the large- N limit the dynamics becomes increasingly faster, and hence propagation is not bounded by any finite quantity. Considering evolution in rescaled time $\tau = tN^q$ can resolve this problem and allows us to obtain a finite bound in the thermodynamic limit.

Suppose we have an arbitrary D -dimensional lattice Λ with N sites. The full dynamics takes place on the tensor product Hilbert space

$$\mathcal{H} = \bigotimes_{i=1}^N \mathcal{H}_i \quad (4.1.1)$$

with finite-dimensional local Hilbert spaces \mathcal{H}_i . On \mathcal{H} a generic Hamiltonian

$$H = \sum_{X \subset \Lambda} h_X \quad (4.1.2)$$

with n -body interactions is defined, with local Hamiltonian terms h_X compactly supported on the finite subsets $X \subset \Lambda$. The Hamiltonian is required to satisfy the following two conditions:

1. *Boundedness*,

$$\sum_{X \ni i, j} \|h_X\| \leq \frac{\lambda}{[1 + \text{dist}(i, j)]^\alpha} \quad (4.1.3)$$

with a finite constant $\lambda > 0$. This condition, also used in [43], is a generalization of the definition of power law-decaying interactions, and reduces to the usual definition in the case of pair interactions, i.e., when X consists only of the two elements i and j .

2. *Reproducibility,*

$$\mathcal{N}_\Lambda \sum_{k \in \Lambda} \frac{1}{[1 + \text{dist}(i, k)]^\alpha [1 + \text{dist}(k, j)]^\alpha} \leq \frac{p}{[1 + \text{dist}(i, j)]^\alpha} \quad (4.1.4)$$

for finite $p > 0$, with

$$\mathcal{N}_\Lambda = 1 / \sup_{i \in \Lambda} \sum_{j \in \Lambda \setminus \{i\}} \frac{1}{[1 + \text{dist}(i, j)]^\alpha}. \quad (4.1.5)$$

The lattice-dependent factor \mathcal{N}_Λ is the same that is frequently used to make a long-range Hamiltonian extensive [17, 59] [see also Equation (2.1.6)], but we use it here for a different purpose. Asymptotically for large regular lattices, one finds [59]

$$\mathcal{N}_\Lambda \sim \begin{cases} c_1 N^{\alpha/D-1} & \text{for } 0 \leq \alpha < D, \\ c_2 / \ln N & \text{for } \alpha = D, \\ c_3 & \text{for } \alpha > D, \end{cases} \quad (4.1.6)$$

with α -dependent positive constants c_1 , c_2 , and c_3 . Equation (4.1.4) is a modified version of one of the requirements for the proof in [43], but due to the modification by the factor \mathcal{N}_Λ the condition is satisfied for a larger class of models, including regular D -dimensional lattice with power law-decaying interactions with arbitrary positive exponents α [80]. In the above described setting the Lieb-Robinson-type bound takes the form

$$\|[O_A(\tau \mathcal{N}_\Lambda), O_B(0)]\| \leq C \|O_A\| \|O_B\| \frac{|A||B|(e^{v|\tau|} - 1)}{[\text{dist}(A, B) + 1]^\alpha} \quad (4.1.7)$$

in rescaled time

$$\tau = t / \mathcal{N}_\Lambda. \quad (4.1.8)$$

For details see the appendices in [109]. This bound has exactly the same form as the original bound of Hastings and Koma [43], except that time t has been replaced by rescaled time τ on the right hand side of Equation (4.1.7). The

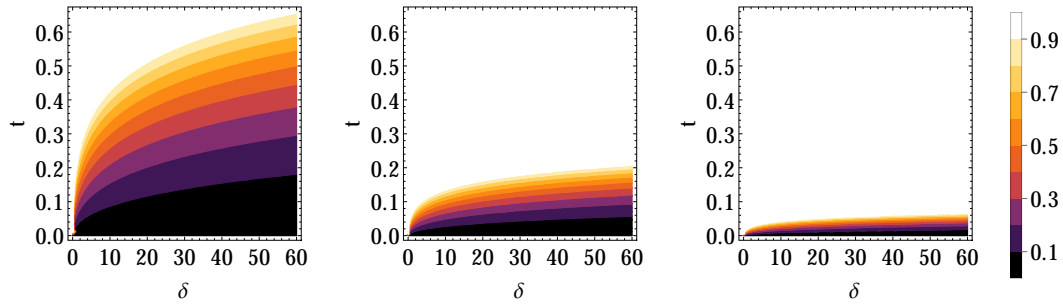


Figure 4.2: Bound (4.1.7) in physical (not rescaled) time t for $\alpha = 1/2$ and lattice sizes $N = 10^1, 10^2, \text{ and } 10^3$ (from left to right), illustrating the speed-up of the propagation with increasing lattice size.

rescaled time bound reproduces qualitative features of supersonic propagation [see Figure 4.1 (left)]. As before, the shape of the causal region can be determined by finding those values of τ and $\text{dist}(A, B)$ such that the fraction on the right hand side of Equation (4.1.7) is greater than some positive ϵ . Recast in terms of physical time t , the causal region is determined by

$$v|t| \geq \mathcal{N}_\Lambda \ln [\epsilon(\text{dist}(A, B) + 1)^\alpha + 1]. \quad (4.1.9)$$

From (4.1.6) we notice that when $\alpha < D$ the right hand side of (4.1.9) decreases in the system size. This signals a speed-up in physical time t for increasing system size and is illustrated in Figure 4.2.

4.2 Matrix exponential bounds for intermediate α

For long-range models with intermediate exponents, in the range $3 < \alpha < 6$ or even a bit larger, one observes a transition from cone-like and supersonic propagation (see Figure 4.1 center). This is the most relevant regime for experimental realizations of long-range interactions by means of cold atoms or molecules, but a theoretical description of the shape of the propagation front turns out to be challenging. In the following present a Lieb-Robinson-type bound that manages to capture the features of the propagation front as observed in long-range models with intermediate exponents, showing a clear and sharp transition from cone-like to supersonic propagation.

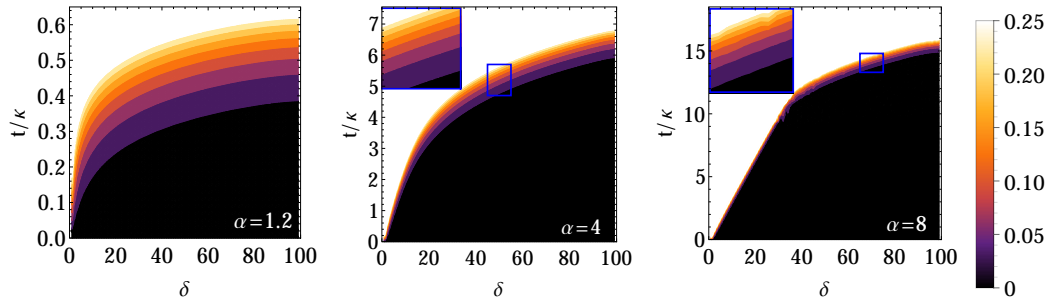


Figure 4.3: Spacetime plots of the matrix exponential bound (4.2.2) for several values of α in a one dimensional system with $L = 201$ lattice sites and periodic boundary conditions. Left: For $\alpha = 1.2$ the bound shows a propagation front with a shape similar to the one of the Ising model in Figure 4.1 (left). Center: For intermediate $\alpha = 4$ a transition from soundcone to supersonic dynamics is being heralded. Right: The two regimes of soundcone-like and supersonic dynamics are fully exposed for $\alpha = 8$.

As in Section 4.1, our setting is a D -dimensional lattice Λ consisting of N sites together with a tensor product Hilbert space (4.1.1) composed of finite-dimensional local Hilbert spaces. We consider a generic Hamiltonian with pair interactions,

$$H = \sum_{k < l}^N h_{kl}, \quad (4.2.1)$$

where the pair interactions h_{kl} are bounded operators supported on lattice sites k and l only. For observables we consider bounded operators O_A and O_B that are supported on single sites $A = \{i\}$ and $B = \{j\}$. In this setting, we prove in [109] a bound in the form of an $N \times N$ matrix exponential,

$$\|[O_i(t), O_j(0)]\| \leq 2\|O_A\|\|O_B\| \left(\exp[2\kappa J|t|]_{i,j} - \delta_{i,j} \right), \quad (4.2.2)$$

where J is the interaction matrix with elements

$$J_{k,l} = \|h_{kl}\| \quad (4.2.3)$$

and $\kappa = \sum_k J_{i,k}$. In one spatial dimension the interaction matrix J is of Toeplitz type and thus (4.2.2) can be evaluated in $\mathcal{O}(N^2)$ time using the Levinson algorithm [8]. For translationally invariant one-dimensional systems, J is a circulant matrix, which permits an analytical solution of (4.2.2) by means of Fourier transformation.

The bound (4.2.2) is tighter than the bounds in [43, 85, 38], and the crossover from cone-like to supersonic propagation is nicely captured (see Figure 4.3). Due to its form as a matrix exponential, the bound is less explicit than others in the sense that asymptotic properties and functional forms of causal fronts are not easily read off. But since the calculation of a matrix exponential scales polynomially in the matrix dimension N (like $\mathcal{O}(N^3)$ or even faster [83]) the bound can easily be evaluated for large lattices up to $\mathcal{O}(10^4)$ on a desktop computer. This is orders of magnitude larger than the sizes that can be treated by exact diagonalization, and covers the system sizes that can be reached for example with state-of-the-art ion trap based quantum simulators of spin systems [13]. Different from other bounds of Lieb-Robinson-type, the matrix exponential bound (4.2.2) can be computed for the exact type of interaction matrix realized in a specific experimental setup. This improves the sharpness of the bound, and can make it a useful tool for investigating all kinds of propagation phenomena in lattice models of intermediate system size.

4.3 Long-range hopping for small α

The bounds discussed in Sections 4.1 and 4.2 are valid for arbitrary initial states, and therefore it may well happen that propagation for a given model and some, or even most, initial states is significantly slower than what the bound suggests. Indeed, linear (cone-like) propagation was observed in model calculations even for moderately large exponents like $\alpha = 3$ [46, 44, 104, 25, 47]. But, as we show in the following, such cone-like propagation can, for suitably chosen initial states, even persist into the strongly long-range regime $0 < \alpha < D$. In the following subsections we analyze free fermions on a one-dimensional lattice with long-range hopping. This is arguably the simplest model to illustrate cone-like propagation in long-range models. We explain the observations on the basis of dispersion relations and density of states. While strictly speaking such a long-range hopping model does not meet the conditions under which Lieb-Robinson bounds have been proved, it proves helpful for understanding the conditions under which cone-like propagation may or may not be observed in other long-range interacting models.

4.3.1 Long-range hopping model

Consider a free fermionic hopping model in one dimension with periodic boundary conditions,

$$H = -\frac{1}{2} \sum_{j=1}^N \sum_{l=1}^{N-1} d_l^{-\alpha} \left(c_j^\dagger c_{j+l} + c_{j+l}^\dagger c_j \right), \quad (4.3.1)$$

where c_j^\dagger , c_j are fermionic creation and annihilation operators at site j . We choose long-range hopping rates proportional to $d_l^{-\alpha}$, where

$$d_l = \begin{cases} l & \text{if } l \leq N/2, \\ N-l & \text{if } l > N/2, \end{cases} \quad (4.3.2)$$

is the shortest distance between two sites on a chain with periodic boundary conditions. A Fourier transformation brings the Hamiltonian (4.3.1) into diagonal form

$$H = \sum_k \epsilon(k) a_k^\dagger a_k \quad (4.3.3)$$

with

$$c_j = \frac{1}{\sqrt{N}} \sum_k e^{ikj} a_k. \quad (4.3.4)$$

and dispersion relation

$$\epsilon(k) = - \sum_{l=1}^{N-1} \frac{\cos(kl)}{d_l^\alpha}, \quad (4.3.5)$$

where $k = 2\pi m/N$ with $m = 1, \dots, N$. Notice that we use a_k^\dagger and a_k for momentum space creation and annihilation operators while c_j^\dagger and c_j are reserved for real space.

4.3.2 Propagation from staggered initial state

We choose a staggered initial state $|1010\dots\rangle$ in position space, i.e., initially every odd site is occupied. For simplicity of notation we assume the number N of lattice sites to be even. A straightforward calculation, similar to that in [28], yields

$$\langle n_j(t) \rangle = \frac{1}{2} - \frac{(-1)^j}{2N} \sum_{n=1}^N \cos [t\Delta(k)] \quad (4.3.6)$$

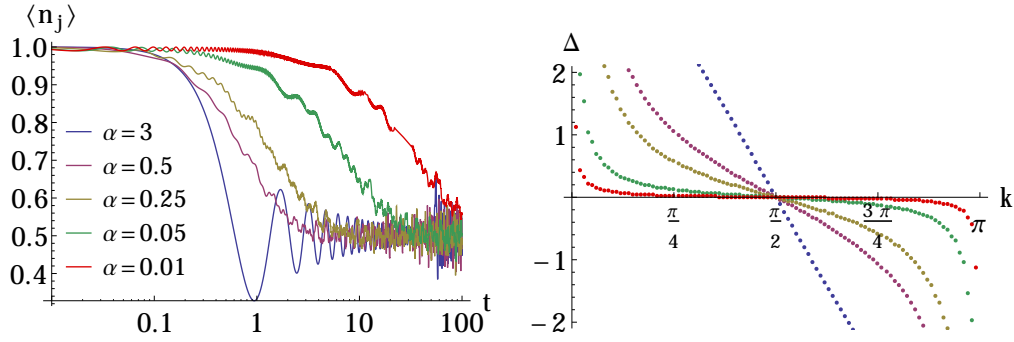


Figure 4.4: Left: Time dependence of the occupation number of site j for different α , starting from a staggered initial state. Right: Δ as a function of k . The system size is $N = 200$ in both plots.

for the time-dependence of the occupation number at lattice site j , where

$$\Delta(k) := \epsilon(k + \pi) - \epsilon(k) = 2 \sum_{l=1}^{N/2} \frac{\cos[k(2l-1)]}{d_{2l-1}^\alpha} \quad (4.3.7)$$

and $k = 2\pi m/N$ with $m = 1, \dots, N$. In Figure 4.4 (left) the time evolution of the occupation number $\langle n_j(t) \rangle$ is plotted for different values of α . We observe that the time it takes to relax to the equilibrium value of $1/2$ increases dramatically for small α (note the logarithmic timescale). This may seem counterintuitive, as a longer hopping range may naively be expected to lead to faster propagation or equilibration. The effect can be understood from Figure 4.4 (right), showing the spectrum of the frequencies Δ in the cosine terms of Equation (4.3.6). As α decreases, the majority of these frequencies lie within a small window around zero, implying very slow dephasing of the cosine terms.

A more refined picture of the propagation behavior can be obtained by studying the spreading of correlations. Starting again from a staggered initial state, a straightforward calculation similar to that in [20, 28], and similar to the one leading to (4.3.6), yields

$$\langle c_{j+\delta}^\dagger(t) c_j(t) \rangle = \frac{1}{2} \delta_{\delta,0} - \frac{(-1)^{j+\delta}}{2N} \sum_k e^{it[\epsilon(k+\pi) - \epsilon(k)]} e^{-ik\delta}. \quad (4.3.8)$$

Figure 4.5 shows contour plots in the (δ, t) -plane of the absolute values of the correlations (4.3.8) for different values of α . For all α shown, a cone-

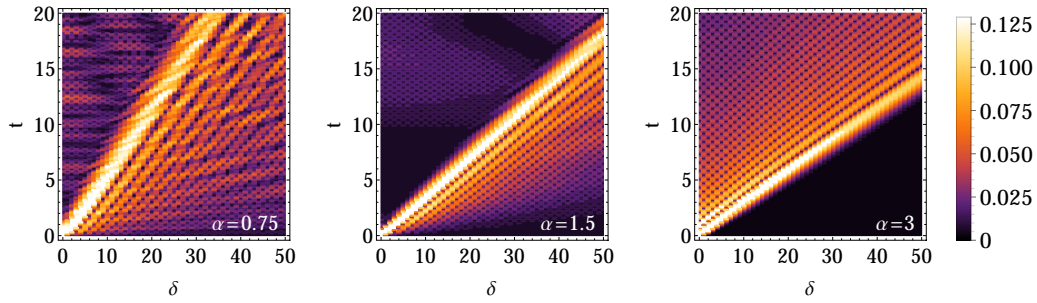


Figure 4.5: Contour plots in the (δ, t) -plane, showing correlations (4.3.8) between sites 0 and δ in the fermionic long-range hopping model for $N = 200$ lattice sites and various values of α , starting from a staggered initial state.

like propagation front is clearly visible, even in the case of $\alpha = 3/4 < D$. Two properties of the cone can be observed to change upon variation of the exponent α :

1. The boundary of the cone is rather sharp for larger α (like $\alpha = 3$), whereas correlations “leak” into the exterior of the cone for smaller α (like $\alpha = 3/2$ and $\alpha = 3/4$).
2. The velocity of propagation, corresponding to the inverse slope of the cone, decreases with decreasing α [see Figure 4.7 (left)]. This confirms the counterintuitive observations of Figure 4.4 (left) that correlations seem to spread slower for small α .

We will argue in Section 4.3.4 that some of these features can be understood on the basis of the dispersion relation (4.3.5) and the density of states of the long-range hopping model.

4.3.3 Dispersion and group velocity

In the limit of large system size the dispersion relation takes the form

$$\epsilon(k) = - [\text{Li}_\alpha(e^{ik}) + \text{Li}_\alpha(e^{-ik})] \quad (4.3.9)$$

where Li_α is the polylogarithm [89]. This function is plotted in Figure 4.6 (left) for different values of α . For $\alpha = 3$ the dispersion ϵ is a smooth function

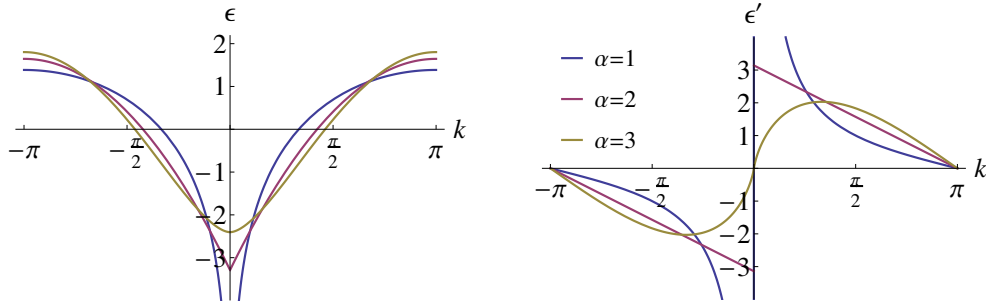


Figure 4.6: Dispersion relation (4.3.9) (left) and its derivative $\epsilon'(k)$ (right) for the long-range fermionic hopping model (4.3.1) with exponents $\alpha = 1, 2,$ and 3 .

of k , while it shows a cusp at $k = 0$ for $\alpha = 2$, and a divergence at $k = 0$ for $\alpha = 1$. Correspondingly, the derivative $\epsilon'(k)$ as shown in Figure 4.6 (right) is discontinuous at $k = 0$ for $\alpha = 2$, and diverges at $k = 0$ for $\alpha = 1$. More generally we can analyze ϵ' in the vicinity of $k = 0$ by considering the difference quotient between the zeroth and the first mode,

$$\left| \frac{\epsilon(2\pi/N) - \epsilon(0)}{2\pi(1-0)/N} \right| = \frac{N}{2\pi} \sum_{l=1}^{N-1} \frac{|\cos(2\pi l/N) - 1|}{d_l^\alpha} \quad (4.3.10)$$

$$\geq \frac{N}{2\pi} \sum_{l=1}^{N-1} \frac{(2\pi l/N)^2}{d_l^\alpha} = \frac{4\pi}{N} \sum_{l=1}^{N/2} l^{2-\alpha}. \quad (4.3.11)$$

In the large- N limit we approximate the sum by an integral,

$$\frac{4\pi}{N} \int_1^{N/2} l^{2-\alpha} dl = \frac{2\pi}{N(3-\alpha)} [(N/2)^{3-\alpha} - 1] \sim N^{2-\alpha}. \quad (4.3.12)$$

This implies that, for $\alpha < 2$, the derivative ϵ' diverges at $k = 0$ in the limit of infinite system size. Interpreting $\epsilon'(0)$ as a group velocity, we infer that we have a finite group velocity only for $\alpha > 2$, whereas the concept of a group velocity breaks down for $\alpha < 2$. The same conclusions about dispersion relations and group velocities also hold for long-range interacting XX and XXZ spin models when restricting the dynamics to the single magnon sector, as the dispersion relations of these models are essentially identical to (4.3.5). The breakdown of the concept of a maximum group velocity can help us to understand Figure 4.5. For $\alpha > 2$ a finite group velocity restricts the propagation to the interior of a cone, which makes this cone appear rather sharp. For $\alpha < 2$, although a cone

is still visible, larger (and, in fact, arbitrarily large) propagation velocities may occur and are responsible for the “leaking” of correlations outside the cone.

The threshold value $\alpha = 2$ for supersonic propagation (i.e., propagation not bounded by any finite group velocity) was also found in Section 3.2.2 by using quantum channels together with single site resolved measurements. It was proved in Section 3.2.1 (see also [25]) that information can be transferred supersonically through a quantum channel with finite dimensional local Hilbert space for any $\alpha < D + 1$, while no such proof exists for $\alpha > D + 1$. However, this result requires the measuring of observables supported on semi-infinite sub-lattices, which is not the most physical scenario. For models with infinite dimensional local Hilbert spaces \mathcal{H}_i , supersonic propagation can occur also in models with nearest-neighbor interactions, although this appears to happen only under rather specific circumstances [23].

4.3.4 Density of states and typical propagation velocities

From Figure 4.5 and the discussion in Section 4.3.3 we have seen that, while supersonic propagation can occur for $\alpha < 2$, cone-like propagation is observed for these values of α at least for some initial states. In this section we will argue that the qualitative features of the observed behavior can be understood on the basis of the density of states

$$\rho(v) = \frac{1}{2\pi} \int_0^{2\pi} \delta\left(v - \frac{d\epsilon}{dk}\right) dk \quad (4.3.13)$$

in the large system limit. Equation (4.3.13) can be rewritten as

$$\rho(v) = \frac{1}{2\pi} \sum_{k_0} \int_0^{2\pi} \delta(k - k_0) \left| \frac{d^2}{dk^2} \epsilon(k_0) \right|^{-1} dk \quad (4.3.14)$$

where the sum is taken over all roots k_0 of the argument of the delta function. The polylogarithms that appear in the dispersion relation (4.3.9) can be

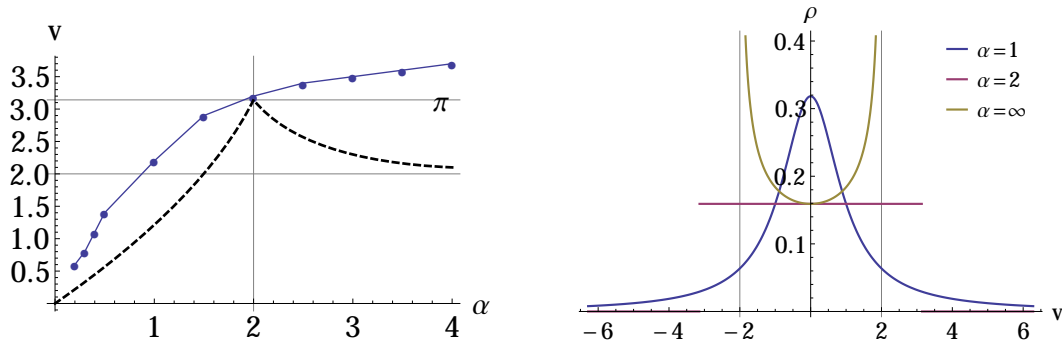


Figure 4.7: Left: The blue curve shows the dominant velocity of propagation, as read off from the inverse slope of the bright cones in Figure 4.5, plotted as a function of the exponent α . The black dashed curve shows the preferred velocity (largest probability) of a general state in the large system limit. As α decreases the preferred velocity increases to $v = \pi$ at $\alpha = 2$. Below $\alpha = 2$ the preferred velocity decreases to zero. Right: Density of states (4.3.13) for $\alpha = 1, 2$ and ∞ .

analytically evaluated for certain integer values of α , yielding

$$\rho(v) = \frac{1}{\pi} \begin{cases} \frac{1}{1+v^2} & \text{for } \alpha = 1, \\ \frac{1}{2} \Theta(\pi - v) \Theta(\pi + v) & \text{for } \alpha = 2, \\ \frac{1}{\sqrt{4-v^2}} & \text{for } \alpha \rightarrow \infty, \end{cases} \quad (4.3.15)$$

where Θ is the Heaviside step function. For those three values of α , the density of states is plotted in Figure 4.7 (right), but other cases can be evaluated numerically (not shown in the figure). Again, as for the group velocity in Figure (4.6) and the classical information capacity in Section 3.2.2, we find a threshold value of $\alpha = 2$, as explained in the following.

For $\alpha < 2$, the density of states ρ is nonzero for all v , implying that propagation is not bounded by any finite maximum velocity. The maximum of ρ , however, is at $v = 0$ for all $\alpha < 2$, and this gives an indication that slow propagation with a small velocity is favored, although larger velocities do occur [as in Figure 4.5 (left and center)]. The maximum at $v = 0$ becomes more sharply peaked when α approached zero, explaining the vanishing of the inverse slope of the cone in Figure 4.5 in that limit, as shown in Figure 4.7 (left).

For $\alpha \geq 2$, the density of states ρ is nonzero only on a finite interval $[-v_{\max}, +v_{\max}]$, where v_{\max} depends on α . For $\alpha > 2$ the density of states diverges, and therefore takes on its maximum, at $\pm v_{\max}$. This implies that the maximum velocity is favored, although smaller velocities also occur [as in Figure 4.5 (right)]. This serves as an additional explanation of the sharp boundary in the spreading for large values of α (see Figure 4.5).

As α decreases from infinity (i.e. nearest neighbour hopping) the density of states [see Figure 4.7 (right)] diverges at increasing maximum velocities v_{\max} . The increase in v_{\max} continues until $\alpha = 2$ where it reaches a maximum of π . Decreasing α beyond 2 causes the majority of excitations to prefer smaller velocities peaked around $v = 0$. This behaviour is superimposed on Figure 4.7 (left) which shows the dominant velocity of propagation, as read off from the inverse slope of the bright cones in Figure 4.5, plotted as a function of the exponent α . The discrepancies are probably due to the finite size effects and the fact that the staggered initial state is not a very general state.

4.4 Summary and conclusions

In this chapter we have studied, from several different perspectives, the nonequilibrium dynamics of lattice models with long-range interactions or hopping, and in particular the spatio-temporal propagation of correlations and other physical quantities. The focus of the chapter was on the competition between linear, cone-like propagation and faster-than-linear, supersonic propagation. We illustrate this competition in two regimes, both relevant for experimental realizations of long-range many-body systems in cold atoms, ions, or molecules:

1. For small exponents $\alpha < 2$ we prove that supersonic propagation can occur. At the same time, in such systems cone-like spreading can be the dominant form of propagation, with supersonic effects appearing only as small corrections [as in Figure 4.5 (center)].
2. For intermediate exponents (roughly between 3 and 8), propagation is observed to be linear initially, with supersonic effects setting in at larger times and distances [as in Figures 4.1 (center) and 4.3 (right)].

To explain these observations, we provide model calculations as well as general bounds that provide a comprehensive and consistent picture of the various shapes of propagation fronts that can occur. Two of the results are Lieb-Robinson-type bounds, valid for large classes of models with long-range interactions. The first is a bound for models with exponents α smaller than the lattice dimension D , a regime for which previously no such bounds existed. Key to deriving the bound is the insight that for $\alpha < D$ the propagation speed in general scales asymptotically like a power law with the system size, and a meaningful bound therefore has to be derived in rescaled time τ as defined in (4.1.8). In physical time t , the bound then describes the increase of the propagation speed with increasing lattice size, as illustrated in Figure 4.2. The second Lieb-Robinson-type bound we report is essentially a cheat, as we stop half way through the derivation of a “conventional” Lieb-Robinson bound. Specializing this result to single-site observables and Hamiltonians with pair interactions only, we obtain an expression that can be evaluated numerically in an efficient way, easily reaching system sizes of $\mathcal{O}(10^4)$. This bound (4.2.2) is sharp enough to capture cone-like as well as supersonic behavior. In experimental studies of propagation in long-range interacting lattice models [99, 56], the currently feasible lattice sizes are small and measured data can be compared to results from exact diagonalization. However, experimental work on systems of larger size is in progress, and exact diagonalization will not be feasible in that case. We expect that the matrix exponential bound (4.2.2) can provide guidance and sanity checks when analyzing the results of such experiments.

In the second half of the chapter we complemented the bounds with results of one of the simplest long-range quantum models, namely a fermionic long-range hopping model in one dimension. We observed that cone-like propagation fronts can be a dominant feature also for small values of α , and we explain the opening angle of such a cone, as well as the interplay of cone-like and supersonic features, on the basis of the dispersion relation combined with the density of states. These results indicate that it will depend crucially on the k -modes occupied whether cone-like or supersonic propagation is dominant. We expect that such an improved understanding can provide guidance for optimizing experimental efforts to harness long-range interactions in a va-

CHAPTER 4. INTERPLAY OF SOUND CONE AND SUPERSONIC DYNAMICS

79

riety of quantum information and signaling tasks.

Chapter 5

Outlook and preliminary results

This thesis contains some of the first analytic results on nonequilibrium dynamics of long-range interacting quantum spin systems. In this chapter we present two possible future avenues along which ideas and results presented in the previous chapters may be exploited.

5.1 Spreading of correlations in initially correlated states

To date Lieb-Robinson bounds have only been used to derive upper bounds on the spreading of entanglement, information and correlations starting from initially uncorrelated states. It would be interesting to see if these bounds can be extended to initially entangled states. If so, how will the presence of long-range interactions affect the shapes of the causal fronts?

The long-range interacting Ising model with initial states taken from the class of orthogonal initial states would serve as an ideal testing bed for studying the spread of correlations. For example, it is straightforward to construct a GHZ multipartite entangled state that belongs to the class of orthogonal initial states. The exact results of Chapter 2 can then be used to determine connected correlation functions. Plotting the connected correlation functions in the (δ, t) -plane, similar to Chapter 3, we can study the shapes of the causal front and compare to (possible) theoretical predictions.

5.2 Many body localization

Another interesting avenue to explore, that has become exceedingly popular in recent years, is the phenomenon of many body localization. For recent reviews on the subject see [86, 1]. Section 5.2.1 shows an example of how level statistics can be used to study a crossover that hints at the possibility of a many-body localization-delocalization transition. The effect of long-ranged hopping and interactions are introduced in Section 5.2.2. In Section 5.2.3 we comment on the use of the exact analytic results of the long-range interacting Ising model to explore the fully many-body localized regime.

5.2.1 Many body localization in finite-range systems

The many body localization-delocalization transition is often studied, in finite ranged hopping and interacting systems, using exact diagonalization of specific models. One such model, studied by Oganesyan and Huse [87], managed to capture the characteristics of the transition using the level statistics of the underlying Hamiltonian. In this section we summarize their work and give an intuition about the many-body localization-delocalization transition.

Consider spinless fermions hopping and interacting on a one dimensional lattice of length L with a random on-site potential and periodic boundary conditions. This model only has two states, empty and occupied, and the Hamiltonian is given by

$$H = \sum_i \left[w_i n_i + V \left(n_i - \frac{1}{2} \right) \left(n_j - \frac{1}{2} \right) + t \left(c_i^\dagger c_{i+1} + c_{i+1}^\dagger c_i \right) + t' \left(c_i^\dagger c_{i+2} + c_{i+2}^\dagger c_i \right) \right]. \quad (5.2.1)$$

The nearest neighbour interaction is chosen to be $V = 2$. The hopping matrix elements, to both nearest and second nearest neighbour, are chosen to be $t = t' = 1$. The second nearest neighbour hopping is included so that the model remains nonintegrable, hence delocalized, at zero disorder. The authors chose on-site potentials w_i from a Gaussian distribution with mean zero and variance W^2 . In this framework W is a measure of the disorder in the system.

The level statistics of the many-body Hamiltonian (5.2.1) serves as the

testing bed for exploring the localization-delocalization transition. In the localized phase, in the large system limit, the eigenstates are localized in the many-body Fock basis of localized single-particle orbitals. This implies that states that are close in energy are far apart in this Fock space and do not interact or show level repulsion. Hence, nearby energy levels are Poisson distributed. On the other hand, in the delocalized phase the level statistics of a large sample are those of random matrix theory and follow the Gaussian orthogonal ensemble. In the finite sized systems considered, the level statistics cross over smoothly between these two limiting cases as the strength of the random potential is varied. The crossover becomes sharper as the size of the system L is increased and hints at the possibility of a phase transition at some critical disorder strength W_c in the large system limit. We can look for this phase transition using finite-size scaling techniques.

To perform the finite-size scaling we require a dimensionless measure of the spectral statistical properties. Specifically, we consider gaps between adjacent energy levels

$$\delta_n = E_{n+1} - E_n \geq 0, \quad (5.2.2)$$

where the eigenvalues $\{E_n\}$ are listed in increasing order. The dimensionless quantity that captures the correlation between adjacent energy gaps is the ratio of two consecutive gaps,

$$0 \leq r_n = \frac{\min[\delta_n, \delta_{n-1}]}{\max[\delta_n, \delta_{n-1}]} \leq 1. \quad (5.2.3)$$

For an uncorrelated spectrum the probability distribution of the r -ratio is Poissonian,

$$P_P(r) = \frac{2}{(1+r)^2} \quad (5.2.4)$$

with a mean of $\langle r \rangle_P = 2 \ln 2 - 1 \approx 0.39$. When the spectrum is correlated the r -ratio follows the Gaussian orthogonal ensemble with mean $\langle r \rangle_{GOE} \approx 0.53$.

Figure 5.1 (right) shows $\langle r \rangle$ of the many-body Hamiltonian (5.2.1). For strong disorder $W > 8$ larger samples show more Poisson-like statistics in an

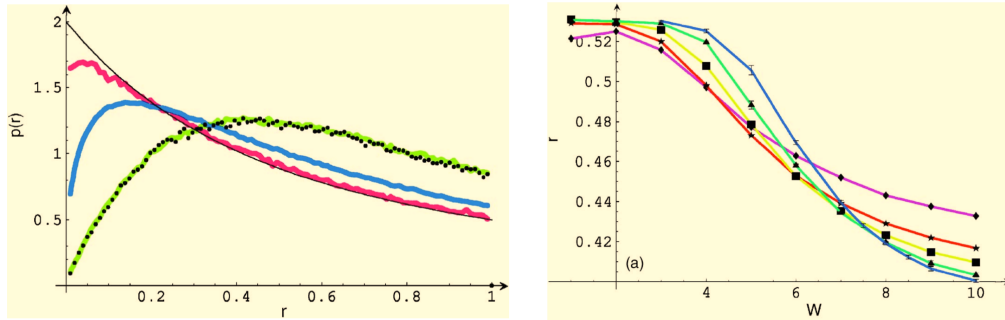


Figure 5.1: (Reproduced from [87]) Left panel: Disorder averaged probability distribution $P(r)$ for Poisson (solid black curve) and Gaussian orthogonal ensemble distributed eigenvalues (dotted black curve). The green curve shows the distribution for $W = 3$ in the delocalized regime. Pink data corresponds to the localized regime with $W = 11$ while blue data shows an intermediate regime with $W = 7$. Right panel: Size and disorder dependencies of the r -ratio. The curves correspond to $L = 8$ (diamonds), 10 (stars), 12 (squares), 14 (triangles), 16 (unadorned) from top to bottom for large W .

apparently localized regime. Weak disorder $W < 4$ show level statistics that converge to the Gaussian orthogonal ensemble with increasing system size, this corresponds to the delocalized phase.

In a related work [90] Pal and Huse study the many-body localization-delocalization transition in the nearest neighbour Heisenberg model with on-site disorder,

$$H = \sum_{i=1}^L [w_i \sigma_i^z + J (\sigma_i^x \sigma_{i+1}^x + \sigma_i^y \sigma_{i+1}^y + \sigma_i^z \sigma_{i+1}^z)]. \quad (5.2.5)$$

In this work they perform a finite-size scaling analysis using the dynamic polarization which is a measure of spin transport across a one-dimensional system at infinite temperature. To be precise, we perturb the initial infinite temperature density matrix with a small (long-wavelength) inhomogeneous spin modulation of the form

$$F = \sum_j \sigma_j^z e^{2\pi i j / L} \quad (5.2.6)$$

and measure the relaxation of this inhomogeneous polarization at infinite time. For each disorder realization η and eigenstate k , the contribution to the dy-

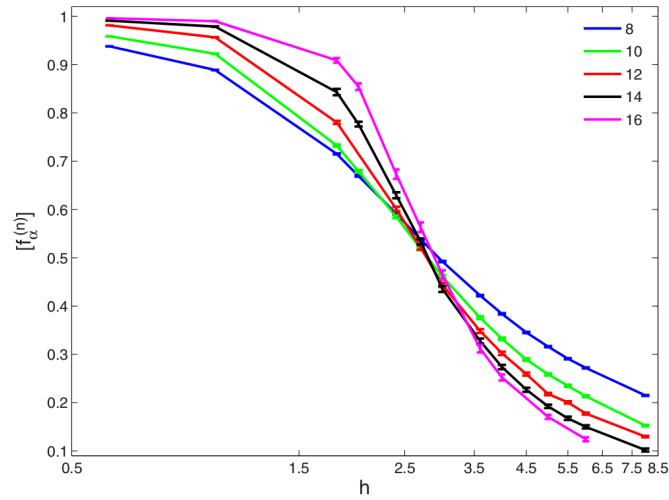


Figure 5.2: (Reproduced from [90]) Finite-size scaling of the dynamic polarization $[f_\alpha^{(n)}] = D$ (see text) for the one-dimensional Heisenberg model with on-site disorder of [90].

dynamic polarization is given by

$$D_\eta^k = 1 - \frac{\langle k|F^\dagger|k\rangle\langle k|F|k\rangle}{\langle k|F^\dagger F|k\rangle}. \quad (5.2.7)$$

D is then defined as the infinite temperature disorder average of D_η^k . As $L \rightarrow \infty$, in the delocalized phase, we expect that $D \rightarrow 1$ since the initial inhomogeneity relaxes away. On the other hand, in the many-body localized phase we expect $D \rightarrow 0$ since there is no transport.

Similar to $\langle r \rangle$ in Figure 5.1 the crossover from the delocalized to localized phase, as depicted by the dynamic polarization in Figure 5.2, becomes sharper for increasing system size. This hints at the possibility of a phase transition at a critical disorder W_c in the large system limit.

5.2.2 Many body localization in long-ranged systems

How does the range of interaction or hopping effect the many-body localization-delocalization transition? Yao and coworkers [122] have addressed this ques-

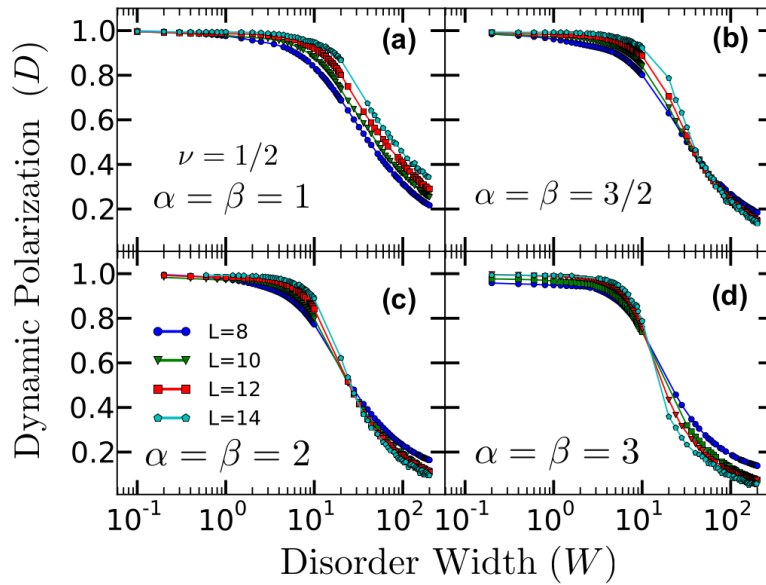


Figure 5.3: (Reproduced from [122]) Finite-size scaling of the dynamic polarization D_{η}^k (see text) of the one-dimensional XXZ -model with on-site disorder (5.2.8) for different flip-flop and interaction exponents. Throughout ν corresponds to the filling factor, i.e. the ratio of up to down spins.

tion for the XXZ model with random on-site potentials,

$$H = \sum_i w_i \sigma_i^z - \sum_{i,j} \frac{t_{ij}}{|i-j|^\alpha} (\sigma_i^x \sigma_j^x + \sigma_i^y \sigma_j^y) + \sum_i \frac{V_{ij}}{|i-j|^\beta}. \quad (5.2.8)$$

As in the work of Pal and Huse [90] they study the finite-size scaling of the dynamic polarization and witness a sharper transition for increasing system size (see Figure 5.3). An additional interesting observation of Yao and coworkers is the α and β dependencies of the localization-delocalization transition as depicted in Figure 5.3. For $\alpha = \beta = 2$ Figure 5.3 (c) hints at a phase transition at some critical disorder W_c in the large system limit. When $\alpha = \beta = 3/2$, Figure 5.3 (b), it is not possible to make any conclusions about the presence of a phase transition. Finally, in Figure 5.3 (a) showing $\alpha = \beta = 1$, the dynamic polarizations do not cross for increasing system size and hints that the system will not exhibit the many-body localization-delocalization transition.

Phil Anderson showed in his seminal paper [2] that long-ranged hopping $t \propto 1/r^\alpha$ delocalizes any localized single particle state for $\alpha \leq D$, where D is

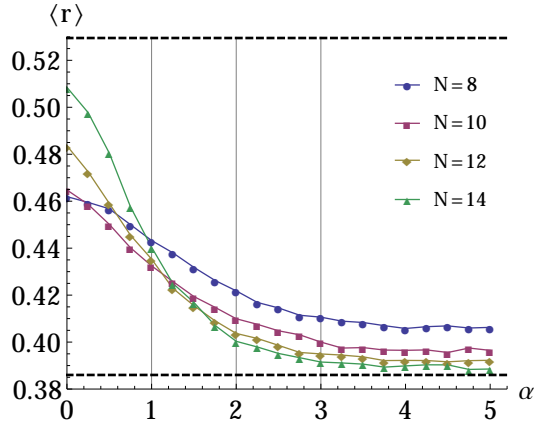


Figure 5.4: Left panel: Mean of r as a function of hopping exponent α for disorder $W = 9$ (strong disorder regime of [87]). The top and bottom dashed black lines indicate the means corresponding to the Gaussian orthogonal and Poissonian ensembles respectively.

the dimension of the underlying space. In [122] Yao and coworkers attempt to generalize this Anderson's criterion to long-range interacting and hopping systems. Surprisingly their results show that the critical values of the hopping and interacting exponents might be larger than the dimension of the underlying system.

Inspired by the results of [122] we extend the results of Oganesyan and Huse [87] to a one-dimensional long-range hopping model,

$$H = \sum_{i=1}^L \left[w_i n_i + V \left(n_i - \frac{1}{2} \right) \left(n_{i+1} - \frac{1}{2} \right) \right] + \sum_{i=1}^L \sum_{j=1}^{L/2} \frac{1}{j^\alpha} \left(c_i^\dagger c_{i+j} + c_{i+j}^\dagger c_i \right) \quad (5.2.9)$$

with periodic boundary conditions and a power-law hopping coupling matrix. We use exact diagonalization and the scheme outlined in Section 5.2.1 to determine the level statistics of the Hamiltonian (5.2.9) with half-filling. Instead of studying the finite size scaling of $\langle r \rangle$ as a function of disorder W we pick a disorder and study the scaling as a function of α , see Figure 5.4. Similar to the results of [87, 90, 122] the transition from the delocalized to localized phase becomes sharper as the system size increases. These results hint at the existence of a critical $\alpha = \alpha_c$ below which the system, in the thermodynamic limit, is in the many-body delocalized phase. Drawing some inspiration from the analytic

results of the long-range hopping fermionic model (4.3.1) we *conjecture that the critical value will be $\alpha_c = 2$* . Naturally the model (5.2.9) can be extended to include both long-range hopping and interactions. These generalizations give results similar to Figure 5.4.

The downside of these studies is that we are limited to small system sizes because we have to make use of exact diagonalization in order to determine the level statistics. Nonetheless, these numerical studies achieve the goal of giving us some intuition regarding the many-body localization-delocalization transition.

5.2.3 Fully many body localized systems

A quantum many body system is said to be fully many body localized when the disorder is strong enough to suppress any diffusive behaviour. The phenomenology of fully many body localized systems has been eloquently explained by Huse and coworkers [51]. Their reasoning goes as follows: Suppose we have a system of N local two-state degrees of freedom $\{\sigma_i\}$. We refer to these as the physical bits. Let us further assume that the time evolution of the physical bits is governed by a Hamiltonian with quenched disorder and strictly short-range interactions. For sufficiently strong disorder such a Hamiltonian can be in the fully many body localized regime, wherein all the many body eigenstates of the Hamiltonian are localized. In this context we can define a set of localized two-state degrees of freedom, with Pauli operators $\{\tau_i\}$, called localized bits. When the Hamiltonian is written in terms of these new localized bits it takes the form

$$H = E_0 + \sum_i \tau_i^z + \sum_{i,j} J_{i,j} \tau_i^z \tau_j^z + \sum_{i,j,\{k\}}^{\infty} K_{i\{k\}j}^{(n)} \tau_i^z \tau_{k_1}^z \dots \tau_{k_n}^z \tau_j^z \quad (5.2.10)$$

where the sums are restricted such that each term appears only once and E_0 is some constant energy. The typical magnitudes of the interactions $J_{i,j}$ and $K_{i\{k\}j}^{(n)}$ fall off exponentially with distance. Heuristically the above construction makes sense since the fully many body localized state should have a set of localized conserved charges which are constants of motion of the system. These are then given by the τ_i^z terms in the Hamiltonian (5.2.10).

Studying the Hamiltonian (5.2.10) we cannot help but notice the similarity with the long-range interacting Ising model. Indeed, similar methods used to determine exact expressions for the two-spin correlation functions (see Appendix A) can be used to determine analytic expressions for time dependent correlations functions governed by the fully many body localized Hamiltonian (5.2.10). Previous results on many body localization relied on exact diagonalization of the Hamiltonian. With this method only small system sizes can be considered. Using the tools developed in this thesis the fully many body localized phase can easily be studied for large systems sizes, even on normal desktop computers.

Another interesting question is whether the signatures of many body localization persist when the system is coupled to a bath. These results can also be studied analytically using the exact expressions for two-spin correlation functions in the presence of a Markovian bath [31].

Appendices

Appendix A

Systematic Calculation of Correlators

In this appendix we give a detailed description of the calculation of exact expressions for the correlation functions of the long-range interacting Ising model.

A.1 Expressing $\prod_i \sigma_i^\pm \prod_j \sigma_j^\mp$ in the Heisenberg Picture

The unitary group of *-automorphisms

$$\alpha_t^\Lambda(\mathcal{O}) : \mathcal{O} \mapsto e^{iHt} \mathcal{O} e^{-iHt} \quad (\text{A.1.1})$$

is the most general way of expressing a time evolved operator in the Heisenberg picture. Since the long-range interacting Ising Hamiltonian (2.1.2) commutes with σ_j^z for all $j \in \Lambda$, the σ_j^z Pauli operators are preserved under time evolution governed by the Hamiltonian (2.1.2). Therefore we need only be concerned with the x and y Pauli operators, σ_j^x and σ_j^y . Calculating the time evolution of

$$\sigma_i^\pm := \frac{1}{2} (\sigma_i^x + i\sigma_i^y) \quad (\text{A.1.2})$$

enables us to study the time evolution of both the Pauli x and y operators at the same time. The real and imaginary parts of $\alpha_t^\Lambda(\sigma_i^\pm)$ respectively correspond to the time evolved Pauli x and y operators. Since the interaction and magnetic terms of the Hamiltonian (2.1.2) commute among themselves we can separate their effects and consider their respective contributions to the time evolution separately.

Let us first calculate the time evolution of a single operator,

$$\alpha_t^\Lambda(\sigma_i^\pm) \tag{A.1.3}$$

$$= \exp \left[i \frac{t}{2} \sum_{(i,j) \in \Lambda \times \Lambda} J_{i,j} \sigma_i^z \sigma_j^z - h i \sum_{i \in \Lambda} \sigma_i^z \right] \sigma_i^\pm \exp \left[-i \frac{t}{2} \sum_{(i,j) \in \Lambda \times \Lambda} J_{i,j} \sigma_i^z \sigma_j^z + h i \sum_{i \in \Lambda} \sigma_i^z \right]. \tag{A.1.4}$$

The contribution from the magnetic terms can be written as,

$$\exp \left[-i h \sum_{j \in \Lambda} \sigma_j^z \right] \sigma_i^\pm \exp \left[i h \sum_{k \in \Lambda} \sigma_k^z \right] \tag{A.1.5}$$

$$\begin{aligned} &= \exp [-i h \sigma_i^z] \sigma_i^\pm \exp [i h \sigma_i^z] \\ &= [\cos(ht) - i \sigma_i^z \sin(ht)] \sigma_i^\pm [\cos(ht) + i \sigma_i^z \sin(ht)] \\ &= \sigma_i^\pm \cos^2(ht) + i \frac{1}{2} [\sigma_i^\pm, \sigma_i^z] \sin(2ht) + \sigma_i^z \sigma_i^\pm \sigma_i^z \sin^2(ht) \\ &= \sigma_i^\pm \cos(2ht) \mp i \sigma_i^\pm \sin(2ht) \\ &= \sigma_i^\pm \exp [\mp 2i h t]. \end{aligned} \tag{A.1.6}$$

The first step follows from the fact that the majority of the terms pass through σ_i^\pm because they have support on different lattice sites. Only the operators on lattice site i cannot be ignored. Notice that the contribution from the magnetic terms (A.1.6) amounts to a rotation and plays a role similar to Larmor precession. Since we are mainly interested in the equilibration behaviour of long-range interacting spin systems we may ignore the magnetic contribution by setting $h = 0$.

Next we calculate the contribution to the time evolution given by the in-

teraction terms. For ease of calculation define

$$P_i := \sum_{k \in \Lambda \setminus i} J_{k,i} \sigma_k^z. \quad (\text{A.1.7})$$

Then similar to the previous calculation we find

$$\begin{aligned} & \exp \left[i \frac{t}{2} \sum_{(j,k) \in \Lambda \times \Lambda} J_{j,k} \sigma_j^z \sigma_k^z \right] \sigma_i^\pm \exp \left[-i \frac{t}{2} \sum_{(l,m) \in \Lambda \times \Lambda} J_{l,m} \sigma_l^z \sigma_m^z \right] \\ &= \exp [itP_i \sigma_i^z] \sigma_i^\pm \exp [-itP_i \sigma_i^z] \\ &= [\cos (tP_i \sigma_i^z) + i \sigma_i^z \sin (tP_i)] \sigma_i^\pm [\cos (tP_i) - i \sigma_i^z \sin (tP_i)] \\ &= \sigma_i^\pm \cos^2 (tP_i) + i \frac{1}{2} [\sigma_i^z, \sigma_i^\pm] \sin (2tP_i) + \sigma_i^z \sigma_i^\pm \sigma_i^z \sin^2 (tP_i) \\ &= \sigma_i^\pm \cos (2tP_i) + i \sigma_i^\pm \sin (2tP_i) \\ &= \sigma_i^\pm \exp [\pm 2itP_i]. \end{aligned} \quad (\text{A.1.8})$$

Using (A.1.6) and (A.1.9) we can write the time evolved σ_i^\pm as

$$\alpha_t^\Lambda (\sigma_i^\pm) = \sigma_i^\pm \exp [\pm 2itP_i] \exp [\mp 2iht]. \quad (\text{A.1.10})$$

In the following we determine the time evolution governed by the interaction terms on products of σ^\pm operators. For products of σ_i^\pm and σ_j^\mp let

$$\mathfrak{P} := \{p(1), \dots, p(N)\} \quad (\text{A.1.11})$$

and

$$\mathfrak{Q} := \{q(1), \dots, q(N)\} \quad (\text{A.1.12})$$

be two mutually disjoint sets of the lattice Λ containing lattice sites $p(i)$ and $q(j)$ respectively. Let

$$\mathfrak{R} := \mathfrak{P} \cup \mathfrak{Q} \quad (\text{A.1.13})$$

$$= \{p(1), \dots, p(N), q(1), \dots, q(M)\}$$

$$=: \{r(1), \dots, r(N), r(N+1), \dots, q(N+M)\}. \quad (\text{A.1.14})$$

For ease of calculation define

$$P(k) := \sum_{l \in \Lambda \setminus \mathfrak{R}} J_{r(k),l} \sigma_l^z. \quad (\text{A.1.15})$$

As a first step the time evolution of the product can be written as

$$\exp \left[\frac{t}{2} \sum_{(j,k) \in \Lambda \times \Lambda} J_{j,k} \sigma_j^z \sigma_k^z \right] \prod_{n=1}^N \sigma_{p(n)}^\pm \prod_{m=1}^M \sigma_{q(m)}^\mp \exp \left[-\frac{t}{2} \sum_{(l,m) \in \Lambda \times \Lambda} J_{l,m} \sigma_l^z \sigma_m^z \right] \quad (\text{A.1.16})$$

$$= \exp \left[it \sum_{k=1}^{N+M} P(k) \sigma_{r(k)}^z \right] \prod_{n=1}^N \sigma_{r(n)}^\pm \prod_{m=N+1}^{N+M} \sigma_{r(m)}^\mp \exp \left[-it \sum_{l=1}^{N+M} P(l) \sigma_{r(l)}^z \right]. \quad (\text{A.1.17})$$

The factor 1 in stead of 1/2 in front of the sums is because we have combined terms proportional to $J_{r(k),l}$ and $J_{l,r(k)}$. Next, we insert the identity between the product terms and regroup, noticing that only terms with $\sigma_{r(k)}^z$ in the exponential make a contribution to the time evolution of $\sigma_{r(k)}^\pm$,

$$\exp \left[it \sum_{k=1}^{N+M} P(k) \sigma_{r(k)}^z \right] \prod_{n=1}^N \sigma_{r(n)}^\pm \exp \left[-it \sum_{k=1}^{N+M} P(k) \sigma_{r(k)}^z \right] \quad (\text{A.1.18})$$

$$\times \exp \left[it \sum_{l=1}^{N+M} P(l) \sigma_{r(l)}^z \right] \prod_{m=N+1}^M \sigma_{r(m)}^\mp \exp \left[-it \sum_{l=1}^{N+M} P(l) \sigma_{r(l)}^z \right] \quad (\text{A.1.19})$$

$$= \prod_{n=1}^N \left\{ \exp [itP(n) \sigma_{r(n)}^z] \sigma_{r(n)}^\pm \exp [-itP(n) \sigma_{r(n)}^z] \right\} \quad (\text{A.1.20})$$

$$\times \prod_{m=N+1}^M \left\{ \exp [itP(m) \sigma_{r(m)}^z] \sigma_{r(m)}^\mp \exp [-itP(m) \sigma_{r(m)}^z] \right\}. \quad (\text{A.1.21})$$

Lastly, we make use of (A.1.9) for the time evolution of single $\sigma_{r(k)}^\pm$ operators, giving

$$\prod_{n=1}^N \sigma_{r(n)}^\pm \exp [\pm 2itP(n)] \prod_{m=N+1}^M \sigma_{r(m)}^\mp \exp [\mp 2itP(m)] \quad (\text{A.1.22})$$

$$= \prod_{p \in \mathfrak{P}} \sigma_p^\pm \prod_{q \in \mathfrak{Q}} \sigma_q^\mp \exp \left[\pm 2it \left(\sum_{r=1}^N P(r) - \sum_{s=N+1}^{N+M} P(m) \right) \right]. \quad (\text{A.1.23})$$

A similar calculation shows that

$$\exp \left[i \frac{t}{2} \sum_{(j,k) \in \Lambda \times \Lambda} J_{j,k} \sigma_j^z \sigma_k^z \right] \prod_{n=1}^N \sigma_{p(n)}^{\pm} \prod_{m=1}^N \sigma_{q(m)}^{\pm} \exp \left[-i \frac{t}{2} \sum_{(l,m) \in \Lambda \times \Lambda} J_{l,m} \sigma_l^z \sigma_m^z \right] \quad (\text{A.1.24})$$

$$= \prod_{p \in \mathfrak{P}} \sigma_p^{\pm} \prod_{q \in \Omega} \sigma_q^{\pm} \exp \left[\pm 2it \left(\sum_{r=1}^N P(r) + \sum_{s=N+1}^{N+M} P(m) \right) \right]. \quad (\text{A.1.25})$$

Including the contribution from the magnetic terms we may write

$$\begin{aligned} & \alpha_t \left(\prod_{n=1}^N \sigma_{p(n)}^{\pm} \prod_{m=1}^N \sigma_{q(m)}^{\pm} \right) \quad (\text{A.1.26}) \\ &= \prod_{n=1}^N \sigma_{p(n)}^{\pm} \prod_{m=1}^N \sigma_{q(m)}^{\pm} \exp \left\{ \pm 2it \left[\left(\sum_{r=1}^N P(r) + \sum_{s=N+1}^{N+M} P(m) \right) - 2(M+N)h \right] \right\} \quad (\text{A.1.27}) \end{aligned}$$

and

$$\begin{aligned} & \alpha_t \left(\prod_{n=1}^N \sigma_{p(n)}^{\pm} \prod_{m=1}^N \sigma_{q(m)}^{\mp} \right) \quad (\text{A.1.28}) \\ &= \prod_{n=1}^N \sigma_{p(n)}^{\pm} \prod_{m=1}^N \sigma_{q(m)}^{\mp} \exp \left\{ \pm 2it \left[\left(\sum_{r=1}^N P(r) - \sum_{s=N+1}^{N+M} P(m) \right) - 2(M-N)h \right] \right\} \quad (\text{A.1.29}) \end{aligned}$$

A.2 Correlation Functions With Orthogonal Initial States

In the section we show how to calculate arbitrary time dependent correlation functions of the long-range Ising model given initial states within the class of orthogonal initial states [see Definition 2.2.1]. Taking the expectation value of time dependent products of σ^{\pm} [see Equations (A.1.27) and (A.1.29)] operators

we can write

$$\left\langle \prod_{n=1}^N \sigma_{p(n)}^{\pm} \prod_{m=1}^M \sigma_{q(m)}^{\mp} \right\rangle (t) \quad (\text{A.2.1})$$

$$= \text{Tr} \left\{ \alpha_t \left[\prod_{n=1}^N \sigma_{p(n)}^{\pm} \prod_{m=1}^M \sigma_{q(m)}^{\mp} \right] \rho(0) \right\} \quad (\text{A.2.2})$$

$$= \text{Tr} \left\{ \left(\prod_{n=1}^N \sigma_{p(n)}^{\pm} \right) \left(\prod_{m=1}^M \sigma_{q(m)}^{\mp} \right) \exp \left[\pm 2it \left(\sum_{k=1}^N P(k) - \sum_{l=N+1}^{N+M} P(l) \right) \right] \rho(0) \right\} \quad (\text{A.2.3})$$

$$= \text{Tr} \left\{ \left(\prod_{n=1}^N \sigma_{p(n)}^{\pm} \right) \left(\prod_{m=1}^M \sigma_{q(m)}^{\mp} \right) \rho(0) \right\} \prod_{r \in \Lambda \setminus \mathfrak{P} \cup \Omega} \cos \left[2t \left(\sum_{k=1}^N J_{r,p(k)} - \sum_{l=1}^M J_{r,q(l)} \right) \right] \quad (\text{A.2.4})$$

$$= \left\langle \left(\prod_{n=1}^N \sigma_{p(n)}^{\pm} \right) \left(\prod_{m=1}^M \sigma_{q(m)}^{\mp} \right) \rho(0) \right\rangle \prod_{r \in \Lambda \setminus \mathfrak{P} \cup \Omega} \cos \left[2t \left(\sum_{k=1}^N J_{r,p(k)} - \sum_{l=1}^M J_{r,q(l)} \right) \right]. \quad (\text{A.2.5})$$

The third line follows from (A.1.23) and the final step follows from induction in the number of lattice sites $|\Lambda|$. Suppose we have $N + M + 1$ lattice sites, then each $P(k)$ only has a single term. Expanding the exponential in a Taylor series gives a cosine term, proportional to the identity matrix, and sine term, coupled to σ^z the z -Pauli matrix. After taking the trace only the cosine term survives. Now assume that the final step holds for any lattice with $N + M + n$ lattice sites then it easily follows that it also holds for $N + M + n + 1$ lattice sites. Hence the final step is true by mathematical induction.

Two specific cases of interest are that of the single- and two-spin correlation functions. In these cases, the above general formulas reduce to

$$\langle \sigma_i^{\pm} \rangle (t) = \langle \sigma_i^{\pm} \rangle (0) \prod_{k \in \Lambda \setminus i} \cos (2t J_{k,i}), \quad (\text{A.2.6})$$

$$\langle \sigma_i^{\pm} \sigma_j^{\pm} \rangle (t) = \langle \sigma_i^{\pm} \sigma_j^{\pm} \rangle (0) \prod_{r \in \Lambda \setminus \{i,j\}} \cos [2t (J_{r,i} + J_{r,j})] \quad (\text{A.2.7})$$

and

$$\langle \sigma_i^\pm \sigma_j^\mp \rangle(t) = \langle \sigma_i^\pm \sigma_j^\mp \rangle(0) \prod_{r \in \Lambda \setminus \{i,j\}} \cos [2t (J_{r,i} - J_{r,j})]. \quad (\text{A.2.8})$$

Now using the identities

$$4\sigma_i^\pm \sigma_j^\pm = \sigma_i^x \sigma_j^x - \sigma_i^y \sigma_j^y \pm i\sigma_i^x \sigma_j^y \pm i\sigma_i^y \sigma_j^x, \quad (\text{A.2.9})$$

$$4\sigma_i^\pm \sigma_j^\mp = \sigma_i^x \sigma_j^x + \sigma_i^y \sigma_j^y \mp i\sigma_i^x \sigma_j^y \pm i\sigma_i^y \sigma_j^x, \quad (\text{A.2.10})$$

we find

$$\sigma_i^x \sigma_j^x = 2\Re [\sigma_i^\pm \sigma_j^\mp + \sigma_i^\pm \sigma_j^\pm], \quad (\text{A.2.11})$$

$$\sigma_i^y \sigma_j^y = 2\Re [\sigma_i^\pm \sigma_j^\mp - \sigma_i^\pm \sigma_j^\pm], \quad (\text{A.2.12})$$

$$\sigma_i^x \sigma_j^y = \mp 2\Im [\sigma_i^\pm \sigma_j^\mp - \sigma_i^\pm \sigma_j^\pm], \quad (\text{A.2.13})$$

$$\sigma_i^y \sigma_j^x = \pm 2\Im [\sigma_i^\pm \sigma_j^\mp + \sigma_i^\pm \sigma_j^\pm]. \quad (\text{A.2.14})$$

Taking the real and imaginary parts of the correlation functions we can determine any of the two-spin correlations.

A.3 n -Time Correlators

The aim of this section is to give a systematic calculation of the n -time correlators

$$\left\langle \prod_{r=1}^N \alpha_{t_r} \left(\sigma_{p(r)}^\pm \right) \prod_{s=1}^M \alpha_{\tau_s} \left(\sigma_{q(s)}^\mp \right) \right\rangle \quad (\text{A.3.1})$$

where each operator σ_i^\pm is time evolved for a different (possibly the same) time t_i , after which expectation values are taken with respect to an orthogonal

initial state $\rho(0)$. As a first step let us only consider

$$\begin{aligned}
& \prod_{r=1}^N \alpha_{t_r} \left(\sigma_{p(r)}^{\pm} \right) \prod_{s=1}^M \alpha_{\tau_s} \left(\sigma_{q(s)}^{\mp} \right) \tag{A.3.2} \\
&= \prod_{r=1}^N \sigma_{p(r)}^{\pm} \exp \left[\pm 2i t_r P_{p(r)} \right] \prod_{s=1}^M \sigma_{q(s)}^{\mp} \exp \left[\mp 2i \tau_s P_{q(s)} \right] \\
&= \sigma_{p(1)}^{\pm} \exp \left[\pm 2i \left(\sum_{r=2}^N t_r J_{p(r),p(1)} - \sum_{s=1}^M \tau_s J_{q(s),p(1)} \right) \sigma_{p(1)}^z \right] \\
&\quad \exp \left[\pm 2i t_1 J_{p(1),p(2)} \sigma_{p(2)}^z \right] \sigma_{p(2)}^{\pm} \exp \left[\pm 2i \left(\sum_{r=3}^N t_r J_{p(r),p(2)} - \sum_{s=1}^M \tau_s J_{q(s),p(2)} \right) \sigma_{p(2)}^z \right] \\
&\quad \dots \\
&\quad \exp \left[\pm 2i \sum_{r=1}^{N-1} t_r J_{p(r),p(N)} \sigma_{p(N)}^z \right] \sigma_{p(N)}^{\pm} \exp \left[\mp 2i \sum_{s=1}^M \tau_s J_{q(s),p(N)} \sigma_{p(N)}^z \right] \\
&\quad \exp \left[\pm 2i \sum_{r=1}^N t_r J_{p(r),q(1)} \sigma_{q(1)}^z \right] \sigma_{q(1)}^{\mp} \exp \left[\mp 2i \sum_{s=2}^M \tau_s J_{q(s),q(1)} \sigma_{q(1)}^z \right] \\
&\quad \exp \left[\pm 2i \left(\sum_{r=1}^N t_r J_{p(r),q(2)} - \tau_1 J_{q(1),q(2)} \right) \sigma_{q(2)}^z \right] \sigma_{q(2)}^{\mp} \exp \left[\mp 2i \sum_{s=3}^M \tau_s J_{q(s),q(2)} \sigma_{q(2)}^z \right] \\
&\quad \dots \\
&\quad \exp \left[\pm 2i \left(\sum_{r=1}^N t_r J_{p(r),q(M)} - \sum_{s=1}^{M-1} \tau_s J_{q(s),q(M)} \right) \sigma_{q(M)}^z \right] \sigma_{q(M)}^{\mp}
\end{aligned}$$

As seen from (A.1.9), time evolving σ_j^{\pm} yields an exponential term containing the sum of z -Pauli matrices on all lattice sites except $j \in \Lambda$. The third line above then follows by rearranging the terms such that σ_j^{\pm} is wedged between exponential terms containing z -Pauli matrices defined on lattice site j . Two distinct types of terms are present in the above expression,

$$\exp \left[\pm 2i \sum_{s \neq m} t_s J_{p(m),p(s)} \sigma_{p(m)}^z \right] \sigma_{p(m)}^{\pm} \exp \left[\pm 2i \left(\sum_{r \neq m} t_r J_{p(r),p(m)} - \sum_{s=1}^M \tau_s J_{q(s),p(m)} \right) \sigma_{p(m)}^z \right] \tag{A.3.3}$$

and

$$\exp \left[\pm 2i \left(\sum_{r=1}^N t_r J_{p(r),q(n)} - \sum_{r \neq n} \tau_r J_{q(r),q(n)} \right) \sigma_{q(n)}^z \right] \sigma_{q(n)}^{\mp} \exp \left[\mp 2i \sum_{s \neq n} \tau_s J_{q(s),q(n)} \sigma_{q(n)}^z \right] \quad (\text{A.3.4})$$

Now notice that if A and B are two real numbers then we can write

$$\exp(\pm iA\sigma^z) \sigma^{\pm} \exp(\pm iB\sigma^z) = \sigma^{\pm} \exp[i(A - B)] \quad (\text{A.3.5})$$

and

$$\exp(\pm iA\sigma^z) \sigma^{\mp} \exp(\mp iB\sigma^z) = \sigma^{\mp} \exp[i(A + B)]. \quad (\text{A.3.6})$$

Using the above identities we can write the sum of all the exponential terms as

$$\begin{aligned} & \sum_{r=1}^M \sum_{s=1}^N (\tau_r - t_s) J_{q(r),p(s)} + \sum_{k=1}^{N-1} \sum_{l=k+1}^N (t_k - t_l) J_{p(l),p(k)} + \sum_{k=1}^{M-1} \sum_{l=k+1}^M (\tau_l - \tau_k) J_{q(l),q(k)} \\ =: & \mathbf{S}(M, N) \end{aligned} \quad (\text{A.3.7})$$

The product of operators, time evolved for different times (A.3.2), can then be written as

$$\begin{aligned} & \prod_{r=1}^N \alpha_{t_r} \left(\sigma_{p(r)}^{\pm} \right) \prod_{s=1}^M \alpha_{\tau_s} \left(\sigma_{q(s)}^{\mp} \right) \\ = & \prod_{r=1}^N \alpha_{t_r} \left(\sigma_{p(r)}^{\pm} \right) \prod_{s=1}^M \alpha_{\tau_s} \left(\sigma_{q(s)}^{\mp} \right) \exp[2it\mathbf{S}(M, N)] \exp \left[\pm 2it \left(\sum_{k=1}^N t_k P(k) - \sum_{l=N+1}^{N+M} \tau_{l-N} P(l) \right) \right]. \end{aligned} \quad (\text{A.3.8})$$

From the above expression the correlation function then trivially follows,

$$\begin{aligned} & \left\langle \prod_{r=1}^N \alpha_{t_r} \left(\sigma_{p(r)}^{\pm} \right) \prod_{s=1}^M \alpha_{\tau_s} \left(\sigma_{q(s)}^{\mp} \right) \right\rangle \quad (\text{A.3.9}) \\ = & \exp[2it\mathbf{S}(M, N)] \left\langle \prod_{r=1}^N \sigma_{p(r)}^{\pm} \right\rangle \prod_{k \in \Lambda \setminus \mathfrak{R}} \cos \left[2 \left(\sum_{r=1}^N t_r J_{p(r),k} - \sum_{s=1}^M \tau_s J_{q(s),k} \right) \right]. \end{aligned} \quad (\text{A.3.10})$$

A specific case of interest is the two-time correlation functions. In this case the correlators can be written as

$$\langle \sigma_i^\pm(t) \sigma_j^\pm(\tau) \rangle = \langle \sigma_i^\pm \sigma_j^\pm \rangle(0) e^{\pm 2i(t-\tau)J_{i,j}} \prod_{k \in \Lambda \setminus \{i,j\}} \cos [2(tJ_{i,k} + \tau J_{j,k})] \quad (\text{A.3.11})$$

and

$$\langle \sigma_i^\pm(t) \sigma_j^\mp(\tau) \rangle = \langle \sigma_i^\pm \sigma_j^\mp \rangle(0) e^{\mp 2i(t-\tau)J_{i,j}} \prod_{k \in \Lambda \setminus \{i,j\}} \cos [2(tJ_{i,k} - \tau J_{j,k})]. \quad (\text{A.3.12})$$

Appendix B

Lattice Independent Upper Bound

The aim of this appendix is to systematically derive the lattice independent upper bounds of the two-spin correlations functions [see Equations (2.5.2) and (2.5.3)] in the large system limit.

B.1 Proof of Equations (2.5.2) and (2.5.3)

The starting point for the derivation is the exact expression for the two-spin correlation functions (2.4.2)-(2.4.5). Specifically, we focus on the $\langle \sigma_i^x \sigma_j^x \rangle$ equal time correlation function,

$$\langle \sigma_i^x(t) \sigma_j^x(t) \rangle = \frac{1}{2} \langle \sigma_i^x(0) \sigma_j^x(0) \rangle (P_{i,j}^- + P_{i,j}^+), \quad (\text{B.1.1})$$

where $P_{i,j}^\pm$ is given as a product (over all lattice sites) of cosine terms [see equation (2.4.6)]. Since $|\cos x| \leq 1$, we can upper bound the absolute value of this quantity by a product over a subset of lattice sites,

$$P_{i,j}^\pm \leq \prod_{k \in \Lambda \setminus g_{i,j}^\pm(t)} \cos [(J_{k,i} \pm J_{k,j}) t], \quad (\text{B.1.2})$$

where we have defined

$$g_{i,j}^\pm(t) := \left\{ k \in \Lambda : |(J_{k,i} \pm J_{k,j}) t| \geq \frac{\pi}{2} \right\}. \quad (\text{B.1.3})$$

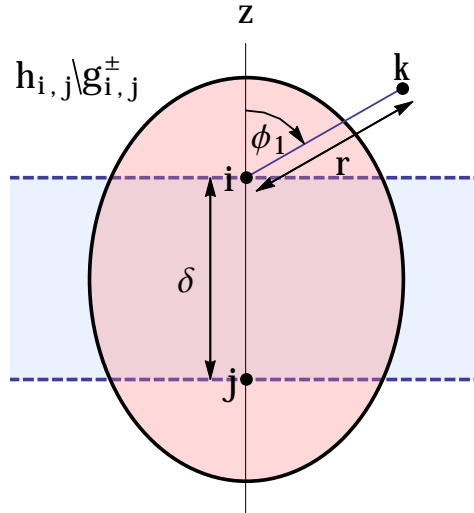


Figure B.1: Sketch of the regions $g_{i,j}^{\pm}(t)$ and $h_{i,j}$ and of the chosen coordinate system as used for the proof in Sec. B.1.

This subset is chosen such that, for all $k \in \Lambda \setminus g_{i,j}^{\pm}(t)$, we can make use of the inequality

$$|\cos(\pi x)| \leq 1 - 4x^2 \leq \exp(-4x^2), \quad (\text{B.1.4})$$

valid for all $|\pi x| < 2$, to write

$$P_{i,j}^{\pm} \leq \exp \left[- \left(\frac{2t}{\pi} \right)^2 \sum_{k \in \Lambda \setminus g_{i,j}^{\pm}(t)} (J_{k,i} \pm J_{k,j})^2 \right]. \quad (\text{B.1.5})$$

To simplify the calculation we restrict the k -summation even further by excluding the hyperslab $h_{i,j}$ sketched in Figure B.1. The occurrence of Euclidean distances in the couplings $J_{i,k}$ and $J_{j,k}$ then suggests to parametrise the lattice sites $k \in \Lambda$ by hyperspherical coordinates,

$$k(r, \phi_1, \dots, \phi_{d-1}) = \begin{pmatrix} r \cos \phi_1 \\ r \sin \phi_1 \cos \phi_2 \\ \vdots \\ r \sin \phi_1 \cdots \sin \phi_{d-2} \cos \phi_{d-1} \\ r \sin \phi_1 \cdots \sin \phi_{d-2} \sin \phi_{d-1} \end{pmatrix}, \quad (\text{B.1.6})$$

with the origin of the coordinate system placed at lattice site i and the z -axis chosen along the line connecting i and j . The couplings can then be written as

$$J_{i,k} = r^{-\alpha}, \quad J_{j,k} = (r^2 + 2r\delta \cos \phi_1 + \delta^2)^{-\alpha/2}, \quad (\text{B.1.7})$$

where $\delta = |i - j|$ denotes the distance between sites i and j . Exploiting also the reflection symmetry of the problem, we arrive at the bound

$$P_{i,j}^{\pm} \leq \exp\left(-\frac{8t^2}{\pi^2} \sum_{k \in h_{i,j} \setminus g_{i,j}^{\pm}(t)} (J_{k,i} \pm J_{k,j})^2\right) \quad (\text{B.1.8})$$

with the k -summation restricted to the lattice sites in the half plane

$$h_{i,j} = \left\{k(r, \phi_1, \dots, \phi_{d-1}) \in \Lambda : 0 \leq \phi_1 \leq \frac{\pi}{2}\right\}. \quad (\text{B.1.9})$$

For large lattices, we can bound the sum in (B.1.8) by an integral,

$$\begin{aligned} & \sum_{k \in h_{i,j} \setminus g_{i,j}^{\pm}(t)} (J_{k,i} \pm J_{k,j})^2 \\ & \geq 2\pi \mathcal{K}(D) \int_{R^{\pm}(t)}^{N^{1/D}} dr r^{D-1} \int_0^{\pi/2} d\phi_1 \cos \phi_1 \sin^{D-2} \phi_1 (J_{k,i} \pm J_{k,j})^2 \end{aligned} \quad (\text{B.1.10})$$

where the prefactor

$$\mathcal{K}(D) = \begin{cases} \frac{1}{\pi} & \text{for } D = 2, \\ \prod_{m=2}^{D-2} \frac{\sqrt{\pi} \Gamma(\frac{1}{2}(-m+D))}{\Gamma(\frac{1}{2}(1-m+D))} & \text{for } D \geq 3, \end{cases} \quad (\text{B.1.11})$$

originates from the integrations over $\phi_2, \dots, \phi_{D-1}$.

The lower limit R^{\pm} of the r -integration still needs to be determined such that the region $g_{i,j}^{\pm}$ is excluded. I.e., we need to determine R^{\pm} such that

$$|t(J_{k,i} \pm J_{k,j})| < \frac{\pi}{2} \quad (\text{B.1.12})$$

for all $r \geq R^{\pm}(t)$. We are interested in the long-time asymptotic behaviour, and in this limit large values of r are required to satisfy the above inequality.

Hence we can assume that r is much larger than δ and expand

$$\begin{aligned} J_{k,i} \pm J_{k,j} &= \frac{1}{r^\alpha} \pm \frac{1}{(\delta^2 + 2r\delta \cos \phi_1 + r^2)^{\alpha/2}} \\ &\sim r^{-\alpha} \pm r^{-\alpha} \left(1 + \frac{\alpha\delta \cos \phi_1}{r} \right) \end{aligned} \quad (\text{B.1.13})$$

to leading order in the small parameter δ/r , yielding

$$J_{k,i} + J_{k,j} \sim 2r^{-\alpha}, \quad (\text{B.1.14a})$$

$$J_{k,i} - J_{k,j} \sim -\frac{\alpha\delta \cos \phi_1}{r^{\alpha+1}}. \quad (\text{B.1.14b})$$

Inserting these asymptotic expressions into (B.1.12), we obtain

$$R^+(t) \sim \left(\frac{8t}{\pi} \right)^{1/\alpha}, \quad R^-(t) \sim \left(\frac{4\alpha\delta t}{\pi} \right)^{1/(1+\alpha)}, \quad (\text{B.1.15})$$

valid for sufficiently large t .

For similar reasons we can insert the expansions (B.1.14a) and (B.1.14b) into the integrand of (B.1.10). The integrations become elementary in this case, yielding

$$\sum_{k \in h_{i,j} \setminus g_{i,j}^\pm(t)} (J_{i,k} + J_{k,j})^2 \geq \frac{8\pi\mathcal{K}(D)}{(D-1)(D-2\alpha)} \left[N^{1-2\alpha/D} - \left(\frac{8t}{\pi} \right)^{D/\alpha-2} \right], \quad (\text{B.1.16})$$

$$\sum_{k \in h_{i,j} \setminus g_{i,j}^\pm(t)} (J_{i,k} - J_{k,j})^2 \geq \frac{4\pi\mathcal{K}(D)\alpha^2\delta^2}{(D^2-1)(D-2\alpha-2)} \left[N^{1-2(\alpha+1)/D} - \left(\frac{4\alpha\delta t}{\pi} \right)^{D/(\alpha+1)-2} \right], \quad (\text{B.1.17})$$

in the limit of large N and t . Interestingly, the bound in (B.1.16) is independent of the distance δ between the lattice sites.

Depending on the sign of the exponents $1-2\alpha/D$ and $1-2(\alpha+1)/D$ in the N -terms, either the first or the second term in the square brackets of (B.1.16) and (B.1.17) will give the dominant contribution in the limit of large system size N . As a result, the asymptotic behaviour of the bounds is different for

different ranges of α ,

$$\sum_{k \in h_{i,j} \setminus g_{i,j}^{\pm}(t)} (J_{i,k} + J_{k,j})^2 \geq \frac{8\pi\mathcal{K}(D)}{(D-1)(D-2\alpha)} \begin{cases} N^{1-2\alpha/D} & \text{for } 0 \leq \alpha < D/2, \\ -\left(\frac{8t}{\pi}\right)^{D/\alpha-2} & \text{for } \alpha > D/2, \end{cases} \quad (\text{B.1.18})$$

$$\sum_{k \in h_{i,j} \setminus g_{i,j}^{\pm}(t)} (J_{i,k} - J_{k,j})^2 \geq \frac{4\pi\mathcal{K}(D)\alpha^2\delta^2}{(D^2-1)(D-2\alpha-2)} \begin{cases} N^{1-2(\alpha+1)/D} & \text{for } 0 \leq \alpha < D/2 - 1, \\ -\left(\frac{4\alpha\delta t}{\pi}\right)^{D/(\alpha+1)-2} & \text{for } \alpha > D/2 - 1. \end{cases} \quad (\text{B.1.19})$$

Inserting these expressions into the inequality (B.1.5) and defining the positive constants

$$C_{\alpha,D}^+ = \frac{\pi\mathcal{K}(D)}{(D-1)|D-2\alpha|}, \quad (\text{B.1.20})$$

$$C_{\alpha,D}^- = \frac{2\pi\mathcal{K}(D)}{(D^2-1)|D-2\alpha-2|}, \quad (\text{B.1.21})$$

the main results (2.5.2) and (2.5.3) of section 2.5 follow.

Appendix C

Lower Bounds on Information Propagation

In this appendix we present detailed calculations of the lower bound on information propagation of an Ising-type Hamiltonian of the form

$$H = \frac{1}{2}(\mathbb{1} - \sigma_0^z) \sum_{j \in B} \frac{1}{(1 + \delta_{0,j})^\alpha} (\mathbb{1} - \sigma_j^z) \quad (\text{C.0.1})$$

with product and more general mixed initial states.

C.1 Product Initial State

Choose an initial product state of the form

$$\rho = |0\rangle\langle 0|^{\Lambda - |B|} \otimes |+\rangle\langle +|^{\otimes |B|}. \quad (\text{C.1.1})$$

For the quantum channel representing free time evolution we have $|0\rangle_0$ at site $0 \in \Lambda$. It then follows that

$$\text{Tr}_{\Lambda \setminus B} [\exp(-itH)\rho \exp(itH)] = |+\rangle\langle +|^{\otimes |B|}. \quad (\text{C.1.2})$$

This then leads to

$$\text{Tr} [\text{Tr}_{\Lambda \setminus B} [\exp(-itH)\rho \exp(itH)] |+\rangle\langle +|^{\otimes |B|}] = 1. \quad (\text{C.1.3})$$

APPENDIX C. LOWER BOUNDS ON INFORMATION PROPAGATION 106

For the quantum channel with the local spin flip we need to determine

$$\mathrm{Tr}_{\Lambda \setminus B} [\exp(-itH) |1\rangle_0 \langle 0| \rho |0\rangle_0 \langle 1| \exp(itH)] \quad (\text{C.1.4})$$

$$= \mathrm{Tr}_{\Lambda \setminus B} [e^{-itH} |1\rangle_0 \langle 1| \otimes |0\rangle \langle 0|^{|A|-|B|-1} \otimes |+\rangle \langle +|^{\otimes |B|} e^{itH}] \quad (\text{C.1.5})$$

Now, since we have $|1\rangle_0$ at site $0 \in \Lambda$ the argument of the exponential will not be zero and we will find some time evolution in the sites $j \in B$. Each of the $|+\rangle_j$ terms then evolve as

$$\exp \left[-it \frac{1 - \sigma_j^z}{(1 + \delta_{0,j})^\alpha} \right] |+\rangle_j \quad (\text{C.1.6})$$

$$= \exp \left[-it \frac{1 - \sigma_j^z}{(1 + \delta_{0,j})^\alpha} \right] \frac{1}{\sqrt{2}} (|0\rangle_j + |1\rangle_j) \quad (\text{C.1.7})$$

$$= \frac{1}{\sqrt{2}} \left(|0\rangle_j + \exp \left[-\frac{2it}{(1 + \delta_{0,j})^\alpha} \right] |1\rangle_j \right). \quad (\text{C.1.8})$$

Hence, when taking the trace we have $|B|$ terms of the form

$${}_j \langle + | \exp \left[-it \frac{1 - \sigma_j^z}{(1 + \delta_{0,j})^\alpha} \right] |+\rangle_j \langle + | \exp \left[it \frac{1 - \sigma_j^z}{(1 + \delta_{0,j})^\alpha} \right] |+\rangle_j \quad (\text{C.1.9})$$

$$= \frac{1}{2} \left[1 + \cos \left(\frac{2t}{(1 + \delta_{0,j})^\alpha} \right) \right]. \quad (\text{C.1.10})$$

It then follows that

$$\mathrm{Tr} \left\{ \mathrm{Tr}_{\Lambda \setminus B} [\exp(-itH) |1\rangle_0 \langle 0| \rho |0\rangle_0 \langle 1| \exp(itH)] |+\rangle \langle +|^{\otimes |B|} \right\} \quad (\text{C.1.11})$$

$$= \frac{1}{2^{|B|}} \prod_{j \in B} \left[1 + \cos \left(\frac{2t}{(1 + \delta_{0,j})^\alpha} \right) \right]. \quad (\text{C.1.12})$$

So, the probability of detecting a signal p_t at time $t > 0$ can be written as

$$p_t = 1 - \frac{1}{2^{|B|}} \prod_{j \in B} \left[1 + \cos \left(\frac{2t}{(1 + \delta_{0,j})^\alpha} \right) \right]. \quad (\text{C.1.13})$$

For times such that

$$2t < (1 + \delta_{0,j})^\alpha, \quad (\text{C.1.14})$$

we can make use of the fact that

$$\cos x \leq 1 - \frac{2x^2}{5} \quad (\text{C.1.15})$$

for all $x \in [0, 1]$ to get

$$p_t \geq 1 - \prod_{j \in B} \left[1 - \frac{4t^2}{5[1 + \delta_{0,j}]^\alpha} \right]. \quad (\text{C.1.16})$$

Using that

$$\ln(1 - x) \leq -x \quad (\text{C.1.17})$$

for all $x \geq 0$ we find

$$p_t \geq 1 - \exp \left[-\frac{4t^2}{5} \sum_{j \in B} (1 + \delta_{0,j})^{-2\alpha} \right]. \quad (\text{C.1.18})$$

For short times and in the large B , and hence system, limit the above equation serves as a lower bound on the propagation of information when starting from the product initial state (C.1.1).

C.2 Entangled Initial state

Choose an entangled initial state of the form

$$\rho = |0\rangle\langle 0|^{|A|-|B|} \otimes |\psi\rangle\langle\psi|, \quad (\text{C.2.1})$$

with

$$|\psi\rangle = (|0, \dots, 0\rangle + |1, \dots, 1\rangle)/\sqrt{2}. \quad (\text{C.2.2})$$

For the quantum channel representing free time evolution we have

$$\text{Tr} \{ \text{Tr}_{A \setminus B} [\exp(-itH)\rho \exp(itH)] |\psi\rangle\langle\psi| \} \quad (\text{C.2.3})$$

$$= \text{Tr} \{ |\psi\rangle\langle\psi| \cdot |\psi\rangle\langle\psi| \} \quad (\text{C.2.4})$$

$$= 1. \quad (\text{C.2.5})$$

When performing a spin flip at site $0 \in \Lambda$ we will have terms of the form

$$\exp \left[-it \sum_{j \in B} \frac{\mathbb{1} - \sigma_j^z}{(1 + \delta_{0,j})^\alpha} \right] |\psi\rangle \quad (\text{C.2.6})$$

$$= \frac{1}{\sqrt{2}} \left(|0, \dots, 0\rangle + \exp \left[2it \sum_{j \in B} \frac{1}{(1 + \delta_{0,j})^\alpha} \right] |1, \dots, 1\rangle \right). \quad (\text{C.2.7})$$

Taking the trace gives

$$\langle \psi | \exp \left[-it \sum_{j \in B} \frac{\mathbb{1} - \sigma_j^z}{(1 + \delta_{0,j})^\alpha} \right] |\psi\rangle \langle \psi | \exp \left[it \sum_{j \in B} \frac{\mathbb{1} - \sigma_j^z}{(1 + \delta_{0,j})^\alpha} \right] |\psi\rangle \quad (\text{C.2.8})$$

$$= \frac{1}{2} \left[1 + \cos \left(2t \sum_{j \in B} \frac{1}{(1 + \delta_{0,j})^\alpha} \right) \right]. \quad (\text{C.2.9})$$

The probability of detecting a signal in B at time $t > 0$ given a unitary perturbation in A is then given by

$$p_t = 1 - \frac{1}{2} \left[1 + \cos \left(2t \sum_{j \in B} \frac{1}{(1 + \delta_{0,j})^\alpha} \right) \right]. \quad (\text{C.2.10})$$

C.3 Supersonic propagation in the full long-range Ising Model

In this appendix we prove that supersonic transmission through a quantum channel can occur for any $\alpha < 2$, and measurements performed on single lattice sites. The proof uses techniques of [25] which are also shown in Appendix C.1 and Chapter 3 but applies them to a slightly more involved model.

Choose a finite one-dimensional lattice $\Lambda = \{1, \dots, L\}$ consisting of L sites. As nonoverlapping regions of the lattice we choose the left- and rightmost single sites $A = \{1\}$ and $B = \{L\}$. Defining $S = \Lambda \setminus (A \cup B)$, the Ising Hamiltonian

$$H = \frac{1}{2} \sum_{i < j} J_{ij} \sigma_i^z \sigma_j^z \quad (\text{C.3.1})$$

APPENDIX C. LOWER BOUNDS ON INFORMATION PROPAGATION 109

can be rewritten as

$$H = H_{AS} + H_{AB} + H_{SB} + H_{SS} \quad (\text{C.3.2})$$

where we define

$$H_{XY} := \frac{1}{2} \sum_{i \in X} \sum_{j \in Y} J_{ij} \sigma_i^z \sigma_j^z \quad (\text{C.3.3})$$

with X and Y taking the values $\{A, S, B\}$ as indicated above. As an initial state we choose

$$\rho(0) = |\downarrow\rangle_1 \langle \downarrow| \bigotimes_{s \in S} |\downarrow\rangle_s \langle \downarrow| \otimes |+\rangle_L \langle +| \quad (\text{C.3.4})$$

with $\sigma_i^z |\uparrow\rangle_i = |\uparrow\rangle_i$, $\sigma_i^z |\downarrow\rangle_i = -|\downarrow\rangle_i$, and

$$|+\rangle_j = \frac{1}{\sqrt{2}} \left(|\uparrow\rangle_j + |\downarrow\rangle_j \right). \quad (\text{C.3.5})$$

Initially all the spins are pointing downward except those in B which are pointing along σ^x .

Similar to before we implement a binary quantum channel evolving either with $\rho(0)$ (sending a “0”), or starting with $U_A \rho(0) \rho U_A^\dagger$ (sending a “1”), where U_A is a unitary supported on A only. As explained in Chapter 3, the classical information capacity can be lower bound by the probability to detect, by measuring according to a positive operator valued measure (POVM) π_B , a signal at B after a time t ,

$$C_t \geq p_t = \left| \text{Tr} \{N_t[\rho(0)] \pi_B\} - \text{Tr} \{T_t[\rho(0)] \pi_B\} \right| \quad (\text{C.3.6})$$

with

$$N_t[\rho(0)] := \text{Tr}_{A \setminus B} \left[e^{-iHt} \rho(0) e^{iHt} \right], \quad (\text{C.3.7})$$

$$T_t[\rho(0)] := \text{Tr}_{A \setminus B} \left[e^{-iHt} U_A \rho(0) U_A^\dagger e^{iHt} \right]. \quad (\text{C.3.8})$$

In the following we compute a lower bound on the right hand side of (C.3.6), and study this bound as a function of channel length, the distance between A

and B .

We choose $\pi_B = |+\rangle_L \langle +|$ and $U_A = |\uparrow\rangle_1 \langle \downarrow|$, where the latter is the spin flip operator on the first site. For the time-evolved density operator in (C.3.7) we find

$$e^{-iHt} \rho(0) e^{iHt} \quad (\text{C.3.9})$$

$$= e^{-iH_{AB}t} e^{-iH_{AS}t} e^{-iH_{SS}t} e^{-iH_{SB}t} \left[\bigotimes_{s=1}^{L-1} |\downarrow\rangle_s \langle \downarrow| \otimes |+\rangle_L \langle +| \right] e^{iH_{SB}t} e^{iH_{SS}t} e^{iH_{AS}t} e^{iH_{AB}t} \quad (\text{C.3.10})$$

$$= \bigotimes_{s=1}^{L-1} |\downarrow\rangle_s \langle \downarrow| \left\{ \exp \left[it \sum_{r=1}^{L-1} J_{rL} \sigma_L^z \right] |+\rangle_L \langle +| \exp \left[-it \sum_{r=1}^{L-1} J_{rL} \sigma_L^z \right] \right\}. \quad (\text{C.3.11})$$

All the exponentials not supported on B add up to zero since the initial state prepared on $\Lambda \setminus B$ is an eigenstate of the Ising Hamiltonian. Taking the partial trace over all but B we find

$$\text{Tr}_{\Lambda \setminus B} \{ N_t [\rho(0)] \pi_B \} \quad (\text{C.3.12})$$

$$= \text{Tr}_{\Lambda \setminus B} \left\{ \exp \left[it \sum_{r=1}^{L-1} J_{rL} \sigma_L^z \right] |+\rangle_L \langle +| \exp \left[-it \sum_{r=1}^{L-1} J_{rL} \sigma_L^z \right] \pi_B \right\} \quad (\text{C.3.13})$$

$$= {}_L \langle +| \exp \left[it \underbrace{\sum_{r=1}^{L-1} J_{rL} \sigma_L^z}_{:=A} \right] |+\rangle_L \langle +| \exp \left[-it \sum_{r=1}^{L-1} J_{rL} \sigma_L^z \right] |+\rangle_L \quad (\text{C.3.14})$$

$$= \frac{1}{4} [e^{itA} + e^{-itA}]^2 = \frac{1}{2} \left\{ 1 + \cos \left[2t \left(\sum_{r \in S} J_{rL} + J_{1L} \right) \right] \right\}. \quad (\text{C.3.15})$$

A similar calculation shows that

$$\text{Tr} \{ T_t [\rho(0)] \pi_B \} = \frac{1}{2} \left\{ 1 + \cos \left[2t \left(\sum_{r \in S} J_{rL} - J_{1L} \right) \right] \right\}. \quad (\text{C.3.16})$$

We can write

$$p_t = \left| \frac{1}{2} \cos \left[2t \left(\sum_{r \in S} J_{rL} + J_{1L} \right) \right] - \frac{1}{2} \cos \left[2t \left(\sum_{r \in S} J_{rL} - J_{1L} \right) \right] \right| \quad (\text{C.3.17})$$

$$= \left| \sin \left(2t \sum_{r \in S} J_{rL} \right) \sin (2t J_{1L}) \right|. \quad (\text{C.3.18})$$

A plot of p_t for various values of α is shown in Figure C.1.

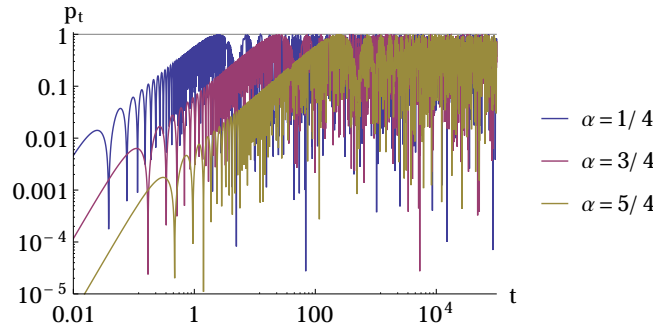


Figure C.1: Transmission probability p_t for chain length $L = 100$ and different values of α as indicated.

For intermediate times, the term $\sin(2tJ_{1L})$ with the smallest frequency determines an upper bound on p_t , before it saturates to 1. The bound follows a power law $t/(L-1)^\alpha$, as indicated in Figure C.1. The short-time behavior of p_t shows faster propagation, consistent with a power law proportional to $t^2/(L-1)^\alpha$; see Figure C.2. As in [25], only in this regime—before oscillatory behavior sets in—it is possible to derive a lower bound on p_t .

Using the inequality

$$\sin x \geq \frac{2x}{\pi} \quad \text{for } 0 \leq x \leq \pi/2, \quad (\text{C.3.19})$$

we obtain

$$p_t \geq \frac{4t}{\pi} \frac{1}{(L-1)^\alpha} \frac{4t}{\pi} \sum_{r=2}^{L-1} \frac{1}{(L-r)^\alpha}. \quad (\text{C.3.20})$$

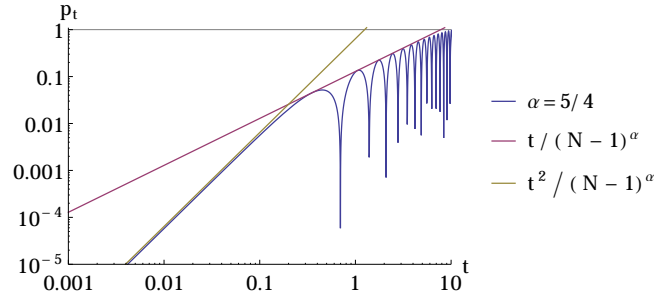


Figure C.2: Transmission probability p_t for chain length $L = 10$ with $\alpha = 5/4$. The straight lines indicate power law behavior $\propto t^2/(L-1)^\alpha$ for short times and $\propto t/(L-1)^\alpha$ for intermediate times (i.e., before saturation is reached).

Interpreting the sum as an upper Riemann sum, we have

$$\sum_{r=2}^{L-1} \frac{1}{(L-r)^\alpha} = \sum_{r=0}^{L-3} \frac{1}{r^\alpha} > \int_0^{L-2} \frac{dr}{(r+1)^\alpha}. \quad (\text{C.3.21})$$

Then we can write the bound on p_t as

$$p_t > \frac{16t^2}{\pi^2(\alpha-1)} \frac{1}{(L-1)^\alpha} \left[1 - \frac{1}{(L-1)^{\alpha-1}} \right] =: \underline{p}_t, \quad (\text{C.3.22})$$

valid for times

$$t \leq \frac{\pi}{4} \sqrt{\sum_{r=0}^{L-3} \frac{1}{r^\alpha}}. \quad (\text{C.3.23})$$

For $\alpha > 1$ and large L the second term in the square bracket in (C.3.22) is much smaller than 1, and we obtain

$$\underline{p}_t \sim \frac{16t^2}{\pi^2(\alpha-1)} \frac{1}{(L-1)^\alpha} \quad (\text{C.3.24})$$

for the large- L asymptotic behavior of the bound \underline{p}_t . In our setting, $\delta = L-1$ is the distance between the regions A and B . To determine the shape of the contour line at which \underline{p}_t is equal to some constant $\epsilon > 0$, we set

$$\epsilon = \underline{p}_t \propto \frac{t^2}{\delta^\alpha}. \quad (\text{C.3.25})$$

From this we can read off that

$$\delta \propto t^{2/\alpha} \tag{C.3.26}$$

along any of those contour lines. Equation (C.3.26) describes faster than linear spreading of classical information for any $\alpha < 2$. It is straightforward to extend the above calculation to more general initial conditions as well as to lattices of arbitrary dimension.

Appendix D

Calculation of Entanglement Measures

Von Neumann entanglement entropy and concurrence are two measures of bipartite entanglement. The first quantifies the amount of entanglement between a chosen subsystem and the rest of the system while the second quantifies the entanglement between two qubits. Both of these entanglement measures are simple to calculate using the exact results of Chapter 2. Spin squeezing is a measure of multipartite entanglement and is a little more tricky to calculate. The aim of this appendix is to calculate the time dependent spin squeezing starting from different initial states. Similar calculations to those performed below can also be found in [4, 121].

D.1 Spin Squeezing

Spin squeezing can be thought of as the minimum amount of uncertainty perpendicular to the mean spin direction. Using the single spin expectation values, the mean spin direction can be written as

$$\langle \boldsymbol{\sigma}(t) \rangle = \sum_{i \in \Lambda} (\langle \sigma_i^x(t) \rangle, \langle \sigma_i^y(t) \rangle, \langle \sigma_i^z(t) \rangle). \quad (\text{D.1.1})$$

Writing the mean spin vector in spherical polar coordinates, the polar and azimuthal angles θ and ϕ are given by

$$\theta = \arccos\left(\frac{\sum_{i \in \Lambda} \langle \sigma_i^z(t) \rangle}{R(t)}\right), \quad \phi = \arctan\left(\frac{\sum_{i \in \Lambda} \langle \sigma_i^y(t) \rangle}{\sum_{j \in \Lambda} \langle \sigma_j^x(t) \rangle}\right) \quad (\text{D.1.2})$$

with mean spin length

$$R(t) = \sqrt{\left(\sum_{i \in \Lambda} \langle \sigma_i^x(t) \rangle\right)^2 + \left(\sum_{i \in \Lambda} \langle \sigma_i^y(t) \rangle\right)^2 + \left(\sum_{i \in \Lambda} \langle \sigma_i^z(t) \rangle\right)^2}. \quad (\text{D.1.3})$$

Any vector directed to a point on the surface of a unit sphere can be written as

$$\mathbf{u} = (\sin \theta \cos \phi, \sin \theta \sin \phi, \cos \theta). \quad (\text{D.1.4})$$

The vector

$$\mathbf{n} = (-\cos \phi \cos \theta, -\sin \phi \cos \theta, \sin \theta) \quad (\text{D.1.5})$$

is perpendicular to \mathbf{u} . Taking the cross product of \mathbf{u} and \mathbf{n} we find another vector \mathbf{w} perpendicular to both \mathbf{u} and \mathbf{n} ,

$$\mathbf{w} = (-\sin \phi, \cos \phi, 0). \quad (\text{D.1.6})$$

Define the unit vector

$$\hat{n}_\psi := \sin \psi \mathbf{w} + \cos \psi \mathbf{n} = \begin{pmatrix} -\cos \psi \cos \phi \cos \theta - \sin \psi \sin \phi \\ -\cos \psi \cos \phi \sin \phi + \sin \psi \cos \phi \\ \cos \psi \sin \theta \end{pmatrix}^T. \quad (\text{D.1.7})$$

Sweeping over ψ defines a plane perpendicular to the original vector \mathbf{u} . Identifying \mathbf{u} with the mean spin direction we need to minimizing the uncertainty

$$\langle (\boldsymbol{\sigma} \cdot \hat{n}_\psi)^2 \rangle - \langle \boldsymbol{\sigma} \cdot \hat{n}_\psi \rangle^2 \quad (\text{D.1.8})$$

over ψ to determine the spin squeezing. The dot product can be written as

$$\begin{aligned} \boldsymbol{\sigma} \cdot \hat{n}_\psi = \sum_{i \in \Lambda} & [-\sigma_i^x (\sin \psi \sin \phi + \cos \psi \cos \theta \cos \phi) \\ & + \sigma_i^y (\sin \psi \cos \phi - \cos \psi \cos \theta \sin \phi) + \sigma_i^z \cos \psi \sin \theta]. \end{aligned} \quad (\text{D.1.9})$$

Taking the expectation value of (D.1.9) we notice that only the single spin expectation values are required to calculate it. The square of the dot product is a little more involved, and can be written as

$$\begin{aligned} & (\boldsymbol{\sigma} \cdot \hat{n}_\psi)^2 \quad (\text{D.1.10}) \\ = \sum_{i \in \Lambda} \sum_{j \in \Lambda \setminus \{i\}} & \left[\sigma_i^x \sigma_j^x (\sin \psi \sin \phi + \cos \psi \cos \theta \cos \phi)^2 \right. \\ & + \sigma_i^y \sigma_j^y (\sin \psi \cos \phi - \cos \psi \cos \theta \sin \phi)^2 + \sigma_i^z \sigma_j^z \cos^2 \psi \sin^2 \theta \\ & - (\sigma_i^x \sigma_j^y + \sigma_i^y \sigma_j^x) (\sin \psi \sin \phi + \cos \psi \cos \theta \cos \phi) \\ & \times (\sin \psi \cos \phi - \cos \psi \cos \theta \sin \phi) \\ & - (\sigma_i^x \sigma_j^z + \sigma_i^z \sigma_j^x) (\sin \psi \sin \phi + \cos \psi \cos \theta \cos \phi) \cos^2 \psi \sin^2 \theta \\ & \left. + (\sigma_i^y \sigma_j^z + \sigma_i^z \sigma_j^y) (\sin \psi \cos \phi - \cos \psi \cos \theta \sin \phi) \cos^2 \psi \sin^2 \theta \right] \\ & + |\Lambda|. \end{aligned} \quad (\text{D.1.11})$$

The final term arises when $i = j$ in the above sum. All the terms $\sigma_i^a \sigma_i^b + \sigma_i^b \sigma_i^a$ with $a \neq b$ equate to zero while the terms $\sigma_i^a \sigma_i^a$ are equal to the identity operator. The coefficient of the nonzero term simplifies to 1 using standard trigonometric identities. Taking the sum implies that each lattice site will contribute 1 to the sum. The time dependent expectation value of (D.1.11) can then easily be calculated using the exact two-spin correlation functions of the long-range interacting Ising model.

Bibliography

- [1] E. Altman and R. Vosk, *Universal dynamics and renormalization in many body localized systems*, ArXiv:1408.2834, 2014.
- [2] P. W. Anderson, *Absence of diffusion in certain random lattices*, Phys. Rev. **109** (1958), 1492.
- [3] M. Antoni and S. Ruffo, *Clustering and relaxation in Hamiltonian long-range dynamics*, Phys. Rev. E **52** (1995), 2361–2374.
- [4] S. Ashourisheikhi, *Spin squeezing of superposition of biaxial state and two qubit bell state*, Int. J. Theor. Phys. **53** (2004), 1103–1108.
- [5] A. Auerbach, *Interacting electrons and quantum magnetism*, Springer-Verlag, New York, 1994.
- [6] R. Bachelard and M. Kastner, *Universal threshold for the dynamical behavior of lattice systems with long-range interactions*, Phys. Rev. Lett. **110** (2013), 170603.
- [7] M. A. Baranov, M. Dalmonte, G. Pupillo, and P. Zoller, *Condensed Matter Theory of Dipolar Quantum Gases*, Chem. Rev. **112** (2012), 5012–5061.
- [8] E. H. Bareiss, *Numerical solution of linear equations with Toeplitz and Vector Toeplitz matrices*, Numerische Mathematik **13** (1969), 404–424.
- [9] C. Bennett and D. DiVincenzo, *Quantum information and computation*, Nature **404** (2000), 247–255.
- [10] M. J. Biercuk, H. Uys, A. P. VanDevender, N. Shiga, W. M. Itano, and J. J. Bollinger, *High-fidelity quantum control using ion crystals in a penning trap*, Quantum Inform. Comput. **9** (2009), 920–49.

- [11] O. Bratteli and D. W. Robinson, *Operator algebras and quantum statistical mechanics 2*, 2nd ed., Springer, Berlin, 1997.
- [12] S. Bravyi, M. Hastings, and F. Verstraete, *Lieb-Robinson Bounds and the Generation of Correlations and Topological Quantum Order*, Phys. Rev. Lett. **97** (2006), 050401.
- [13] J. W. Britton, B. C. Sawyer, A. C. Keith, C.-C. J. Wang, J. K. Freericks, H. Uys, M. J. Biercuk, and J. J. Bollinger, *Engineered two-dimensional Ising interactions in a trapped-ion quantum simulator with hundreds of spins*, Nature **484** (2012), 489–492.
- [14] P. Calabrese, F. H. L. Essler, and M. Fagotti, *Quantum Quench in the Transverse-Field Ising Chain*, Phys. Rev. Lett. **106** (2011), 227203.
- [15] ———, *Quantum quench in the transverse field ising chain I: Time evolution of order parameter correlators*, J. Stat. Mech. (2012), P07016.
- [16] ———, *Quantum quenches in the transverse field ising chain II: Stationary state properties*, J. Stat. Mech. (2012), P07022.
- [17] A. Campa, T. Dauxois, and S. Ruffo, *Statistical mechanics and dynamics of solvable models with long-range interactions*, Phys. Rep. **480** (2009), 57–159.
- [18] M. A. Cazalilla and M. Rigol, *Focus on dynamics and thermalization in isolated quantum many-body systems*, New J. Phys. **12** (2010), 055006.
- [19] J. I. Cirac, *Entanglement in many-body quantum systems*, 2012, arxiv:1205.3742, Chapter for the Proceedings of the les Houches school on “many-Body Physics with ultracold atoms”, 2010.
- [20] M. Cramer, C. M. Dawson, J. Eisert, and T. J. Osborne, *Exact relaxation in a class of nonequilibrium quantum lattice systems*, Phys. Rev. Lett. **100** (2008), 030602.
- [21] D. DeMille, *Quantum computation with trapped polar molecules*, Phys. Rev. Lett. **88** (2002), 067901.
- [22] F. J. Dyson, *Existence of a phase-transition in a one-dimensional Ising ferromagnet*, Commun. Math. Phys. **12** (1969), 91–107.

- [23] J. Eisert and D. Gross, *Supersonic quantum communication*, Phys. Rev. Lett. **102** (2009), 240501.
- [24] J. Eisert and T. J. Osborne, *General entanglement scaling laws from time evolution*, Phys. Rev. Lett. **97** (2006), 150404.
- [25] J. Eisert, M. van den Worm, S. R. Manmana, and M. Kastner, *Breakdown of quasi-locality in long-range quantum lattice models*, Phys. Rev. Lett. **111** (2013), 260401.
- [26] G. G. Emch, *Non-Markovian model for the approach to equilibrium*, J. Math. Phys. **7** (1966), 1198–1206.
- [27] J. Estève, C. Gross, A. Weller, S. Giovanazzi, and M. K. Oberthaler, *Squeezing and entanglement in a Bose-Einstein condensate*, Nature **455** (2008), 1216–1219.
- [28] A. Flesch, M. Cramer, I. P. McCulloch, U. Schollwöck, and J. Eisert, *Probing local relaxation of cold atoms in optical superlattices*, Phys. Rev. A **78** (2008), 033608.
- [29] M. Foss-Feig, Z.-X. Gong, C. W. Clark, and A. V. Gorshkov, *Nearly-linear light cones in long-range interacting quantum systems*.
- [30] M. Foss-Feig, K. R. A. Hazzard, J. J. Bollinger, and A. M. Rey, *Nonequilibrium dynamics of arbitrary-range Ising models with decoherence: An exact analytic solution*, Phys. Rev. A **87** (2013), 042101.
- [31] M. Foss-Feig, K. R. A. Hazzard, J. J. Bollinger, A. M. Rey, and C. W. Clark, *Dynamical quantum correlations of Ising models on an arbitrary lattice and their resilience to decoherence*, New J. Phys. **15** (2013), 113008.
- [32] A. Friedenauer, H. Schmitz, J. T. Glueckert, D. Porras, and T. Schaetz, *Simulating a quantum magnet with trapped ions*, Nature Phys. **4** (2008), 757–761.
- [33] A. Gabrielli, M. Joyce, and B. Marcos, *Quasistationary States and the Range of Pair Interactions*, Phys. Rev. Lett. **105** (2010), 210602.

- [34] M. Ghasemi Nezhadhighi and M. A. Rajabpour, *Entanglement dynamics in short- and long-range harmonic oscillators*, Phys. Rev. B **90** (2014), 205438.
- [35] S. Goldstein, J. L. Lebowitz, C. Mastrodonato, R. Tumulka, and N. Zanghì, *Approach to thermal equilibrium of macroscopic quantum systems*, Phys. Rev. E **81** (2010), 011109.
- [36] S. Goldstein, J. L. Lebowitz, R. Tumulka, and N. Zanghì, *Canonical typicality*, Phys. Rev. Lett. **96** (2006), 050403.
- [37] Z.-X. Gong and L. M. Duan, *Prethermalization and dynamic phase transition in an isolated trapped ion spin chain*, New J. Phys. **15** (2013), 113051.
- [38] Z.-X. Gong, M. Foss-Feig, S. Michalakis, and A. V. Gorshkov, *Persistence of locality in systems with power-law interactions*, Phys. Rev. Lett. **113** (2014), 030602.
- [39] A. V. Gorshkov, S. R. Manmana, G. Chen, J. Ye, E. Demler, M. D. Lukin, and A. M. Rey, *Tunable Superfluidity and Quantum Magnetism with Ultracold Polar Molecules*, Phys. Rev. Lett. **107** (2011), 115301.
- [40] D. Greif, T. Uehlinger, G. Jotzu, L. Tarruell, and T. Esslinger, *Short-Range Quantum Magnetism of Ultracold Fermions in an Optical Lattice*, Science **340** (2013), 1307–1310.
- [41] M. Gring, M. Kuhnert, T. Langen, T. Kitagawa, B. Rauer, M. Schreitl, I. Mazets, D. A. Smith, E. Demler, and J. Schmiedmayer, *Relaxation and Prethermalization in an Isolated Quantum System*, Science **337** (2012), 1318–1322.
- [42] C. Gross, T. Zibold, E. Nicklas, J. Estève, and M. K. Oberthaler, *Nonlinear atom interferometer surpasses classical precision limit.*, Nature **464** (2010), 1165–9.
- [43] M. B. Hastings and T. Koma, *Spectral gap and exponential decay of correlations*, Commun. Math. Phys. **265** (2006), 781–804.
- [44] P. Hauke and L. Tagliacozzo, *Spread of correlations in long-range interacting systems*, Phys. Rev. Lett. **111** (2013), 207202.

- [45] K. R. A. Hazzard, B. Gadway, M. Foss-Feig, B. Yan, S. A. Moses, J. P. Covey, N. Y. Yao, M. D. Lukin, J. Ye, D. S. Jin, and A. M. Rey, *Many-body dynamics of dipolar molecules in an optical lattice*, Phys. Rev. Lett. (2014), 195302.
- [46] K. R. A. Hazzard, S. R. Manmana, M. Foss-Feig, and A. M. Rey, *Far-from-equilibrium quantum magnetism with ultracold polar molecules*, Phys. Rev. Lett. **110** (2013), 075301.
- [47] K. R. A. Hazzard, M. van den Worm, M. Foss-Feig, S. R. Manmana, E. Dalla Torre, T. Pfau, M. Kastner, and A. M. Rey, *Quantum correlations and entanglement in far-from-equilibrium spin systems*, Phys. Rev. A **90** (2014), 063622.
- [48] R. Hildebrand, *Concurrence revisited*, J. Math. Phys. **48** (2007), 102108.
- [49] R. Horodecki, P. Horodecki, M. Horodecki, and K. Horodecki, *Quantum entanglement*, Rev. Mod. Phys. **81** (2009), 865–942.
- [50] S. F. Huelga, C. Macchiavello, T. Pellizzari, A. K. Ekert, M. B. Plenio, and J. I. Cirac, *Improvement of frequency standards with quantum entanglement*, Phys. Rev. Lett. **79** (1997), 3865–3868.
- [51] D. A. Huse, R. Nandkishore, and V. Oganesyan, *Phenomenology of fully many-body-localized systems*, Phys. Rev. B **90** (2014), 174202.
- [52] R. Islam, E. E. Edwards, K. Kim, S. Korenblit, C. Noh, H. Carmichael, G.-D. Lin, L.-M. Duan, C.-C. Joseph Wang, J.K. Freericks, and C. Monroe, *Onset of a quantum phase transition with a trapped ion quantum simulator*, Nat. Commun. **2** (2011), 377.
- [53] R. Islam, C. Senko, W. C. Campbell, S. Korenblit, J. Smith, A. Lee, E. E. Edwards, C.-C. J. Wang, J. K. Freericks, and C. Monroe, *Emergence and frustration of magnetism with variable-range interactions in a quantum simulator*, Science **340** (2013), 583–587.
- [54] N. T. Jacobson, L. C. Venuti, and P. Zanardi, *Unitary equilibration after a quantum quench of a thermal state*, Phys. Rev. A **84** (2011), 022115.

- [55] J. Jünemann, A. Cadarso, D. Pérez-García, A. Bermudez, and J. J. García-Ripoll, *Lieb-Robinson Bounds for Spin-Boson Lattice Models and Trapped Ions*, Phys. Rev. Lett. **111** (2013), 230404.
- [56] P. Jurcevic, B. P. Lanyon, P. Hauke, C. Hempel, P. Zoller, R. Blatt, and C. F. Roos, *Quasiparticle engineering and entanglement propagation in a quantum many-body system*, Nature **511** (2014), 202–205.
- [57] M. Kastner, *Nonequivalence of ensembles for long-range quantum spin systems in optical lattices*, Phys. Rev. Lett. **104** (2010), 240403.
- [58] ———, *Nonequivalence of ensembles in the Curie-Weiss anisotropic quantum Heisenberg model*, J. Stat. Mech. **2010** (2010), P07006.
- [59] ———, *Diverging Equilibration Times in Long-Range Quantum Spin Models*, Phys. Rev. Lett. **106** (2011), 130601.
- [60] ———, *Long-time asymptotics of the long-range Emch-Radin model*, Cent. Eur. J. Phys. **10** (2012), 637–644.
- [61] M. Kastner and M. van den Worm, *Relaxation timescales and prethermalization in d -dimensional long-range quantum spin models*, Phys. Scr (2015), no. T165, 14039.
- [62] G. Kaur, A. Ajoy, and P. Cappellaro, *Decay of spin coherences in one-dimensional spin systems*, New J. Phys. **15**, 093035.
- [63] K. Kim, M.-S. Chang, R. Islam, S. Korenblit, L.-M. Duan, and C. Monroe, *Entanglement and Tunable Spin-Spin Couplings between Trapped Ions Using Multiple Transverse Modes*, Phys. Rev. Lett. **103** (2009).
- [64] K. Kim, M.-S. Chang, S. Korenblit, R. Islam, E.E. Edwards, J.K. Freericks, G.-D. Lin, L.-M. Duan, and C. Monroe, *Quantum simulation of frustrated ising spins with trapped ions*, Nature **465** (2010), 590–593.
- [65] M. Kitagawa and M. Ueda, *Squeezed spin states*, Phys. Rev. A **47** (1993), 5138–5143.
- [66] M. Kliesch, C. Gogolin, and J. Eisert, *Lieb-Robinson bounds and the simulation of time evolution of local observables in lattice systems*, Many-

- Electron Approaches in Physics, Chemistry and Mathematics (L. D. Site and V. Bach, eds.), Springer, Berlin, 2014, pp. 301–318.
- [67] T. Koffel, M. Lewenstein, and L. Tagliacozzo, *Entanglement Entropy for the Long-Range Ising Chain in a Transverse Field*, Phys. Rev. Lett. **109** (2012), 267203.
- [68] J. K. Korbicz, J. I. Cirac, and M. Lewenstein, *Spin Squeezing Inequalities and Entanglement of N Qubit States*, Phys. Rev. Lett. **95** (2005), 120502.
- [69] S. Korenblit, D. Kafri, W. C. Campbell, R. Islam, E. E. Edwards, Z.-X. Gong, G.-D. Lin, L.-M. Duan, J. Kim, K. Kim, and C. Monroe, *Quantum simulation of spin models on an arbitrary lattice with trapped ions*, New J. Phys. **14** (2012), 095024.
- [70] Claudine Lacroix, Philippe Mendels, and Frederic Mila (eds.), *Introduction to frustrated magnetism*, Springer, Heidelberg, 2011.
- [71] T. Lahaye, C. Menotti, L. Santos, M. Lewenstein, and T. Pfau, *The physics of dipolar bosonic quantum gases*, Rep. Prog. Phys. **72** (2009), 126401.
- [72] B. P. Lanyon, C. Hempel, D. Nigg, M. Müller, R. Gerritsma, F. Zähringer, P. Schindler, J. T. Barreiro, M. Rambach, G. Kirchmair, M. Hennrich, P. Zoller, R. Blatt, and C. F. Roos, *Universal Digital Quantum Simulation with Trapped Ions*, Science **334** (2011), 57–61.
- [73] J. I. Latorre and A. Riera, *A short review on entanglement in quantum spin systems*, J. Phys. A **42** (2009), 504002.
- [74] E. H. Lieb and D. W. Robinson, *The finite group velocity of quantum spin systems*, Commun. Math. Phys. **28** (1972), 251–257.
- [75] N. Linden, S. Popescu, A. J. Short, and A. Winter, *Quantum mechanical evolution towards thermal equilibrium*, Phys. Rev. E **79** (2009), 061103.
- [76] R. Löw, H. Weimer, J. Nipper, J.B. Balewski, Björn Butscher, H.P. Büchler, and T. Pfau, *An experimental and theoretical guide to strongly interacting rydberg gases*, J. Phys. B: At. Mol. Opt. Phys. **45** (2012), 113001.

- [77] D. Lynden-Bell and R. Wood, *The gravo-thermal catastrophe in isothermal spheres and the onset of red-giant structure for stellar systems*, Mon. Not. R. Astron. Soc. **138** (1968), 495–525.
- [78] M. Maik, P. Hauke, O. Dutta, J. Zakrzewski, and M. Lewenstein, *Quantum spin models with long-range interactions and tunnelings: a quantum Monte Carlo study*, New J. Phys. **14** (2012), 113006.
- [79] M. J. Martin, M. Bishof, M. D. Swallows, X. Zhang, C. Benko, J. von Stecher, A. V. Gorshkov, A. M. Rey, and Jun Ye, *A Quantum Many-Body Spin System in an Optical Lattice Clock*, Science **341** (2013), 632–636.
- [80] D. Métivier, R. Bachelard, and M. Kastner, *Spreading of Perturbations in Long-Range Interacting Classical Lattice Models*, Phys. Rev. Lett. **112** (2014), 210601.
- [81] A. Micheli, G. K. Brennen, and P. Zoller, *A toolbox for lattice-spin models with polar molecules*, Nature Phys. **2** (2006), 341–347.
- [82] M. Moeckel and S. Kehrein, *Interaction quench in the Hubbard model*, Phys. Rev. Lett. **100** (2008), 175702.
- [83] C. Moler and C. Van Loan, *Nineteen dubious ways to compute the exponential of a matrix, twenty-five years later*, SIAM Rev. **45** (2003), 3–49.
- [84] K. Mølmer and A. Sørensen, *Multiparticle Entanglement of Hot Trapped Ions*, Phys. Rev. Lett. **82** (1999), 1835–1838.
- [85] B. Nachtergaele, Y. Ogata, and R. Sims, *Propagation of Correlations in Quantum Lattice Systems*, J. Stat. Phys. **124** (2006), 1–13.
- [86] R. Nandkishore and D. A. Huse, *Many-body localization and thermalization in quantum statistical mechanics*, Annu. Rev. Condens. Matter Phys. (2015).
- [87] V. Oganesyan and D. A. Huse, *Localization of interacting fermions at high temperature vademecum*, Phys. Rev. B **75** (2007), 155111.
- [88] B. Olmos, D. Yu, Y. Singh, F. Schreck, K. Bongs, and I. Lesanovsky, *Long-Range Interacting Many-Body Systems with Alkaline-Earth-Metal Atoms*, Phys. Rev. Lett. **110** (2013), 143602.

- [89] F. W. J. Olver, D. W. Lozier, R. F. Boisvert, and C. W. Clark (eds.), *NIST Handbook of Mathematical Functions*, Cambridge University Press, Cambridge, 2010.
- [90] A. Pal and D. A. Huse, *Many-body localization phase transition arXiv preprint*, Phys. Rev. B **82** (2010), 174411.
- [91] D. Peter, S. Müller, S. Wessel, and H. P. Büchler, *Anomalous behaviour of spin systems with dipolar interactions*, Phys. Rev. Lett. **109** (2012), 025303.
- [92] D. Porras and J. I. Cirac, *Effective Quantum Spin Systems with Trapped Ions*, Phys. Rev. Lett. **92** (2004), 207901.
- [93] S. Prawer and A. D. Greentree, *Diamond for Quantum Computing*, Science **320** (2008), 1601–1602.
- [94] C. Radin, *Approach to Equilibrium in a Simple Model*, J. Math. Phys. **11** (1970), 2945–2955.
- [95] M. A. Rajabpour and S. Sotiriadis, *Quantum quench in long-range field theories*, Phys. Rev. B **91** (2015), 045131.
- [96] P. Reimann, *Foundation of statistical mechanics under experimentally realistic conditions*, Phys. Rev. Lett. **101** (2008), 190403.
- [97] ———, *Canonical thermalization*, New J. Phys. **12** (2010), 055027.
- [98] P. Reimann and M. Kastner, *Equilibration of isolated macroscopic quantum systems*, New J. Phys. **14** (2012), 043020.
- [99] P. Richerme, Z.-X. Gong, A. Lee, C. Senko, J. Smith, M. Foss-Feig, S. Michalakis, A. V. Gorshkov, and C. Monroe, *Non-local propagation of correlations in quantum systems with long-range interactions*, Nature **511** (2014), 198–201.
- [100] M. Rigol, V. Dunjko, and M. Olshanii, *Thermalization and its mechanism for generic isolated quantum systems*, Nature **452** (2008), 854–858.
- [101] O. Bratteli D. R. Robinson, *Operator algebras and quantum statistical mechanics*, Springer, 2002.

- [102] S. Sachdev, *Quantum magnetism and criticality*, Nature Physics **4** (2008), 173.
- [103] ———, *Quantum Phase Transitions*, second ed., Cambridge University Press, Cambridge, 2011.
- [104] J. Schachenmayer, B. P. Lanyon, C. F. Roos, and A. J. Daley, *Entanglement growth in quench dynamics with variable range interactions*, Phys. Rev. X **3** (2013), 031015.
- [105] P. Schaub, M. Cheneau, M. Endres, T. Fukuhara, S. Hild, Ahmed Omran, T. Pohl, C. Gross, S. Kuhr, and I. Bloch, *Observation of spatially ordered structures in a two-dimensional rydberg gas*, Nature **87** (2012), 491.
- [106] A. J. Short and T. C. Farrelly, *Quantum equilibration in finite time*, New J. Phys. **14** (2012), 013063.
- [107] J. Simon, W. S. Bakr, M. Ruichao, M. E. Tai, P. M. Preiss, and M. Greiner, *Quantum simulation of antiferromagnetic spin chains in an optical lattice*, Nature **472** (2011), 307.
- [108] M. Srednicki, *Chaos and quantum thermalization*, Phys. Rev. E **50** (1994), 888–901.
- [109] D.M. Storch, M. van den Worm, and M. Kastner, *Interplay of soundcone and supersonic propagation in lattice models with power law interactions*, New J. Phys. **17** (2015), 063021.
- [110] J. Struck, C. Ölschläger, R. Le Targat, P. Soltan-Panahi, A. Eckardt, M. Lewenstein, P. Windpassinger, and K. Sengstock, *Quantum Simulation of Frustrated Classical Magnetism in Triangular Optical Lattices*, Science **333** (2011), 996–999.
- [111] M. D. Swallows, M. Bishof, Y. Lin, S. Blatt, M. J. Martin, A. M. Rey, and J. Ye, *Suppression of Collisional Shifts in a Strongly Interacting Lattice Clock*, Science **331** (2011), 1043–1046.
- [112] W. Thirring, *Systems with negative specific heat*, Z. Phys. **235** (1970), 339–352.

- [113] S. Trotzky, P. Cheinet, S. Fölling, M. Feld, U. Schnorrberger, A. M. Rey, A. Polkovnikov, E. A. Demler, M. D. Lukin, and I. Bloch, *Time-Resolved Observation and Control of Superexchange Interactions with Ultracold Atoms in Optical Lattices*, *Science* **319** (2008), 295–299.
- [114] S. Trotzky, Y.-A. Chen, A. Flesch, I. P. McCulloch, U. Schollwöck, J. Eisert, and I. Bloch, *Probing the relaxation towards equilibrium in an isolated strongly correlated one-dimensional Bose gas*, *Nature Phys.* **8** (2012), 325–330.
- [115] H. Uys, M. J. Biercuk, J. Britton, and J. J. Bollinger, *Towards spin squeezing with trapped ions*, *Quantum Africa 2010: Theoretical and Experimental Foundations of Recent Quantum Technology*, vol. 1469, (New York: AIP), 2012.
- [116] M. van den Worm, B. C. Sawyer, J. J. Bollinger, and M. Kastner, *Relaxation timescales and decay of correlations in a long-range interacting quantum simulator*, *New J. Phys.* **15** (2013), 083007.
- [117] H. Weimer, M. Müller, I. Lesanovsky, P. Zoller, and H.P. Büchler, *A rydberg quantum simulator*, *Nature Physics* **6** (2010), 382.
- [118] W. K. Wootters, *Entanglement of Formation of an Arbitrary State of Two Qubits*, *Phys. Rev. Lett.* **80** (1998), 2245–2248.
- [119] Y.Y. Yamaguchi, J. Barré, F. Bouchet, T. Dauxois, and S. Ruffo, *Stability criteria of the Vlasov equation and quasi-stationary states of the HMF model*, *Physica A* **337** (2004), 36–66.
- [120] B. Yan, S. A. Moses, B. Gadway, J. P. Covey, K. R. A. Hazzard, A. M. Rey, D. S. Jin, and J. Ye, *Observation of dipolar spin-exchange interactions with lattice-confined polar molecules*, *Nature* **501** (2013), 521–525.
- [121] D. Yan, X. Wang, L. Song, and Z. Zong, *Mean spin direction and spin squeezing in superpositions of spin coherent states*, *CEJP* **5** (2007), 367–376.
- [122] N. Y. Yao, C. R. Laumann, S. Gopalakrishnan, M. Knap, M. Müller, E. A. Demler, and M. D. Lukin, *Many-body localization in dipolar systems*, *Phys. Rev. Lett.* **113** (2014), 243002.